



# Université Lille1 Sciences et Technologies

Laboratoire Génie Civil et Géo-environnement

# Thèse

*Pour obtenir le grade de Docteur de l'Université Lille1 Sciences et Technologies*

Discipline : Génie Civil

# Interactions de radionucléides et de $CO_2$ avec les argiles: mécanismes à élucider à l'échelle nanométrique

Présentée et soutenue publiquement par

Wei YANG

le **5 Mai 2014** devant le jury:

| | |
|---|---|
| Rajeev AHUJA, Professeur, Université d'Uppsala (Suède) | Rapporteur |
| Anatoly BELONOSHKO, Professeur, Royal Institute of Technology-KTH-(Suède) | Rapporteur |
| Antonio Ferreira DA SILVA, Professeur, Université de Bahia (Brésil) | Examinateur |
| Isam SHAHROUR, Professeur, Université Lille 1 Sciences et Technologies | Examinateur |
| YuanYuan ZHENG, Maître de Conférences, Université Lille 1 Sciences et Technologies | Examinateur |
| Ali ZAOUI, Professeur, Université Lille 1 Sciences et Technologies | Directeur de Thèse |

# Acknowledgments

First of all, I would like to express the deepest appreciation to my supervisor, Professor A. Zaoui, who has the attitude and the substance of a genius: he continually and convincingly conveyed a spirit of adventure in regard to research and scholarship, and an excitement in regard to teaching. Without his guidance and persistent help this dissertation would not have been possible.

I would like to thank my committee members, Rajeev AHUJA, Anatoly BELONOSHKO for their help and suggestions concerning my research, Antonio Ferreira da Silva, Isam Shahrour and YuanYuan Zheng for their attentive lecture of my manuscript and examination of my work.

I would like to take this opportunity to express my sincere gratitude to my group members and friends: Amine Bouibes, Maria Suryatriyastuti, Anna Lushnikova, Kokou Anoukou who have given me support and encouragement in my thesis work. Special thanks to YUANYUAN ZHENG, who have given me abundantly help and advices, and accompany me during the hard period.

I wish to express my love and gratitude to my families, my husband Jishuai REN, my baby Roméo and my parents, for their endless love, encouragement and support.

# Table of contents

# List of Figures

# List of tables

# *General introduction*

Uranium is a chemical element in the actinide series of the periodic Table, it is a metallic unstable and weakly radioactive. In nature, uranium is found mostly as uranium-238 which exists a lot in soils and groundwater. Uranium mine is the main element in the nuclear fuel cycle and it is also a major component of the waste product($UO_2$ >95%) of the nuclear industry, the most stable chemical form of dissolved uranium is the uranyl ion $UO_2^{2+}$, that is potentially very mobile to complexate with organic and inorganic matter in the environment. Therefore, uranium and its decay products are hazardous pollutants of the environment. In order to protect environment and human, the adsorption properties of hexavalent uranyl species, $UO_2^{2+}$, have been most extensively studied. Such as the research in the geologic disposal of nuclear waste, we found that the clay minerals have low permeability; high adsorption capacity and plasticity which allow them to fix effectively radioactive waste to avoid their transport in groundwater. Clay minerals are ubiquitous components of rocks, soils and sediments and the clay minerals are highly sorptive due to their small particle sizes, large surface areas and chemically active surface defect sites. Thus, adsorption of uranyl at clay materials can take place everywhere. Natural clays as the adsorbent with a low cost have received much attention on heavy metals sorption from contaminated water.

Carbon dioxide $CO_2$ is a naturally occurring chemical compound. The environmental effects of carbon dioxide are of significant interest. Carbon dioxide is an important greenhouse gas, warming the earth's surface to a higher temperature by reducing outward radiation. However, problems may occur when the atmospheric concentration of greenhouse gases increases. Amount of carbon dioxide emissions since the industrial revolution to the point that significant climate warming and sea level raises have been attributed to anthropogenic activity. Atmospheric concentrations of $CO_2$ have increased from around 280 parts per million by volume (ppmv) in the 18th century to over 360 ppmv during 1997, primarily as a consequence of fossil fuel combustion for energy production. Clay minerals are of great practical importance here, in storage of carbon dioxide due to its hydraulic permeability and ability to retain mobile species.

Two prototypes of clays have been considered here: Kaolinite and Montmorillonite.

Kaolinite, a typical 1:1 clay mineral, part of the group of industrial minerals, is a major constituent of the clay mineral content of Opalinus clay. Kaolinite belongs to the class of layered two-sheet alumosilicates. As a clay mineral, kaolinite has a relatively small unit cell. Kaolinite has a low shrink-swell capacity and a low cation exchange capacity of the order of 3 to 15 meq/100g and therefore it is not expected to be an ion-exchanger of high order. The chemical composition of kaolinite is represented by a unit cell formula $Al_4Si_4O_{10}(OH)_8$, which consists of a tetrahedral Si sheet and an octahedral Al sheet. The formula indicates that there is no substitution of Si in the tetrahedral layer and no substitution of Al in the octahedral layer. Which means the net layer is overall neutral. However in nature, the small number of exchange sites is located on the surface of kaolinite by broken edges on the clay crystals. Nevertheless, the small CEC and the adsorption properties may play an effective role in scavenging inorganic and organic pollutants. For modeling uranyl adsorption onto kaolinite surface, kaolinite models with neutral unit cells had to be created by invoking surface defects. Inner-sphere complex is usually accompanied by the release of hydrogen H+ ions from the edge sites of kaolinite. The uranyl ions can be held through van der Waals interactions and form new bond with the kaolinite surface.

Montmorillonite is typical 2:1 clay of smectite group composed of two silica tetrahedral sheets with a central alumina octahedral sheet. In this work, a Wyoming type montmorillonite with unit cell formula $(Si_{7.75}Al_{0.25})(Al_{3.5}Mg_{0.5})O_{20}(OH)_4$ has been studied. The formula indicates that there is substitution of Si by Al in the tetrahedral layer and of Al by Mg in the octahedral layer. The charge resulting from these substitutions in the clay is -0.75e per unit cell. The resulting negative net charge needs to be balanced by adsorbing exchangeable cations. Montmorillonite is considered as an engineered barrier that would limit the movement of radionuclide.

It is difficult or impossible to carry out experiments under extremes of temperature and pressure, while the remarkable development of molecular computer simulations make a computer simulation of the material in high temperature, a nuclear reactor or a planetary core perfectly feasible. Computer simulation provides a direct route from the microscopic details of a system to macroscopic properties of experimental interest. The results of computer simulations may also be compared with those of real experiments. Atomic computer simulation methods have been widely used for instance to understand in

atomic level the mineral surface behaviour. It is important to get detailed structural and dynamic information on the relaxed structure when considering the processes of sorption. Classical Monte Carlo (MC) and molecular dynamics (MD) methods have been used in our work in order to understand the adsorption behaviour of radionuclide and carbon dioxide in clays surface.

In this thesis, we will investigate first the adsorption of uranyl on kaolinite surface by means of Monte Carlo and Molecular Dynamics simulation methods. Several adsorption sites have been modeled by invoking surface defects in order to have inner or outer-sphere complexes. Then, the adsorptions of uranyl species onto Montmorillonite surfaces in the presence of different counterions will be performed. Interaction energy between Montmorillonite sheets and work of adhesion between the radionuclide and MMT surface will be discussed as well. Finally, we will simulate the adsorption behavior of carbon dioxide in MMT, including thermodynamical, structural and dynamical properties.

The thesis is organised in two parts: part I is theory and part II summarizes the results and discussions.

The first chapter in part I contain an introduction of the clay minerals, where we will present the structure of clay. The works have been performed in the use of clays to the stockage of Uranyl species and carbon dioxide. We will focus our attention on the structure of Kaolinite and Montmorillonite and their adsorption properties.

The second chapter of part I is the introduction to molecular modeling, where we will present the simulation methods that are used in this study. Two techniques of Molecular simulations methods will be investigated: Molecular Dynamics (MD) and Monte Carlo (MC). This chapter describes these two methods as well as the interatomic potentials of the radionuclide-cation-clay and $CO_2$-cation-clay system components. For modeling of adsorption between uranyl species and Kaolinite, uranyl-kaolinite system is a neuter one. However, for the simulation of radionuclide adsorption onto montmorillonite surface, there are seven different interlayer cations such as: $Na^+$,$K^+$,$Cs^+$,$Ba^{2+}$,$Pb^{2+}$,$Ca^{2+}$ and $Zn^{2+}$, as well as three different radionuclide systems like ($UO_2(H_2O)_5$,$UO_2CO_3(H_2O)_5$, and $UO_2Cl_2(H_2O)_5$), which are deposited near the clay surface.

System set up and data analysis will be introduced in the third chapter. Three popular ensembles used in MD and MC simulations are presented in this chapter: the microcanonical NVE, the canonical NVT and the isothermal NPT. Periodic boundary conditions are applied in computer simulations in order to avoid the problem of limit of simulation size. We will investigate a general force field, CLAYFF, which has been employed in ours modeling for the calculating of potential energy.

The second part contains three chapters. In each chapter we investigate the case of corresponding adsorption study.

In chapter 4, we perform a MD study to investigate the adsorption of uranyl on kaonilite surface in the NVE and NVT ensemble with the x-y parallelogram boundary conditions. In order to have more models of uranyl adsorbed on clay surface, we will invoke defects at the opposite side of clay, which may be deprotonated when necessary for charge compensation. Several inner and outer-sphere complexes will be modeled and their structural and dynamical results will be studied.

Chapter 5 presents an intensive study of adsorption behavior between radionuclide elements and substituted Montomorillonite surface in the presence of different counterions. Structural properties like bond formation of U atom and surface Oxygen atom will be interesting to understand. We will compare the averaged bond length of U-different oxygen atoms (water oxygen Ow, surface oxygen Os and carbonate oxygen Oc) as well as the averaged bond length between cations and radionuclide species. Interactions between layered MMT sheets in the presence of different cations play an important role to characterize the surface properties. The main contributions to the formation of this interaction are the electrostatic interactions and the van der Waals interactions. These interactions between MMT sheets with different cations will be discussed. When an adsorption complex is modeled, the adhesion between the radionuclide surface and MMT surface is quantified by the work of adhesion. It combines all the fundamental interfacial forces responsible for adhesion of these two different surfaces. The work of adhesion will be evaluated for different models in this chapter.

In chapter 6, we report a Monte Carlo and molecular dynamics simulations study of carbon dioxide in hydrated calcium montmorillonite at different burial depth, including thermodynamical, structural and dynamical properties. Systems containing approximately one, two, and three molecular layers of

water have followed gradients of 150bar/km and 30K/km, from burial depth of 0km (280K and 1.0bar), to 3km (370K and 450bar) and to a maximum burial depth of 6km (460K and 900bar). In addition, diffusion behaviors will be studied in order to see the dependence of the interlayer diffusion depends strongly on the water content and burial depth.

Finally, a summary of the thesis will be given at the end of the manuscript.

# *Part I* : Theory

# Chapter 1. Introduction of the clay minerals

## 1.1 Overview of the clay minerals

Clays and clay minerals are considered as the materials of the 21st century because they are cheap, abundant in many near-surface geological environments. They are typically formed over long periods of time by the gradual chemical weathering of rock and vary in chemical composition, structure and modes of occurrence. Clay minerals are phyllosilicates that make up the fine-grained fraction of soils and sediments, which are smaller than 2㎛. The clay minerals are hydrous aluminum silicates and in some of these minerals, iron and magnesium substitute for the aluminum and in some others there are alkaline and alkaline earth elements present as essential constituents[1]. Clay research focuses on the geological, geotechnical and mineralogical aspects of clays for a long time, and on physic-chemical for recent years. The most important properties of clay materials are the low hydraulic permeability and their ability to retain mobile species. The highly adsorption due to their small particle size, large surface areas and chemically active surface defect sites make them important in storage of radioactive waste and carbon dioxide. We are interested here in the interaction between the clay minerals and other compounds which can be water, polymer, iron, organic or molecule. This interaction is influenced by many factors such as the acid-basic character (PH and ionic strength) and thermodynamic conditions (pressure and temperature).

## 1.2 Structure and composition of the clay minerals

The atomic structure of the clay minerals consists of two basic units, an octahedral sheet and a tetrahedral sheet. One tetrahedral sheet and one octahedral sheet are joined by sharing the apical oxygen or hydroxyls to form a 1:1 (T-O) layer structure. Condensation of two tetrahedral sheets with one octahedral sheet through which the octahedral sheet becomes sandwiched between two opposing tetrahedral sheets gives rise to a 2:1 (T-O-T) type layer structure.

In the 1:1 layer structure, the unit cell includes six octahedral sites and four tetrahedral sites. Six octahedral sites and eight tetrahedral sites characterize the 2:1 layer unit cell.

### 1.2.1 Tetrahedral sheet

The first structural unit is the silica tetrahedral layer in which the tetrahedron consists of a central $Si^{4+}$ cation coordinated to four oxygens. These tetrahedrons are arranged to form a hexagonal network $(SI_4O_{10})^{4-}$ by sharing oxygen atom. The negative charge of $(SI_4O_{10})^{4-}$ may be balanced by replacement of four oxygens by hydroxyls or by union. The structure can be repeated infinitely in two horizontal directions to form what is called the silica tetrahedral sheet (Fig.1-1). The tetrahedral apical oxygen atoms orient to the same side of the sheet and ready to connect with the octahedral sheets. The tetrahedral cations $Si^{4+}$ can be replaced by $Al^{3+}$ or $Fe^{3+}$.

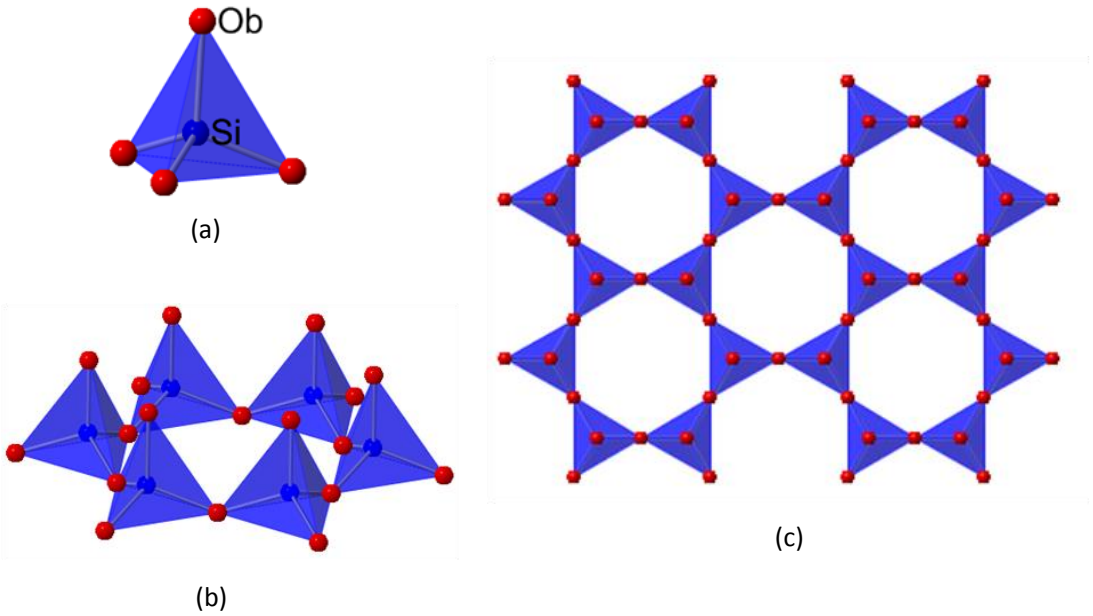


**Fig. 1–1: (a) silica tetrahedron ($SiO_4$); (b) silica tetrahedral arranged in a hexagonal hole; (c) silica tetrahedral sheet.**

The second structural unit is the octahedral sheet, which is comprised of closely packed oxygens and hydroxyls in which aluminum, iron, and magnesium atoms are arranged in octahedral coordination (Fig.1-2).

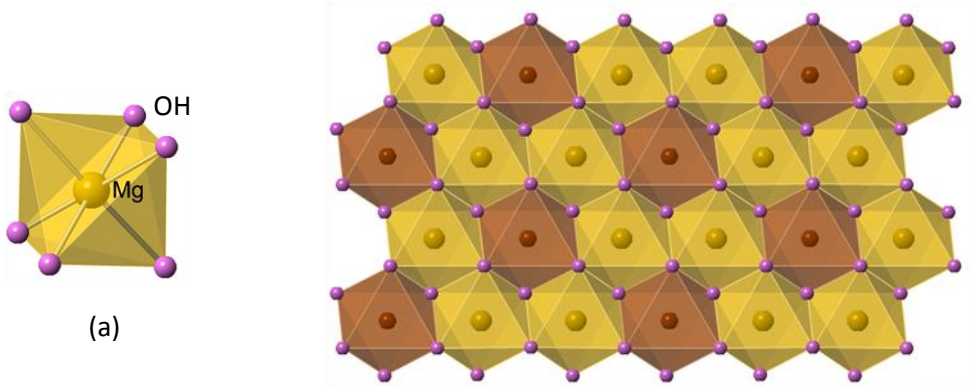


(a) (b)

**Fig. 1–2: (a) octahedral unit; (b) octahedral sheet.**

When aluminum with a positive valence of three is the cation present in the octahedral sheet, only two-thirds of the possible positions are filled in order to balance the charges. When only two-thirds of the positions are filled, the mineral is termed dioctahedral, the composition is $Al_2(OH)_6$. When magnesium with a positive charge of two is present, all three positions are filled to balance the structure and the mineral is termed trioctahedral, the composition is $Mg_3(OH)_6$ (Fig.1-3). Octahedral cations are usually $Al^{3+}$, $Fe^{3+}$, $Mg^{2+}$ and $Fe^{2+}$.

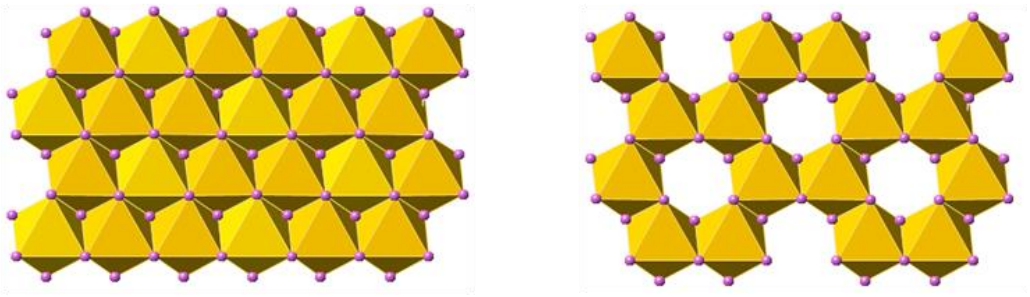

(a) (b)

**Fig. 1–3: (a) Trioctahedral sheet; (b) dioctahedral sheet.**

### *1.2.3 Classification of the clay minerals*

On the basis of the crystal chemistry and the structure, clay minerals can be divided into following types: 1). 1:1 type kaolinite group; 2) 2:1 type pyrophyllite-talc group, smectite group, vermiculite group,

hydromica group, chlorite group and 3) clay minerals with chain-layered structure Hormite group( palygorskite-attapulgite, sepiolite)(Fig.1-4).

The three main groups of clay minerals are Kaolinite group, Illite group and Montmorillonite group. The Kaolinite group is the mineral the most dominant part of residual clay deposits and is made up from large stacks of alternating single tetrahedral sheets of silicate and octahedral sheet of aluminum. Kaolinites are very stable with a strong structure and absorb little water. They have low swelling and shrinkage responses to water content variation. The Illite group consists of a series of single octahedral sheets of aluminum sandwiched between two tetrahedral sheets of silicon. In the octahedral sheets some of the aluminum is replaced by iron and magnesium and in the tetrahedral sheets there is a partial replacement of silicon by aluminum. Illites tend to absorb more water than kaolinites and have higher swelling and shrinkage characteristics. For Montmorillonite group, they have a similar structure to the illite group but, in the tetrahedral sheets, some of the silicon is replaced by iron magnesium and aluminium. Montmorillonites exhibit extremely high water absorption, swelling and shrinkage characteristics [2](Fig.1-4).

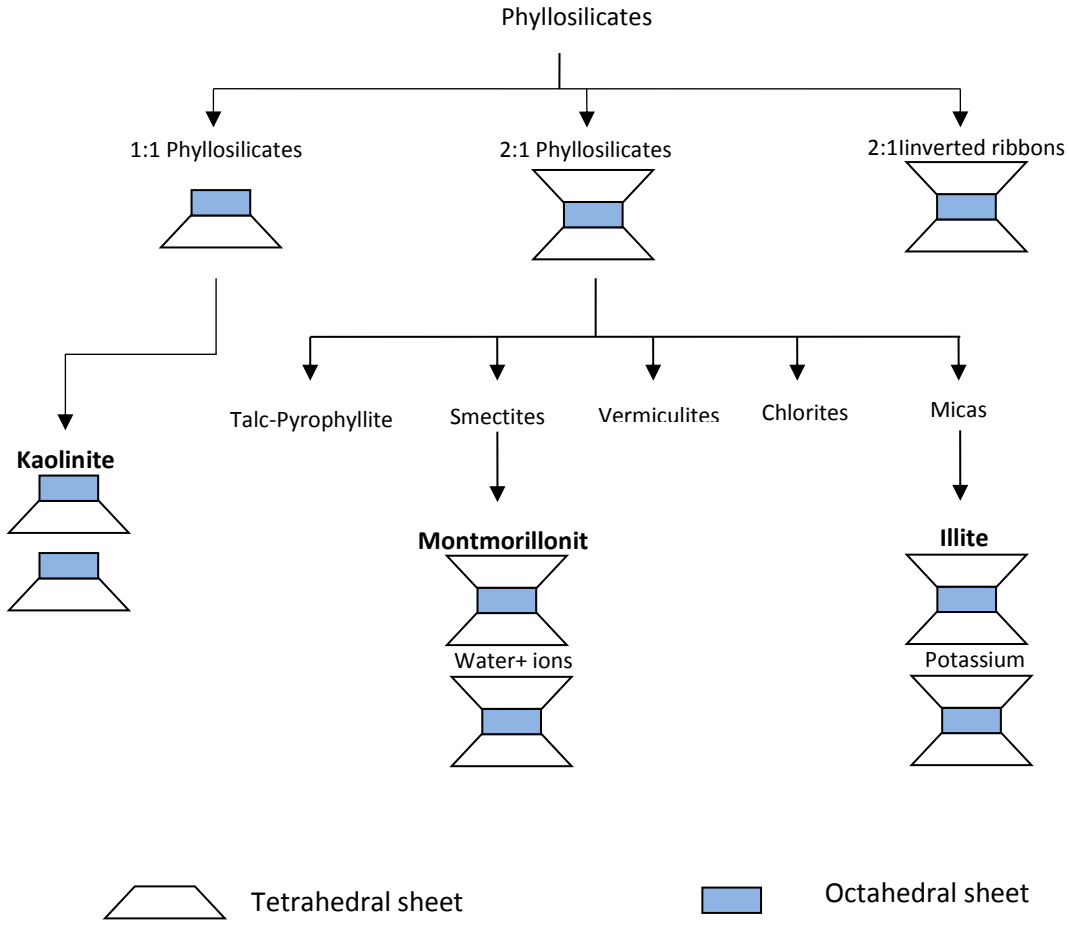


**Fig. 1–4: classification of the clay minerals**

## 1.3 The use of clays for the storage of radioactive waste and $CO_2$: research need

The long timescales over which some of the waste remains radioactive led to the idea of deep geological disposal in underground repositories in stable geological formations. Isolation is provided by a combination of engineered and natural barriers (rock, salt, clay). Deep geological disposal remains the preferred option for waste management of long-lived radioactive waste in several countries, including Argentina, Australia, Belgium, Czech Republic, Finland, Japan, Netherlands, Republic of Korea, Russia, Spain, Sweden, Switzerland and USA[1].

The Swedish proposed to use copper container with a steel insert to contain the spent fuel. After placement in the repository about 500 metres deep in the bedrock, the container would be surrounded by a bentonite clay buffer to provide a very high level of containment of the radioactivity in the wastes over a very long time period. In June 2009, the Swedish Nuclear Fuel and Waste Management Company (SKB) announced its decision to locate the repository at Östhammar[1].

The Belgian disposal concept proposes that spent fuel and high-level radioactive waste is placed in high integrity steel containers and then emplaced in excavated tunnels within ductile clay. The very low permeability of the clay leads to virtually no groundwater flow over long time periods. Waste would be backfilled with excavated clay or, alternatively, could be emplaced into unlined secondary tunnels where the clay would be allowed to creep into contact with the waste containers[3]. The French radioactive waste disposal agency ANDRA is designing a deep geological repository in clays at Bure in eastern France. This will be for disposal of vitrified high-level waste (HLW) and long-lived intermediate-level waste. The repository is designed to operate at up to 90ºC, which is likely to be reached about 20 years after emplacement. ANDRA expects to apply for a construction and operating licence in 2014(Fig.1-5)[2].

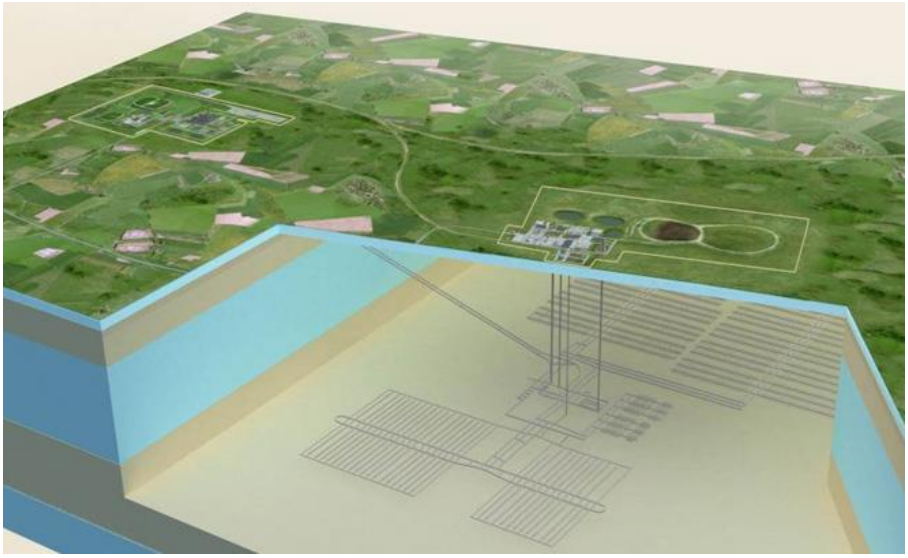

**Fig. 1–5: Schematic diagram of the installations at the future High-level and long-live waste repository of ANDRA.**

[1] http://www.world-nuclear.org/info/Nuclear-Fuel-Cycle/Nuclear-Wastes/Appendices/Radioactive-Waste-Management-Appendix-2--Storage-and-Disposal-Options/#g

[2] http://www.andra.fr/international/pages/en/menu21/waste-management/waste-management-issues-at-national-level/high-level-waste-and-long-lived-intermediate-level-waste-1618.html

On the other hand, we consider that Carbon dioxide ($CO_2$) is a main cause of climate change, and human activities raise the level of $CO_2$ in the earth's atmosphere. In order to reduce $CO_2$ emissions, one option is to capture $CO_2$ produced by power generation and industrial processes and store the $CO_2$ deep underground. This is known as $CO_2$ Capture and Storage (CCS). At the end of 2010, there were 4 commercial applications of CCS in operation around the world; injecting over 4 million tonnes a year of $CO_2$[4]. Numerous other projects are at varying stages of planning, and many other projects are in operation at the pilot scale.

The best rocks for $CO_2$ storage are depleted oil and gas fields and deep saline formations. These are layers of porous rock over 1km underground. The deep saline formations are rocks with tiny spaces that are filled with very salty water. They exist in most regions of the world and appear to have a very large capacity for $CO_2$ storage. $CO_2$ dissolved in salt water is weakly acidic and can react with the minerals in the surrounding rocks, forming new minerals, as a coating on the rock (much like shellfish use calcium and carbon from seawater to form their shells). This process can be rapid or very slow (depending on the chemistry of the rocks and water) and it effectively binds the $CO_2$ to the rocks[4].

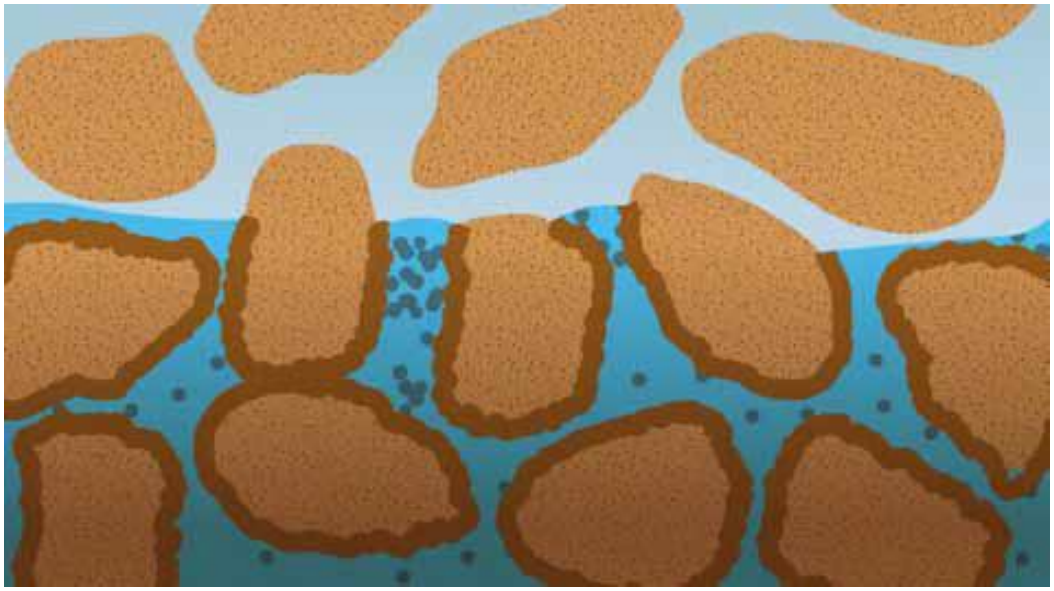

**Fig. 1–6: Mineral storage of $CO_2$.**

In recent years, the study in actinide adsorption on clay mineral has greatly increased due to an ongoing concern in environmental research. Their interaction with clay mineral surface plays an important role to govern the migration of actinide in the environment. Experiments are unable to give complete information about their interaction in atomic level. However, molecular modeling methods have been increasingly used in the past decade to simulate a wide range of materials and to evaluate their microscopic structure, physical, and thermodynamic properties. Molecular computer simulations have become extremely helpful in providing an atomistic perspective on the structure and behavior of clay minerals[5]. These studies have typically used classical Monte Carlo (MC) and molecular dynamics (MD) methods to illustrate the interactions between $UO_2$ species and clay (Kaolinite and Montmorillonite) surface, as well as the adsorption of CO2 onto Montmorillonite. In addition, we will study the surface energy between layered Montmorillonite sheet and the work of adhesion between radionuclide and charged Montmorillonite.

## 1.4 Presentation of Kaolinite

Kaolinite is one of the most abundant clay minerals in the earth's crust. The basic kaolinite structure is a layer of a single tetrahedral sheet and a single octahedral sheet. The two sheets are combined to form a unit in which the tips of the silica tetrahedrons are joined with the octahedral sheet. The unit cell composition for Kaolinite is $Al_4Si_4O_{10}(OH)_8$ and the chemical composition is $SiO_2$, 46.54%; $Al_2O_3$, 39.50%; and $H_2O$, 13.96%. The charge distribution in the kaolinite layer is shown in Table1-1. The combined octahedral and tetrahedral sheets are continuous in the a- and b-axis directions and are stacked one above the other in the c-axis direction. The thickness of the unit layer is about 7.13Å. Two-thirds of the octahedral positions are filled by an aluminum atom. The aluminum atoms are surrounded by four oxygen and eight hydroxyls (Fig.1-7). Kaolinite structure contains two types of hydroxyl groups. The first is located at the top of the tetrahedral hexagonal cavity. Such OH group is situated in the plane of the oxygen atoms and shared by aluminum octahedral. This is called internal hydroxyl group. The second hydroxyl type occupies the basal surface of the octahedral sheet is called external hydroxyl group.

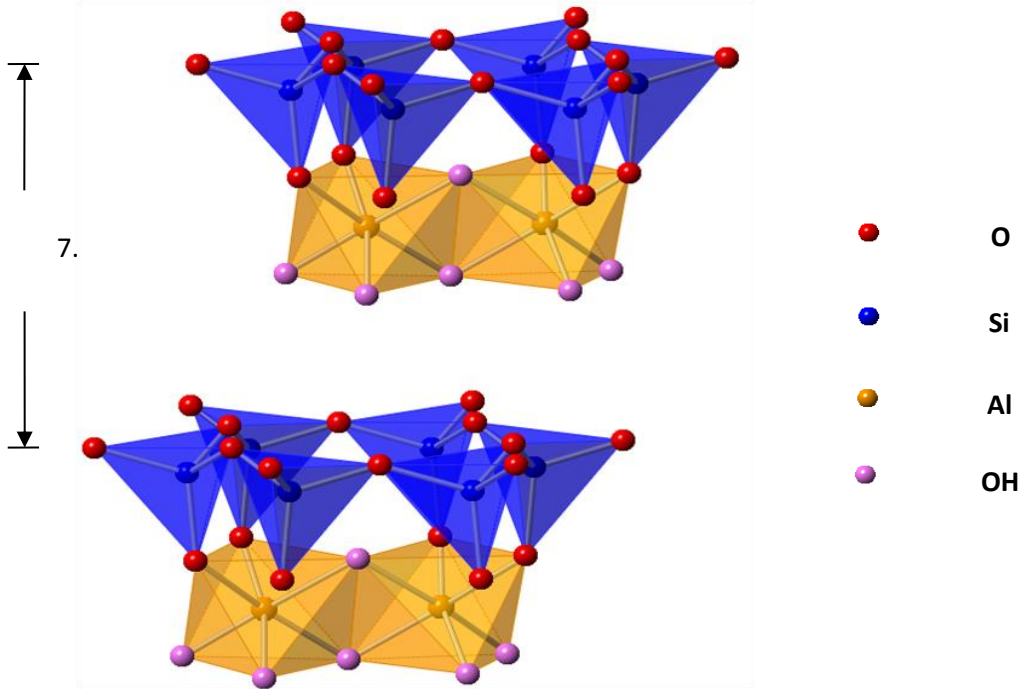


**Fig. 1–7: Diagrammatic sketch of the structure of Kaolinite.**

**Table1-1: charge distribution of kaolinite layer**

| | |
|---|---|
| $6O^{2-}$ | $12^{-}$ |
| $4Si^{4+}$ | $16^{+}$ |
| $4O^{2-}+2(OH)^{-}$ | $10^{-}$ (layer shared by the tetrahedral and octahedral sheets) |
| $4Al^{3+}$ | $12^{+}$ |
| $6(OH)^{-}$ | $6^{-}$ |

At its morphology, the kaolinite particles appear by SEM (Scanning Electron Micrograph) in the form of hexagonal plates [6](Fig. 1-8). When viewing along the (001) direction, elongated hexagonal plates are observed. The diameter size of the hexagonal plates extend up to 6.0-10.0 μm along the (010) direction and 3.0-7.0 μm when perpendicular to the (010) direction (Fig.I-8a). A book-type structure is observed along the (001) direction, in which coherent plates are separated by cleavage planes. The thickness of the coherent plates in many crystals extends up to 205-3.0 μm, but in some crystals only to ~0.25-1.0 μm (Fig. 1-8b).

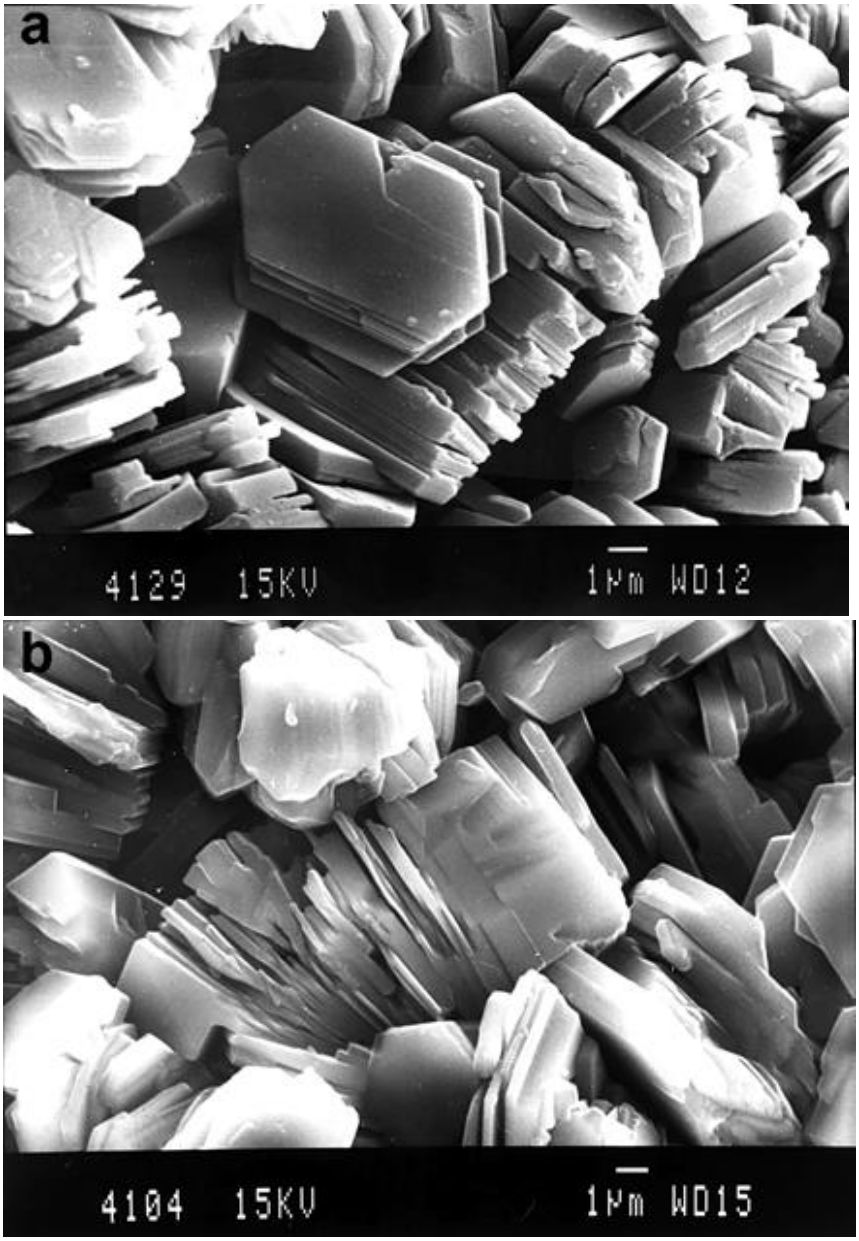


**Fig. 1–8: Scanning electron micrograph of kaolinite crystals (a) view along the crystallographic (001) direction. (b) View along (010) or (100) direction displaying a book-type structure[6].**

## 1.5 Presentation of Montmorillonite

The montmorillonite is a 2:1 layer mineral composed of two silica tetrahedral sheets with a central octahedral sheet (Fig. 1-9). All the tips of the tetrahedral point are towards the centre of the unit cell. The oxygens forming the tips of the tetrahedral are common to the octahedral sheet as well. Water

molecules and cations occupy the space between the layers. The basal spacing of montmorillonite changes with the interlayer cations. As the most common interlayer cations, calcium ions and water may balance the layer charge deficiency and the basal spacing of the calcium montmorillonite is 14.2Å. Sodium montmorillonite occurs when the charge deficiency is balanced by sodium ions and water. The basal spacing corresponds to 12.2Å. A typical montmorillonite contains $Na^+$, $K^+$, $Li^+$,$Mg^{2+}$ and $Ca^{2+}$[7]. The theoretical formula of montmorillonite is $Si_8Al_4O_{20}(OH)_4(H_2O)_N$, in which N water stay in the interlayer spaces. The theoretical charge distribution in the unit cell Montmorillonite without considering substitutions is shown in Table1-2. The theoretical composition without the interlayer cations is 66.7% of $SiO_2$; 28.3% of $Al_2O_3$; and 5% of $H_2O$.

However, in montmorillonite, we must consider the substitution in the octahedral sheet and some in the tetrahedral sheet for silicon and aluminum. Aluminum may be replaced by magnesium, iron, zinc, nickel, lithium or other cations in the octahedral sheet. Aluminum may replace the silicon ions up to 15% and in the tetrahedral sheet. These substitutions make the sheets negative charged, which is balanced by exchangeable cations adsorbed between the layers. If the interlayer cation is sodium, the specific mineral called sodium montmorillonite and if it is calcium, it is a calcium montmorillonite. The charged montmorillonite has high cation exchange capacities (CEC), between 80 and 130 meq/100g for sodium montmorillonite and between 40 and 70 meq/100g for calcium montmorillonite. The high CEC makes them capable to exchange the interlayer water and associated cations with surrounding. Montmorillonite has generally a high surface area, of about 150-200 $m^2/g$ for sodium montmorillonite. Montmorillonite exhibits a high sorptivity generated by its high surface area and high layer charge.

**Table1-2: charge distribution in unit cell Montmorillonite without substitution**

| | |
|---|---|
| **$6O^{2-}$** | **$12^-$** |
| **$4Si^{4+}$** | $16^+$ |
| **$4O^{2-}$+2$(OH)^-$** | $10^-$ (plane common to tetrahedral and octahedral sheets) |
| **$4Al^{3+}$** | $12^+$ |
| **$4O^{2-}$+2$(OH)^-$** | $10^-$(plane common to tetrahedral and octahedral sheets) |
| **$4Si^{4+}$** | $16^+$ |
| **$6O^{2-}$** | $12^-$ |

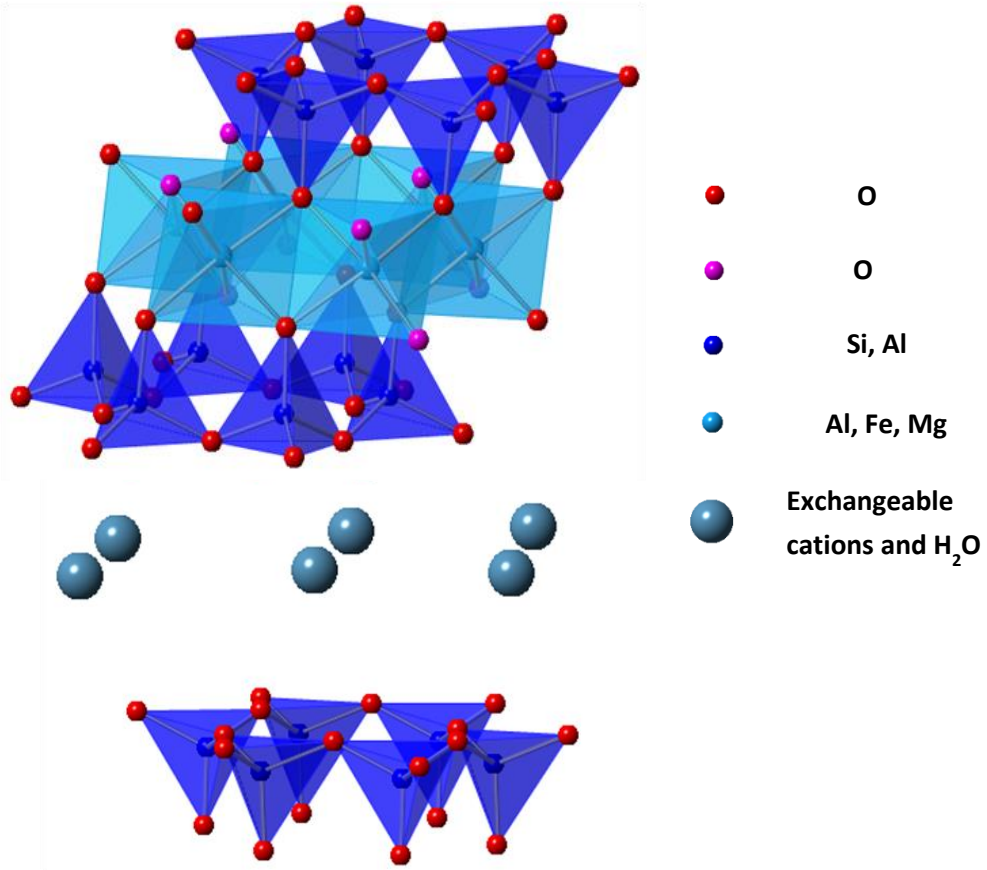


**Fig. 1–9: Diagrammatic sketch of the montmorillonite structure**

# Chapter 2. Introduction to molecular computer simulations

## 2.1 Introduction

Molecular computer simulations mean to construct molecular system with the computational techniques and to realize a numbers of calculations on these molecules in order to understand and predict the properties and behaviour of materials[8]. It may be very difficult and therefore expensive to measure the properties of real materials at very high pressures or temperatures. But it is feasible in a computer simulation. In addition, we can use computer simulation to predict the properties of materials that have not yet been made.

Numerical simulation of dense liquids was one of the first problems to be tackled when electronic computers were made available for unclassified research. In fact, Metropolis Rosenbluth, Teller, and Teller have carried out the first computer simulation of a liquid on the MANUAC computer at Los Alamos in 1953 by using the Metropolis Monte Carlo (MC) method[9]. In few years later, MC simulations were carried out on the Lennared-Jones interaction potential[10] which made it possible to validate experimental studies. In 1957, Alder and Wainwright[11] have reported their first proper Molecular Dynamics (MD) simulations. Molecular dynamics (MD) is the term used to describe the solution of the classical equations of motion (Newton's equations) for a set of molecules[12]. Then in 1960, the first MD simulation of a model for a real material was reported by the group led by Vineyard at Brookhaven[13], who simulated radiation damage in crystalline Cu.

Molecular computer simulations have been widely used to provide an atomistic perspective on the structure and behaviour of clay minerals. MC and MD methods have typically used to evaluate the interlayer structure and adsorption behaviour [14-23]. These simulation techniques allow us to determine a system of molecules: it's chemical structure (number and type of atoms, bonds, bonds lengths, angles and dihedral angles); its dynamical properties (layer spacing changes, coefficient de diffusion, energy, and enthalpy) and its activity (chemical reaction with other molecules such as bond break, bond formation, and electrostatic potentials).

## 2.2 Monte Carlo Simulation

### *2.2.1 Introduction to Monte Carlo method*

In order to study the diffusion of neutrons in fissionable material, at the end of the Second World War, von Neumann, Ulam and Metropolis have developed the Monte Carlo method. The name 'Monte Carlo', chosen because of the extensive use of random numbers in the calculation, was coined by Metropolis in 1947 and used in the title of a paper describing the early work at Los Alamos [24]

Monte Carlo methods are a class of computational algorithms that rely on repeated random sampling to obtain numerical results. The Metropolis Monte Carlo method aims to generate a trajectory in phase space which samples from a chosen statistical ensemble[24]. We can illustrate the use of the MC technique as a method of integration through the simply example of calculation of π. Consider a circle centred at the origin and inscribed in a unit square. A great number of independent random points are generated within the square OABC (Fig. 2-1). The distance from the random point to the origin is calculated. We score the total point that landed inside the square m, and then the value of π can be calculated from the fraction of points that fall within the shaded region n.

$$\mathbf{S_{shaded\ region}} = \frac{\pi \mathbf{R^2}}{\mathbf{4}} = \frac{\pi}{\mathbf{4}} \qquad (2.1)$$

$$\boldsymbol{\pi} = \frac{\mathbf{4}\times \mathbf{S_{shaded\ region}}}{\mathbf{S_{square\ region}}} \cong \frac{\mathbf{4}\times \mathbf{n}}{\mathbf{m}} \qquad (2.2)$$

The points must be uniformly distributed and we should have large numbers of input points. After placing 30000 random points, the estimate for π is within 0.07% of the actual value.

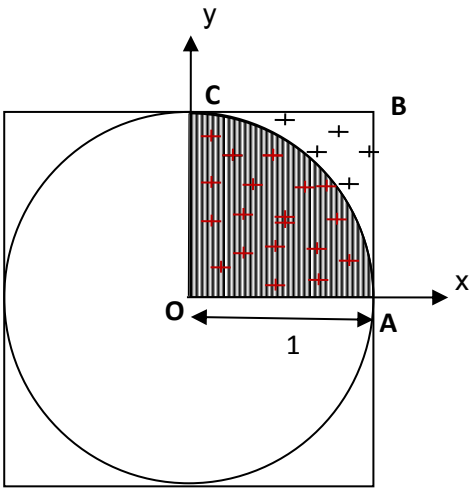


**Fig. 2–1: the geometry for the Monte Carlo integration applied to approximating the value of $\pi$.**

### *2.2.2 The Monte Carlo algorithm*

The Monte Carlo method is a simulation technique for phenomena in thermodynamic equilibrium by generating a series of microscopic states under a certain stochastic law. We illustrate how thermodynamic equilibrium occurs in microscopic states in a practical situation by considering a two particle attractive system in Fig.2-2. When the two particles overlap as shown in Fig.2-2a, they may have significant repulsive interaction energy. As shown in Fig.2-2b, the interaction energy decreases for the case of close proximity. If the two practices are sufficiently separated in Fig.2-2c, the interaction energy is negligible as zero. In actual phenomena, microscopic states arise frequently a low energy system like shown in Fig.2-2b

(a) (b) (c)

**Fig. 2–2: typical energy situations for a two particle system: (a) overlapping; (b) close proximity; (c) sufficiently distant**

In a Monte Carlo simulation of a particle system, the main procedure is as follow (Fig. 2-4):

1: Specify the initial coordination and direction of all particles in a microscopic state m, the position vector of an atom i (i=1,2,….,N) is denoted by $r_i^m$ . Then the total interaction energy of the system can be calculated as a function of the atom coordination and it can be expressed as$U_m$.

2: A particle i selected at random in the system and make it move from its position $r_i^m$ to any point $r_i^n$ (Fig. 2-3). The interaction energy $U_n$ for this new configuration is calculated. The change in potential energy is calculated by considering the interaction of atom i with all its neighbours within a cutoff distance:

$$\Delta U_{nm} = \sum_{j=1}^{N} U\left(r_{ij}^n\right) - \sum_{j=1}^{N} U(r_{ij}^m) \qquad (2.3)$$

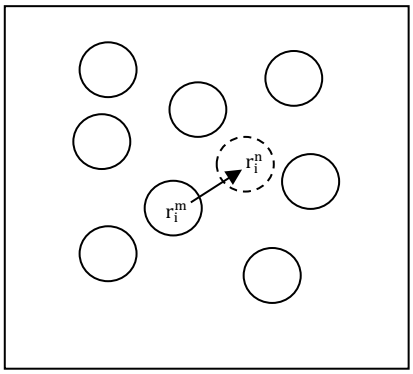


**Fig. 2–3: A new microscopic state n is generated from state m by moving particle i from $r_i^m$ to $r_i^n$.**

3: If the interaction energy decreases for this new microscopic state$U_m \geq U_n$, we will accept this new configuration and repeat from step 2.

If the interaction energy increases for the new microscopic state $U_m < U_n$, we calculate the transition probability from microscopic state m to n, $\frac{\rho_n}{\rho_m}$, which is illustrated in the 'Metropolis method'[25]. The radio of $\frac{\rho_n}{\rho_m}$ is obtained as follows:

$$\frac{\rho_n}{\rho_m} = \exp\left(-\frac{\Delta U_{nm}}{KT}\right) \qquad (2.4)$$

Where $\rho_m$ and $\rho_n$ are the probability density functions for microscopic states m and n, T is the temperature and K is the Boltzmann constant.

A random number $\xi$ is generated uniformly from zero to unity, after comparing this random number with the probability, we have the following possibilities:

If $\frac{\rho_n}{\rho_m} \geq \xi$ , then this new configuration is accepted and repeated from 2;

If $\frac{\rho_n}{\rho_m} < \xi$, then this microscopic state is rejected.

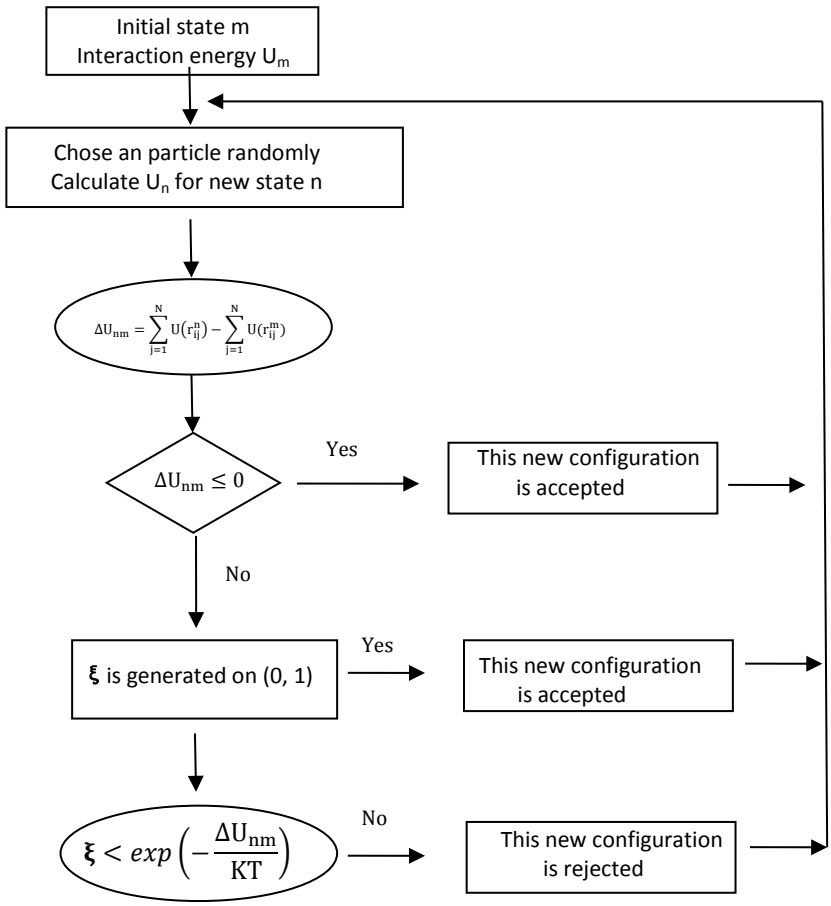


**Fig. 2–4: the algorithm for Monte Carlo simulations.**

We notice that there is no equation of motion in the Monte Carlo simulation procedure, and therefore it is applicable to only thermodynamic equilibrium phenomena. Hence, the MC method is unsuitable to deal with the dynamic properties of a system, which are dependent on time. We will illustrate in the following paragraphs the most important point of the concept of the Molecular Dynamic method, which are applicable to both thermodynamic equilibrium and non-equilibrium phenomena.

## 2.3 Molecular Dynamics simulation

Molecular Dynamics method is a technique useful for computing thermodynamic equilibrium and dynamical properties of a many body system in a non-equilibrium situation. In a MD simulation, we prepare a sample which is regarded as a collection of N particles. These particles are allowed to interact by exerting forces on each other and we solve Newton's equation of motion for this system. The goal is to compute the atom's trajectories numerically by involving the interaction model. We equilibrate the system until the properties of the system no longer change with time, and then we perform the actual measurement.

### *2.3.1 Equations of motion*

In Molecular Dynamics simulations, particle motion is generally simulated following Newton's equations of motion in classical theory. Computer is a powerful tool for a microscopic analysis. Consider a particle *i* in the simulation system, its position and velocity are described by the vector **r**(t)=(x,y,z) and **v**(t)=($v_x$, $v_y$, $v_z$), respectively. The velocity is how fast **r** changes with time. The acceleration vector is described by the time derivation of velocity $\mathbf{a} = d\mathbf{v}(t)/dt$. The mass of particle *i* is denoted by $m_i$, and the force acting on this particle denoted by $f_i$, which is calculated by summing up all the interactions between atom *i* and the surrounding atoms. Therefore the particle's equation of motion is described as follows:

$$f_i = m_i a = m_i \frac{d^2 r_i(t)}{dt^2} \tag{2.5}$$

For a system of N particles, the total potential energy U(r) is determined by summing up the potential energy associated with all types of interactions. The force $\mathbf{f}_i$ can be written as the negative derivative of the potential:

$$f_i = -\nabla_{r_i} U(r) \tag{2.6}$$

Once the force acting on atoms determined by the total interaction energy, new acceleration and velocities will be computed by application of algorithm.

Therefore, the main procedure for a Molecular Dynamics simulation is constructed according to the following steps:

1. Specify the initial position and velocity of all particles.
2. Calculate the total interaction energy for the system by the initial positions and then the force acting on particles
3. New positions and velocities are evaluated by computer algorithm.
4. Repeat the procedures from step 2.

### *2.3.2 Integrating the equation of motion*

A good algorithm to integrate Newton's equation of motion is required to a good Molecular Dynamics program. There are many algorithms that can be used and each has its own advantages and disadvantages. Let us look at the criteria that a good algorithm should satisfy when making our choice:

- The speed is important, it should be fast;
- Accuracy for large time steps Δt is necessary, the longer the time step that we can use, the fewer evaluation of the forces are need per unit of simulation time[8];
- The memory storage requirement for storing information should be little;
- It should satisfy the known conservation laws for energy and momentum;
- Time reversibility;
- It should be simple enough in its form and easy to implement.

For Molecular Dynamics, not all of the above points are very important. Compared with the accuracy for large time steps, the speed of the integration algorithm is not crucial. It is far more important to be able to employ a long time step$\Delta t$ . Energy conservation for short time and long-time is an important criterion. The sophisticated higher-order algorithms tend to have very good energy conservation for short times but the overall energy drifts for long times.

Let us focus now on Verlet-like algorithms. If the classical trajectory is continuous, then an estimate of the positions, velocities at time $t + \Delta t$ may be obtained by a truncated Taylor expansion around time $t$:

$$r_i(t+\Delta t) = r_i(t) + \Delta t\, v_i(t) + \frac{\Delta t^2}{2m_i} f_i(t) + \cdots \quad (2.7)$$

$$v_i(t+\Delta t) = v_i(t) + \frac{\Delta t}{m_i} f_i(t) + \cdots \quad (2.8)$$

#### 2.3.2.1 The Verlet algorithm

The most widely used method of integrating the equations of motion is adopted by Verlet[26] and attributed to Störmer[27]. If we solve the second order system (equation 5) based on the current positions $\mathbf{r}_i(t)$ and forces $\mathbf{f}_i(t)$ and the position $\mathbf{r}_i(t-\Delta t)$ from previous step, we get the Verlet algorithm. The derivation is straightforward:

$$r_i(t-\Delta t) = r_i(t) - \Delta t\, v_i(t) + \frac{\Delta t^2}{2m_i} f_i(t) + \cdots \quad (2.9)$$

Summing the two equations of (7) and (9), we obtain the positions and for the velocities by subtracting them, respectively:

$$r_i(t+\Delta t) = 2r_i(t) - r_i(t-\Delta t) + \frac{\Delta t^2}{m_i} f_i(t) \quad (2.10)$$

$$v_i(t) = \frac{r_i(t+\Delta t) + r_i(t-\Delta t)}{2\Delta t} \quad (2.11)$$

The velocities are not needed to compute the trajectories, but they are useful for estimating observables like the kinetic energy. The Verlet algorithm is fast for integrating the equations of motion. However we should expect to compute the forces on all particles frequently because it is not particularly accurate for long time steps. It might be useful when we simulate very large systems as Verlet algorithm requires little memory. In additional, the Verlet method has excellent energy conserving properties even with long time steps and it is easy to program. Another remark regarding the Verlet algorithm is that $\mathbf{r}_i(t-\Delta t)$ and $\mathbf{r}_i(t+\Delta t)$ play symmetrical roles in equation (I.10) making it time-reversible.

#### 2.3.2.2 Leap-frog algorithm

Several algorithms are equivalent to the Verlet scheme. One of these is a so-called half-step 'leap-frog' algorithm[28], which is obtained by making some modifications to the basic Verlet scheme. This algorithm evaluates the velocities at half-integer time steps and uses these velocities to compute the

new positions. To derive the Leap Frog algorithm from the Verlet scheme, we start by defining the velocities and positions at half-interger time step as follows:

$$v_i\left(t+\frac{\Delta t}{2}\right) = v_i\left(t-\frac{\Delta t}{2}\right) + \frac{\Delta t}{m_i} f_i(t) \tag{2.12}$$

$$r_i(t+\Delta t) = r_i(t) + \Delta t\, v_i\left(t+\frac{\Delta t}{2}\right) \tag{2.13}$$

The velocities are updated at half time steps and 'leap' ahead the positions. The current velocities may be obtained by calculating the average of the velocities half a timestep either side of time *t*:

$$v_i(t) = \frac{v_i\left(t+\frac{\Delta t}{2}\right) + v_i\left(t-\frac{\Delta t}{2}\right)}{2} \tag{2.14}$$

This is illustrated in Fig.2-5. In this method, the energy at time *t* can be calculated with initial positions of all practices to obtain the force, and then, the new accelerations at time *t* may be evaluated ready for the next step. In the next, $\mathbf{v}_i\left(t+\frac{\Delta t}{2}\right)$ and $\mathbf{r}_i(t+\Delta t)$ will be calculated by the applications of equation 2.12 and 2.13. Numerical imprecision is minimized in the leap-frog scheme. However, the velocities are still not accessible in a completely satisfactory manner.

#### 2.3.2.3 Velocity-Verlet algorithm

An algorithm which does store positions, velocities, and forces all at the same time *t* is given by the Velocity-Verlet[29] scheme. First, the new positions at time $t+\Delta t$ are obtained according to equation 2.15 and the velocities at mid-step are computed using the equation 2.16:

$$r_i(t+\Delta t) = r_i(t) + \Delta t\, v_i(t) + \frac{\Delta t^2}{m_i} f_i(t) \tag{2.15}$$

$$v_i\left(t+\frac{1}{2}\Delta t\right) = v_i(t) + \frac{\Delta t}{2m_i} f_i(t) \tag{2.16}$$

The forces at time $t+\Delta t$ are computed by the new position to obtain the new accelerations, and the velocity move completed

$$v_i(t+\Delta t) = v_i\left(t+\frac{1}{2}\Delta t\right) + \frac{\Delta t}{2m_i} f_i(t+\Delta t) \tag{2.17}$$

The Velocity-Verlet algorithm is very stable and has become perhaps the most widely used Molecular Dynamics algorithm.

The procedures of these three different Verlet-likes algorithm are shown in Fig. 2-5.

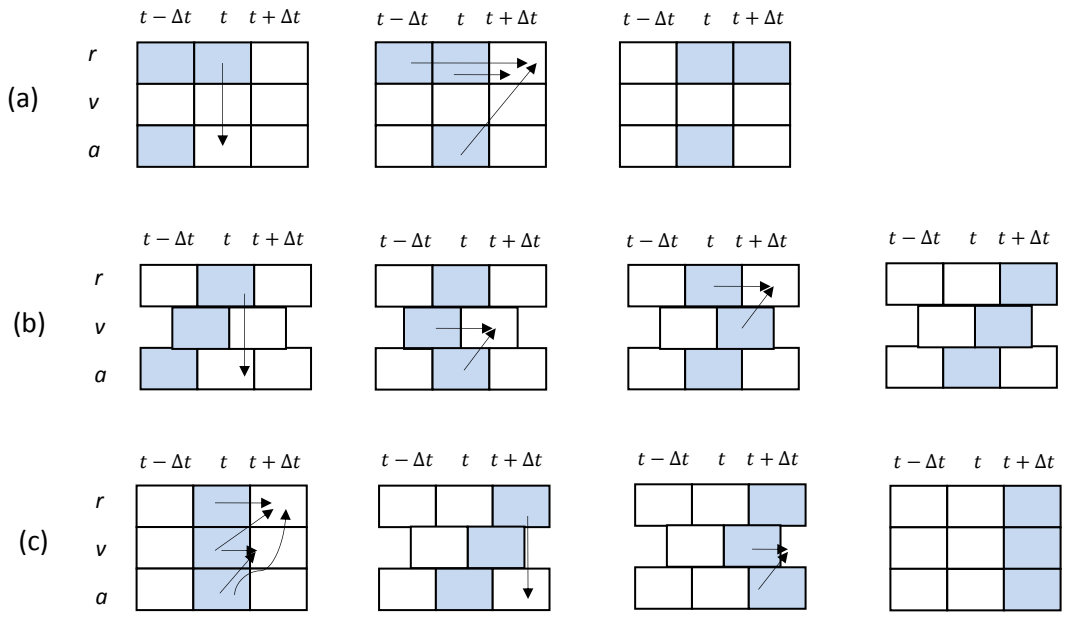


**Fig. 2–5: Schematic steps of three forms of the Verlet-likes algorithm. (a) Verlet's original method. (b) The Leap-Frog method. (c) The Velocity-Verlet form. We show successive steps in the implementation of each algorithm. In each case, the stored variables are in bleu boxes[30].**

## 2.4 Atomic interactions potentials

In most of the atomistic molecular modeling techniques, the first step is the determination of the interactions potentials. Potentials play an important role in determining the accuracy of the computer modeling studies[31].

Consider first the simple case of a system containing N atoms, the potential energy can be computed by summing all different types of interactions, which depending on the coordinates of individual atoms, pairs, triplets etc.:

$$U = \sum_i U_1(r_i) + \sum_i \sum_{j>i} U_2(r_i, r_j) + \sum_i \sum_{j>i} \sum_{k>j>i} U_3(r_i, r_j, r_k) + \cdots \qquad (2.18)$$

Where, *i, j, k* refers to the number of atoms. The $\sum_i \sum_{j>i}$ notation indicates a summation over all distinct pairs *i* and *j* without counting any pair twice; the same care must be taken for triplets etc. The first term signifies self-energies of the atoms which come from an external field (including, for example, the

container walls) on the system. The remaining terms represent particle interactions. The pair interaction represented by the second term$U_2$ is the most important, which depends only on the magnitude of the pair separation$r_{ij} = |r_i - r_j|$, so it may be written as$U_2(r_{ij})$. Compared with two body term $U_2$, the contribution of three-body term and four-body term is relatively small, and the calculation which involves a sum over triplets of molecules will be very time-consuming on a computer. That's why the three-body and higher terms are rarely included in computer simulations. We consider that there is no external potential, so no $U_1$ term, and the equation 2.15 will be written as:

$$\boldsymbol{U = \sum_i \sum_j U(r_{ij})} \qquad (2.19)$$

A mathematical approximation named Lennard-Jones potential has been proposed to illustrate the interaction between two non-ionic particles. The Lennard-Jones potential can rapidly evaluate the Van der Waals interactions for a large number of atoms. The Lennard-Jones potential is given by the following equation:

$$\mathbf{U(r_{ij}) = 4\varepsilon_{ij}\left[\left(\frac{\sigma_{ij}}{r_{ij}}\right)^{12} - \left(\frac{\sigma_{ij}}{r_{ij}}\right)^{6}\right]} \qquad (2.20)$$

Where ε is the well depth and a measure of how strongly the two particles attract each other, while $\varepsilon_{ij} = \sqrt{\varepsilon_i \varepsilon_j}$ ; σ is the distance at which the interatomic potential between the two particles is zero (Fig.2-6a), while $\sigma_{ij} = \frac{1}{2}(\sigma_i + \sigma_j)$; $r_{ij}$is the distance between the centers of two atoms. The Fig.2-6 shows a plot of the Lennard-Jones potential, which accounts for repulsion part and attraction part. Attraction occurs at short range, as the distance of separation increases by a few angstroms, the interaction rapidly decreases. Their potential energy comes to zero when two atoms are an infinite distance apart. When they approach to each other, the interaction increases. The atoms come closer together until they reach a region of separation where the two atoms become bounded and their bonding potential energy decreases from zero to a negative quantity. The distance of their centers will continue to decrease until they reach an equilibrium, which is specified by the separation distance at which the minimum potential energy is reached (Fig.2-6b). If we continue to push the two bound atoms, the electronic clouds surrounding the atoms start to overlap and then, repulsion occurs. The bonding

energy rises rapidly as the distance of separation between them decreases below the equilibrium distance (Fig. 2-6b).

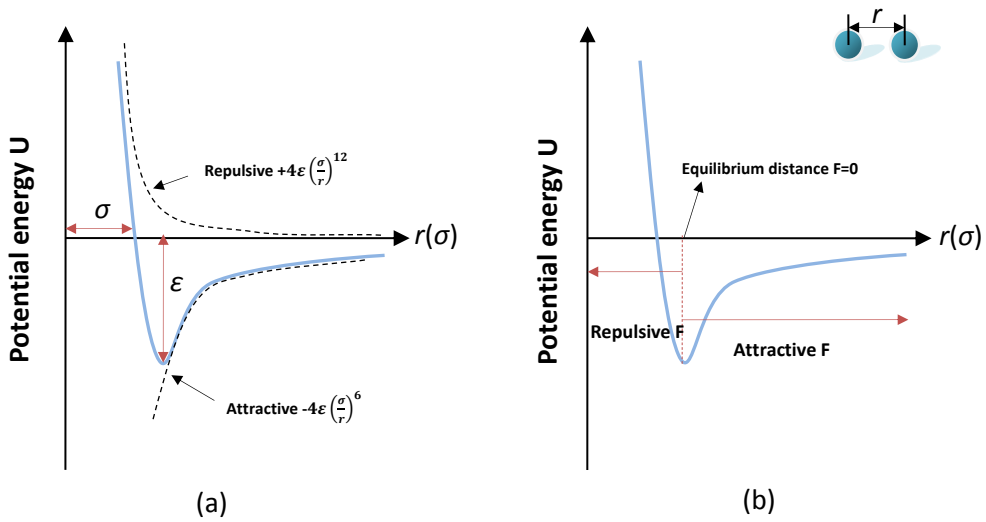


**Fig.2 − 6: Lennard-Jones potential between non-ionic atoms :( a) repulsive potential and attractive potential; (b) repulsive force and attractive force.**

There are many kinds of chemical bonds that exist between two-body, namely ionic bonds, covalent bonds, metallic bonds, hydrogen bonds, van der Waals bonds. When dealing with ionic systems, the Lennard-Jones potentials are not sufficient to represent the long range interactions. We have to involve the Coulomb interactions because they contribute the most to the total energy of the structure, whose form is defined by:

$$\mathbf{U^{Coulomb}(r_{ij}) = \frac{q_i q_j}{4\pi\varepsilon_0 r_{ij}}} \qquad (2.21)$$

Where$U^{Coulomb}$ is the Coulomb energy; $q_i$ et $q_j$ are the charges on ions *i* and *j;* $\varepsilon_0$is the permittivity of free space; $r_{ij}$is the inter-ionic distance.

## 2.5 Molecular interactions potentials

When dealing with molecular systems, there is no raison to abandon the atomic approach: chemical bonds are simply interatomic potential energy terms[32].

We have a wide variety of analytical forms of functions to define the interactions in a molecular system. These set of functions must be parameterised to give the correct energy and forces. The total

configuration energy of a molecular system can be calculated by summing the intra-molecular interactions and inter-molecular interactions:

$$\mathbf{U_{total} = U_{intra} + U_{inter}} \quad (2.22)$$

There are different kinds of interactions that exist in different substances for holding the material together.

### 2.5.1 Intra-molecular interactions

The interactions between the atoms within a molecule are called intra-molecular interactions. An intra-molecular interaction is for holding together the atoms making up a molecule or compound. It is important to note that there is no global specification of the intra-molecular interactions, all bonds, valence angles and dihedrals must be individually cited[33]. The intra-molecular energy of a molecular system can be written as:

$$\mathbf{U_{intra} = U_{bond} + U_{angle} + U_{dihed} + U_{inv}} \quad (2.23)$$

Where $U_{bond}$, $U_{angle}$, $U_{dihed}$ and $U_{inv}$ are empirical interaction functions representing chemical bonds, valence angles, dihedral angles and inversion angles. Generally, these four terms contribute to the short range interactions. They are illustrated in Fig.2-7.

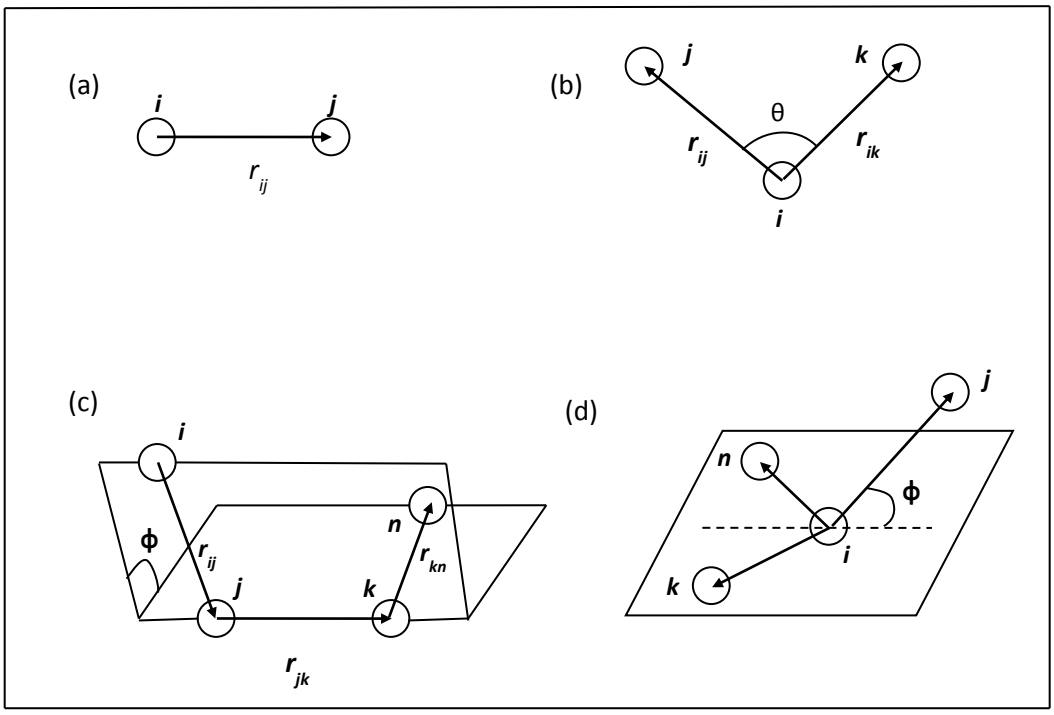


**Fig. 2–7: Intra molecular interactions: (a) the vector for chemical bond; (b) the valence angle and associated vectors; (c) the dihedral angle and associated vectors; (d) the inversion angle and associated vectors.**

The bond potentials describe explicit bonds between specified atoms (Fig.2-7a). They are functions of the inter-atomic distance only. Three approximation popularly used are Harmonic bond, 12-6 potential bond and Buchkingham potential. The potential functions are given by:

1. Harmonic bond :

$$\mathbf{U(r_{ij}) = \frac{1}{2} k(r_{ij} - r_0)^2} \qquad \textbf{(2.24)}$$

2. 12-6 potential bond:

$$\mathbf{U(r_{ij}) = \left(\frac{A}{r_{ij}^{12}}\right) - \left(\frac{B}{r_{ij}^{6}}\right)} \qquad \textbf{(2.25)}$$

3. Buckingham potential :

$$\mathbf{U(r_{ij}) = A \exp\left(-\frac{r_{ij}}{\rho}\right) - \frac{C}{r_{ij}^{6}}} \qquad \textbf{(2.26)}$$

Where $r_{ij}$ is the distance between atoms labelled *i* and *j* in the molecule and all the others are the parameters of the potentials function.

The valence angle potentials describe the bond bending terms between the specified atoms (Fig.2-7b). Three body terms will provide the angular constrains. For example, when to model the bending of O-Si-O bonds of tetrahedral sheet, the three body potentials were employed. The general expression for this potential is given by Harmonic:

$$\mathbf{U(\theta_{jik}) = \frac{k}{2}(\theta_{jik} - \theta_0)^2} \qquad \textbf{(2.27)}$$

With $\theta_{jik}$ is the angle between atom j,i and k in the molecule, k (in kcal.mol-1) and $\theta_0$ (en $^o$) are the parameters depending on the molecules.

The dihedral angle potentials describe the interaction arising from torsion forces in molecules. They require the specification of four atomic positions. While the inversion angle potentials describe the interaction arising from a particular geometry of three atoms around a central atom. They are illustrated in Fig.2-7c and Fig.2-7d, respectively. The expressions for these two potentials are given in the same form by:

$$\mathbf{U(\Phi_{ijkn}) = A[1 + cos(m\Phi_{ijkn} - \delta)]} \qquad \textbf{(2.28)}$$

Where $\Phi_{ijkn}$ is the torsion angle formed by four atoms shown in Fig.2-7c and Fig.2-7d. A is an energy parameter (kcal.mol$^{-1}$), $\delta$ is the phase factor (in $^o$) which represents the angle when torsion energy reachs its minimum, and m is the multiplicity.

### *2.5.2 Inter-molecular interactions*

The forces holding molecules together are generally called intermolecular forces. The energy requires to break molecules apart is much smaller than typical intra-molecular forces energy, but inter-molecular forces play important roles in determining the properties of a substance. In general, intermolecular forces can be divided into electrostatic interactions and Van der Waals interactions:

$$\mathbf{U_{intermolecular} = U_{Coulomb} + U_{vdw}} \qquad \textbf{(2.29)}$$

Van der Waals interactions play a vital role in estimating the location and shape of the minimum energy which is general when applied to interactions occurring between neutral species (molecules or atoms), and arising from their permanently or transiently polarized electron distributions. The Van der

Waals interaction between two particles arises from a balance between repulsive and attractive forces. As we discussed above in section 2.4, the repulsive force arises at short distances where the electron-electron interaction is strong, and attractive force arises at greater distances. Three most popularly used Van der Waals potentials are 12-6 potential, Lennard-Jones potentials and Buckingham potential. The expressions for these potentials are already discussed above in equation 2.25, 2.20 and equation 2.26:

1. 12-6 potential:

$$\mathbf{U}(\mathbf{r_{ij}}) = \left(\frac{\mathbf{A}}{\mathbf{r_{ij}^{12}}}\right) - \left(\frac{\mathbf{B}}{\mathbf{r_{ij}^{6}}}\right)$$

2. Lennard-Jones potential:

$$\mathbf{U}(\mathbf{r_{ij}}) = \mathbf{4\varepsilon_{ij}}\left[\left(\frac{\boldsymbol{\sigma}_{\mathbf{ij}}}{\mathbf{r_{ij}}}\right)^{\mathbf{12}} - \left(\frac{\boldsymbol{\sigma}_{\mathbf{ij}}}{\mathbf{r_{ij}}}\right)^{\mathbf{6}}\right]$$

3. Buckingham potential:

$$\mathbf{U}(\mathbf{r_{ij}}) = \mathbf{A}\,\mathbf{exp}\left(-\frac{\mathbf{r_{ij}}}{\boldsymbol{\rho}}\right) - \frac{\mathbf{C}}{\mathbf{r_{ij}^{6}}}$$

The electrostatic interaction between two atoms is calculated by the Coulomb's law which we have discussed above in section 2.4, whose expression is as follows:

$$\mathbf{U^{Coulomb}}(\mathbf{r_{ij}}) = \frac{\mathbf{q_i q_j}}{\mathbf{4\pi\varepsilon_0 r_{ij}}}$$

For a molecular system, the knowledge of the charge distribution is essential for determining the electrostatic energies in Monte Carlo and molecular dynamics calculations. The accuracy with which these methods can derive physical properties of solids, liquids, and solutions is critically dependent on the atomic charges used[34]. The description of the molecular charge distribution may be improved somewhat by incorporating point multipole moments at the centre of charge. These multipoles may be equal to the known (isolated atom) values, or may be 'effective' values chosen simply to yield a better description of the thermodynamic properties. In order to approximate the complete charge distribution in the molecule, an approach to use a set of fictitious 'partial charges' for ionic and polar system has been proposed. These 'partial charges' will be distributed 'in a physically reasonable way' around the molecule so as to reproduce the known multipole moments[35], and a further refinement is to distribute fictitious multipoles in a similar way. For example, the electrostatic interaction between methane molecules may be modelled using five partial charges, a tetrahedral arrangement of partial

charges is illustrated in Fig2-8, where there is one charge at the centre and four other charges at the positions of the hydrogen nuclei. A typical value is z=0.143 giving O=5.77×$10^{-50}$ $cm^3$ with the octopole moment is given by[36]:

$$O = \frac{5}{2}\sum_{a=1}^{5} z_a r_{ax} r_{ay} r_{az} \qquad \textbf{(2.30)}$$

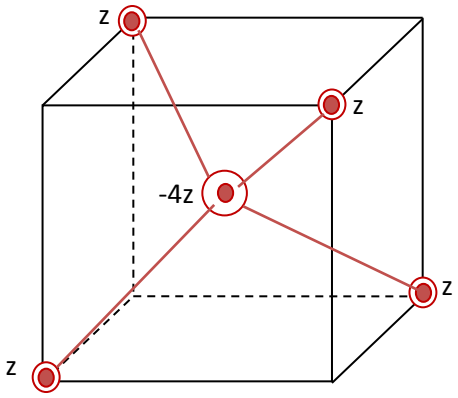


**Fig2–8: A five-charge model for $CH_4$.**

In a potential energy calculation, the electrostatic interaction between partial charges on different molecules would be summed in the same way as the other site-site interactions.

# Chapter 3. System set up and data analysis

## 3.1 System set up

### *3.1.1 Ensembles*

Statistical mechanics provides the link between the classical microscopic world described by Newton's laws of motion and the macroscopic observables that are actually measured in experiments, including thermodynamic, structural and dynamical properties.

Although the enormous quantity of microscopic information is certainly sufficient to predict any macroscopic observable, there are many microscopic configurations of a system that lead to the same macroscopic properties. For example, if we connect the temperature of a system to an average of the kinetic energy of the individual particles composing the system, then there are many ways to assign the velocities of the particles consistent with a given total energy such that the same total kinetic energy and, hence, the same measure of temperature is obtained. Suppose we aimed to predict macroscopic time-dependent properties, we start with a large set of initial conditions drawn from a state of thermodynamic equilibrium, and if we launched a trajectory from each initial condition in the set, then the resulting trajectories would all be unique in phase space. Despite their uniqueness, these trajectories should all lead, in the long time limit, to the same macroscopic dynamical observables such as vibrational spectra, diffusion constants and so forth[37].

An ensemble is a collection of systems, whose thermodynamic state is defined by a common set of macroscopic properties, such as the same total energy, volume and number of atoms. Macroscopic thermodynamics properties, such as density, diffusion coefficient, heat capacity etc. can be calculated by performing average over the systems in the defined ensembles. In classical ensemble theory, every macroscopic observable of a system is directly connected to a microscopic function of the coordinates and momenta of the system.

There are three ensembles which are in common use in MD and MC: the microcanonical NVE, the canonical NVT and the isothermal NPT.

- Microcanonical ensemble (NVE)

The microcanonical ensemble is considered to be the most fundamental equilibrium ensemble. In this ensemble, number of atoms (N), volume (V) and energy (E) of the system are maintained constant. A microcanonical molecular dynamics trajectory may be seen as an exchange of potential and kinetic energy, with total energy being conserved. The system in the microcanonical ensemble is isolated from any surroundings. Its main disadvantage is that conditions of constant total energy are not those under which experiments are performed.

- Canonical ensemble (NVT)

In order to reflect more common experimental setups, ensembles that have different sets of thermodynamic control variables have been developed. The Canonical ensemble is an example. The thermodynamic control variables in the canonical ensemble are constant particle number (N), constant volume (V) and constant temperature (T), which characterize a system in thermal contact with an infinite heat source.

- Isothermal-Isobaric ensemble (NPT)

The Isothermal-Isobaric ensemble is one of the most important ensemble, in which the particle number (N), pressure (P) and temperature (T) are conserved. It corresponds most closely to conditions of constant temperature and pressure under which many experiments are performed.

### *3.1.2 Periodic boundary conditions*

Computer simulations are usually performed on a relatively small number of molecules, $10 \leqq N \leqq 10000$[30]. The size of the system is limited by the available storage on the host number. If we expect to simulate real bulk material consist of milliards of particles. It is obvious that such simulations cannot be handled by any computer. This problem of limit of simulation size can be solved by using periodic boundary conditions. Then we can simulate a large system by modeling a small simulation box that is far from the edge of the system. Around the simulation box there are exactly similar virtual box which replicate throughout space to from an infinite lattice. There is no need to simulate the virtual box because it is similar to the original one at all times. During the simulation, as a particle moves in the original simulation box, its periodic image in each of the neighbouring boxes moves in exactly the same

way. Thus, as a particle floats out from the central simulation box, another particle floats in through the opposite boundary from the virtual box at the same time. The number of particles in the simulation box is thus conserved. Only the properties of the unit cell need to be recorded and propagated. A two-dimensional version of such a periodic system is illustrated in Fig3-1, where particles can enter and leave the box across each of the four boundaries. A similar analogy exists for a three-dimensional periodic system, the central simulation box replicate throughout space in x,y,z direction to form an infinite lattice. The particles would be free to cross any of the six cube boundaries during the simulation.

Two-dimensional periodic boundary conditions are generally used for performing the simulations of planar surface, such as the simulation of adsorption which aim to calculate the interfacial forces of two different surfaces. The simulation box replicate in the x- and y- dimensions to form a thin slab while leaving the z-boundary open. Three-dimension periodic boundary conditions are particularly useful for simulating a bulk system with no existing surface.

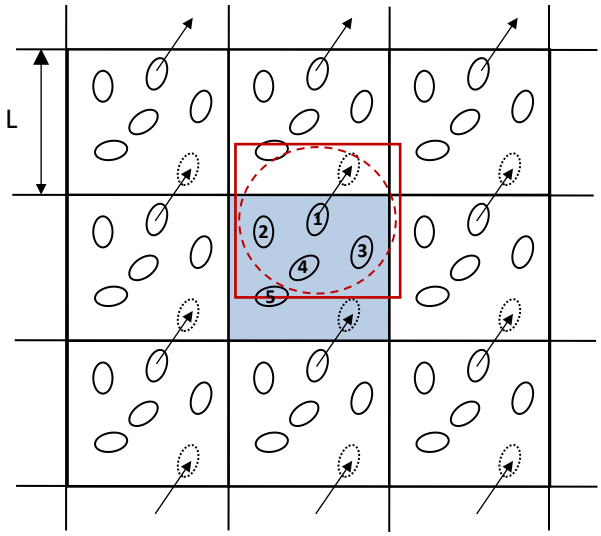


**Fig.3 – 1: A two-dimensional periodic system. All boxes have the same movement as central simulation box. The red box represents the minimum image convention for molecule 1. The dashed circle represents a potential cutoff.**

It is important to ask if the properties of a small, infinitely periodic system, and the macroscopic system which it represents, are the same. This will depend on both the range of the intermolecular potential and the phenomenon under investigation. But we remark that the common experience in simulation work is that periodic boundary conditions have little effect on the equilibrium

thermodynamic properties. If the resources are available, it should be standard practice to increase the number of molecules and the box size so as to maintain constant density.

Now we must think about the question of calculating properties of systems subject to periodic boundary conditions. The calculation of the potential energy of a particular configuration is the heart of the MC and MD programs. In the case of MD program, most time is spent for calculating the interactions. In order to calculate the force on a certain molecule, we must include interactions between this molecule and every other molecule in the simulation box and also every other molecules lying in the surrounding virtual boxes. This infinite number of terms is impossible to calculate in practice. We can make an approximation called 'minimum image convention' to simplify the calculation. In this approximation, we consider molecule 1 maintained at the centre of a region which has the same size and shape as the basic simulation box(see the red box in Fig.3-1). Molecule 1 interacts with all the molecules whose centres lie within this region, which is with the closest periodic images of the other N-1 molecules if we have N molecule in total in the simulation box. So in the minimum image convention, the calculation of the potential energy due to two-body interactions involves $\frac{1}{2}N(N-1)$ terms. However for a system of about 1000 particles, this may still be a very substantial calculation. In order to improve this situation, a further approximation called 'spherical cutoff' has been developed. In this approximation, we apply a spherical cutoff to the molecule of interest for short-range forces. This means that only the pair potential for $r \leqslant r_c$ will be considered, where $r_c$ is the cutoff distance represented by the dashed circle in Fig.3-1. The number of neighbours explicitly considered is reduced by a factor of approximately $\frac{\frac{4}{3}\pi r_c^3}{L^3}$, and this may be a substantial saving. The cutoff distance should be sufficiently large to ensure the reliability of the potential calculation. The cutoff distance must be small or equal to 0.5L for consistency with the minimum image convention.

### *3.1.3 Molecular force fields*

In the simple systems, the interactions between particles are composed of long-range forces of electrostatic and Van der Waals interactions which are described by Coulomb's law and a Lennard-Jones

potentials, respectively. This may be a very useful approximation for independent shapeless particles without any internal structure. However, this simple model is not accurate enough for simulating the internal structure of real molecules. So we need to consider a wide variety of molecular force fields.

The force field (FF) method, also known as the molecular mechanics (MM) method, is a purely classical ball-and –spring model. The bond distances, bond angles and all the non-bonded inter-atomic interactions are described as classical springs with a characteristic equilibrium value and stiffness. A collection of spring constants for all types of interactions that are known to the program is called a force field. The force field is used in simulations to calculate the internal potential energy of a system. The FF method is purely classical and the electrons are not involved into the model at all and therefore estimates of the charge distributions cannot be obtained. The partial charges, which we have discussed above at the end of chapter 2, are usually assigned to all centres.

In this work, a general force field, CLAYFF[5] has been employed. It is a theoretical molecular model useful for a fundamental atomic-level understanding, and suitable for the simulation of hydrated and multicomponent mineral systems and their interfaces with aqueous solutions. In this approach, most interatomic interactions are nonbonded, all atoms are represented as point charges and are allowed complete translational freedom. The empirical parameters are optimized on the basis of known mineral structures, and partial atomic charges are derived from periodic DFT quantum chemical calculations of simple oxide, hydroxide, and oxhydroxide model compounds with well-defined structures[5].

CLAYFF is based on the single point charge (SPC) water model to represent the water, hydroxyl, and oxygen-oxygen interactions. This water model has been successfully used in a variety of molecular simulations to evaluate water structure and properties and for the interaction of water with hydroxide mineral surfaces. Compared to the more complex water models such ad TIP4P, BJH etc., the SPC is relatively simple in having partial charges centered directly on each of three atoms, and the short-range interactions represented by a simple Lennard-Jones term. Bond stretch and bond angle terms are introduced into the SPC water model using the expressions determined by Teleman et al[38] to ensure full flexibility for the water and hydroxide components.

In this CLAYFF model, the short-range interactions of all atoms are represented by simple Lennard-Jone potential. The total potential energy for our molecular simulation system is expected to have contributions from the Coulombic (electrostatic) interactions; the short-range interactions, the bonded interactions and the angle bend interactions:

$$\mathbf{E_{total}} = \frac{\mathbf{e^2}}{\mathbf{4\pi\epsilon_o}} \sum_{\mathbf{i\neq j}} \frac{\mathbf{q_i q_j}}{\mathbf{r_{ij}}} + \sum_{\mathbf{i\neq j}} \mathbf{D_{o,ij}} \left[ \left( \frac{\mathbf{R_{o,ij}}}{\mathbf{r_{ij}}} \right)^{\mathbf{12}} - \mathbf{2} \left( \frac{\mathbf{R_{o,ij}}}{\mathbf{r_{ij}}} \right)^{\mathbf{6}} \right] + \mathbf{k_1} \left( \mathbf{r_{ij}} - \mathbf{r_o} \right)^{\mathbf{2}} + \mathbf{k_2} \left( \boldsymbol{\theta}_{\mathbf{ijk}} - \boldsymbol{\theta}_{\mathbf{o}} \right)^{\mathbf{2}} \quad \textbf{(3.1)}$$

Where the sums are over all lattice and water interaction sites and $r_{ij}$ is the distance between atoms *i* and *j*. The first term represents the Coulombic energy, where $q_i$ and qj the partial charges which are derived from quantum mechanics calculations, e is the charge of the electron and and $\epsilon_o$ is the dielectric permittivity of free space ($8.85419\times10^{-12}$F/m). The second term is the Van der Waals energy, which is represented by the Lennard-Jones (12-6) function, including the short-range repulsion associated with the increase in energy as two atoms approach each other and the attractive dispersion energy, where $D_{o,ij}$ and $R_{o,ij}$ are respectively the energy and distance parameters for the unlike atoms with:

$$\mathbf{R_{o,ij}} = \frac{\mathbf{1}}{\mathbf{2}} \left( \mathbf{R_{o,ii}} + \mathbf{R_{o,jj}} \right) \quad \textbf{(3.2)}$$

$$\mathbf{D_{o,ij}} = \sqrt{\mathbf{D_{o,ii} D_{o,jj}}} \quad \textbf{(3.3)}$$

The bond stretch energy of the hydroxyl groups like O-H bonds in this work is described by the third term where $k_1$ is a force constant and $r_o$ represents the equilibrium bond length. The three-body energy can be described by the last term where $k_2$ is a force constant. $\theta_{ijk}$ represents the bond angle and $\theta_o$ is the equilibrium bond angle.

## 3.2 Data analysis

### *3.2.1 Radial distribution function*

The Radial Distribution Function g(r), also known as the pair distribution function, is an important way to characterize the distribution of particles on a two-dimensional plane or in a three-dimensional

space during the molecular dynamics simulations. The g(r) represents the probability to find an atom in a shell Δr at the distance r of another atom chosen as a reference point. This describes how the atoms are radially packed around each other in a system where there is continual movement of the atoms.

It is not difficult to construct an RDF. Chosen an atom in the system and draw around it a series of concentric spheres, set at a small fixed distance Δr apart. At regular intervals a snapshot of the system is taken and the number of atoms found in each shell is counted and stored. At the end of the simulation, the average number of atoms in each shell is calculated. We obtain then the RDF by dividing by the volume of each shell and the average density of atoms in the system, which mathematically can be expressed as:

$$\mathbf{g(r) = \frac{\rho(r)}{\rho} = n(r)/(\rho\, 4\pi r^2 \Delta r)} \qquad \textbf{(3.4)}$$

Where ρ(r) is the local time-averaged density at the distance r from a reference particle, ρ is the average density of particles equal to N/V, n(r) is the number of atoms in a shell of width Δr at distance r and g(r) is the RDF. This simplified definition holds for a homogeneous and isotropic system.

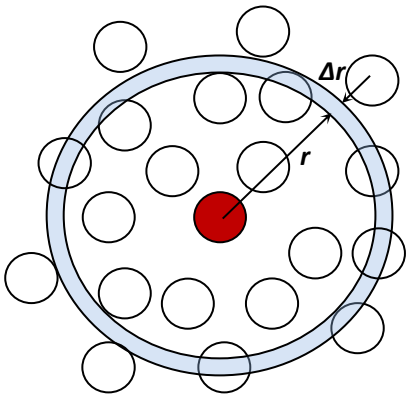


**Fig. 3–2: Schematic representation of RDF.**

For a more general case of molecular dynamics simulations, let us consider a system of N particles in a volume V (for an average number density ρ=N/V), and at a temperature T (let us also define β=1/KT). The potential energy due to the interaction between particles is $\mathbf{U(r_1, r_2, r_3, \dots, r_N)}$, and the pair distribution function in canonical ensemble is obtained according to such formula:

$$\mathbf{g(r) = \frac{N(N-1)}{\rho^2 Z_{NVT}} \int e^{-\beta U(r_1, r_2, r_3, \dots, r_N)} dr_3 \dots dr_N} \qquad \textbf{(3.5)}$$

Where $Z_{nvt}$ is the configuration integrals for system in NVT ensemble. This function depends only on the relative distance ***r*** between two particles. We integrate the configurationally distribution function over the positions of all atoms except two, incorporating the appropriate normalization factors[39].

The RDF is usually plotted as a function of the interatomic separation r. A typical RDF plot (Fig.3-3a) for liquid shows a number of important features. Firstly, at very short separations the RDF must be zero, because two particles cannot approach any more closely to occupy the same space. Secondly, a number of obvious peaks appear which indicates that the atoms pack around each other in 'shells' of neighbours. The occurrence of peaks at long range indicates a high degree of ordering. Usually, at high temperature the peaks are broad, indicating thermal motion, while at low temperature they are sharp. They are particularly sharp in crystalline materials, where atoms are strongly confined in their positions. g(r) go to 1 for long separation, which happens because the RDF describes the average density at this range[40].

The RDF for a perfectly ordered crystalline lattice is shown in Fig.3-3b, the g(r) go to zero after the first peak because the crystalline is perfectly ordered.

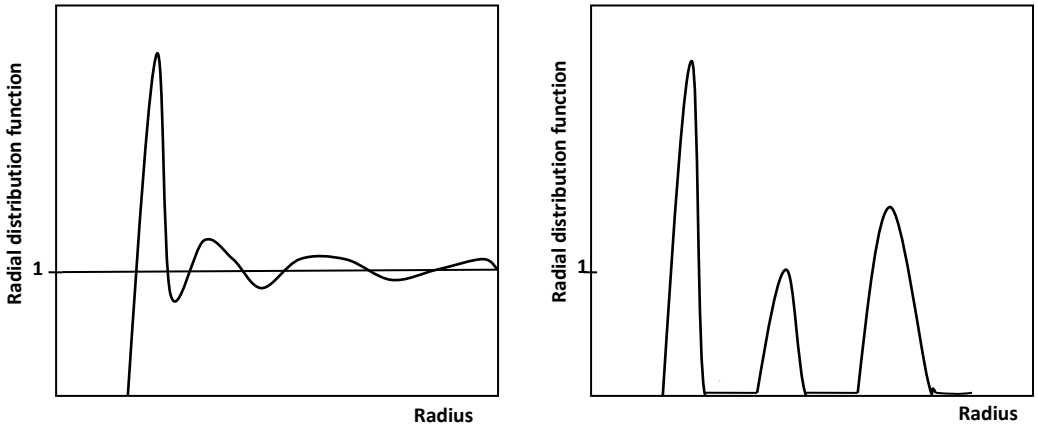


(a) (b)

**Fig.3–3: Typical RDFs plot :(a) RDF for liquid schematically; (b)RDF of a periodic solid.**

### *3.2.2 Self-diffusion coefficients*

The self-diffusion coefficient Ds is used to describe the diffusive behaviour of individual particles. In an isotropic three-dimensional material, a three-dimensional Einstein relation was used to calculate the self-diffusion coefficient which is related to the mean-squared displacement of particle after time *t*:

$$\mathbf{D_s = \lim_{t\to\infty} \frac{1}{6Nt} \langle \sum_{i=1}^{N} |\vec{r_i}(t) - \vec{r_i}(0)|^2 \rangle} \qquad \textbf{(3.6)}$$

Where N is the total particle number, t is the simulation time, $\vec{r_i}(t)$ is the position of particle i at time *t.* $\langle |\vec{r_i}(t) - \vec{r_i}(0)|^2 \rangle$ is the mean-square displacement of the particle i and the angular brackets indicate an ensemble average. Equation 3.6 easily can be generalized to determine the x,y or z component of a diffusivity by replacing the factor of 6 by a factor of 2 and by using the desired component of position instead of the position vectors[41].

When applying this expression one must remove the wrap-around effects and let the particles to propagate beyond the boundaries. This implies that the long-range effects are limited to distances that correspond the simulation box dimension. For very long distances the diffusion coefficient will go to zero.

The Green-kubo relation is another equivalent diffusion coefficient, which is based on the velocity autocorrelation function:

$$\mathbf{D_s = \frac{1}{3N} \int_0^\infty \langle \sum_{i=0}^{N} \vec{v_i}(t) * \vec{v_i}(0) \rangle dt} \qquad \textbf{(3.7)}$$

With $\vec{v_i}(t)$ the velocity of particle i at time t and $\sum_{i=0}^{N} \vec{v_i}(t) * \vec{v_i}(0)$ is called Velocity autocorrelation function. This formula does not require special treatment of the wrapping around at the boundary conditions. However, as long as the velocities are correlated the trajectories must be calculated quite accurately. The main uncertainty in the velocities when using a pair potential, such as the Lennard-Jones potential, the main source of uncertainty is the steep repulsive part of the potential, not the cut-off error. This mimics the natural behaviour of the sample.

### *3.2.3 Root-mean-square deviation (RMSD) and root-mean-square fluctuation (RMSF)*

As we mentioned above, the molecular dynamics simulations is a useful method in providing information about dynamics of the system. The field of study is not limited to equilibrium properties such as structure and thermodynamic functions of the system. One can try investigating evolution of non-equilibrium system in time. The most popular of such measure is the root-mean-square deviation

(RMSD) and root-mean-square fluctuation (RMSF). The RMSD of certain atoms in a system with respect to a reference structure (often the starting structure), $r^{ref}$, is calculated as:

$$\mathbf{RMSD(t)} = \left[\frac{1}{N}\sum_{i=1}^{N}\left(\mathbf{r_i^t} - \mathbf{r_i^{ref}}\right)^2\right]^{1/2} \quad \textbf{(3.8)}$$

where N is the number of particles in system, $r_i^{ref}$ is the position of atom i at reference time and $r_i^t$ is the position at time t after least square fitting the structure to the reference structure.

The RMSF is a measure of the deviation between the position of particle i and some reference position:

$$\mathbf{RMSF(i)} = \left[\frac{1}{T}\sum_{t_j=1}^{T}\left|\mathbf{r_i(t_j)} - \mathbf{r_i(t^{ref})}\right|^2\right]^{1/2} \quad \textbf{(3.9)}$$

Where T is the time over which one wants to average and $r_i(t^{ref})$ is the reference postion of particle i. Typically this reference position will be the time-averaged position of the same particle i. The difference between RMDS and RMSF is that, the latter is averaged over time, giving a value for each particle i. For the RMSD the average is taken over the particles, giving time specific values.

# *Part II* : Results

# Chapter 4. Uranyl adsorption on (001) surfaces of Kaolinite: A molecular dynamics study

## 4.1 Abstract

The aim of this chapter is to investigate the adsorption of uranyl species $(UO_2)^{2+}(H_2O)_5$ onto kaolinite (001) surfaces. To this end we have employed molecular dynamic simulations based on CLAYFF force field potential. Various types of surface model for inner-sphere adsorption complexes and one model for outer-sphere adsorption complexes were optimized. In order to have a neutral structure, the uranyl $(UO_2)^{2+}(H_2O)_5$ or the kaolinite was deprotonated to form the outer-sphere or inner-sphere adsorption complexes. Both singly protonated and partially depronated states of the Al(O) kaolinite surface were considered for adsorption in the model of inner-sphere complexes. The first uranyl coordination shell exhibits pentagonal bi-pyramidal symmetry with the pentagonal formed by 5 water molecules. We show that the average U-Ow distances are between 2.49 and 2.57 Å for water molecules. The bond of uranyl with deprotonated $O^-$ center is always short because of the charge attraction. The obtained results agree well with density functional calculations and EXAFS measurements, and show how and why the adsorption of uranyl appears on the surface of kaolinite.

## 4.2 Introduction

In order to predict and regulate the environmental impact of human activities such as uranium mining and radioactive waste disposal, it is necessary to understand the behavior of actinides in the environment because their interaction with clay mineral is an important factor to control the migration of radionuclide in the environment. The behavior of actinides in the soil is mainly the surface adsorption interactions witch change the forms of radioactive elements and reduces the mobility of actinides in the natural systems. Therefore, it is important to search how the actinides interact with clay mineral such as the fundamental process of surface complexation and surface precipitation.

As we mentioned above in the general introduction part, Uranium is a chemical element in the actinide series of the periodic table. It is a metallic unstable and weakly radioactive. In nature, uranium is found mostly as uranium-238 which exists in soils and groundwater. Uranium mine is the main element in the nuclear fuel cycle and it is also a major component of the waste product ($UO_2$ > 95%) of the nuclear industry, the most stable chemical form of dissolved uranium is the uranyl ion $UO_2^{2+}$, which is potentially very mobile to complexate with organic and inorganic matter in the environment. Therefore, uranium and its decay products are hazardous pollutants of the environment. To try to protect environment and human, the adsorption properties of hexavalent uranyl species, $UO_2^{2+}$, have been most extensively studied. Such as the research in the geologic disposal of nuclear waste, we found that the clay minerals have low permeability, high adsorption capacity and plasticity which make them able to fix effectively radioactive waste to avoid their transport in groundwater. The clay minerals are highly sorptive due to their small particle sizes, large surface areas and chemically active surface defect sites. Natural clays as the adsorbent with a low cost have received much attention on heavy metals sorption from contaminated water.

In recent 30 years, the structure of uranyl in aqueous solution has been widely investigated both through experimental and theoretical techniques. The coordination data has been obtained by different methods such as extended X-ray adsorption fine-structure (EXAFS) [42-45] measurements, 'H-NMR research [44], as well as the Molecular Dynamics method [46]. These studies suggest that $UO_2^{2+}$

coordinated mostly to 5 water molecules in aqueous solution [44], although a small percentage of the uranyl ions are coordinated to four waters. The typical U-$H_2O$ distance within the water structure and the hydrated $UO_2^{2+}$ group are expected to be about 2.50 Å and the U-O distance within the hydrated $UO_2^{2+}$ are expected to be about 1.8 Å. Kremleva et al. have studied uranyl adsorption at (001) surfaces of kaolinite using first-principles density functional calculation.

Numerous studies of uranyl sorption on various mineral surfaces have been published [47-52] by different methods such as X-ray adsorption fine-structure (EXAFS) [50-52] as well as experiments. The adsorption behavior of uranyl on kaolinite surfaces is affected by numbers of parameters such as the pH of the solution, as well as the concentration of uranyl and different counterions in solution: uranyl sorption increases with pH, achieve saturation at pH=7 [53-55].

In this work, we used Molecular Dynamic simulations to study the molecular coordination of dissolved uranyl and the sorption of dissolved Uranyl on the surface of Kaolinite at neutral pH. This was done by inclusion of deprotonated form of Al-$OH^-$ leading to negatively charged Al-$O^{2-}$ and Si-OH resulting in the negatively charged Si-$O^-$. We examine here both inner- and outer-sphere complexes at the basal Al (o) (001) surface of kaolinite. Furthermore, we test the effect of different NVE and NVT ensembles.

## 4.3 Data preparation for adsorption modeling

### *4.3.1 Crystal structure of kaolinite*

Kaolinite is a 1:1 clay that is widely distributed in the environment. It is a non-swelling clay, with the ideal chemical composition $Al_4Si_4O_{10}(OH)_8$ per unit cell, which is characterized by the parameters a=5.17 Å, b=8.97 Å, c=7.39 Å, and α=91.40°, β=104.85°, γ=89.71°. The coordinates of atoms in the clay crystal structure of one unit-cell of Kaolinite are presented in Table 4-1. The Kaolinite structure consists of a repeating siloxane silicon tetrahedral ($Si_2O_5$) sheet and a gibbsite-type aluminum octahedral ($Al(OH)_3$) sheet. In the Si tetrahedral sheet, each Si connected to three Si by sharing oxygen atoms forming the siloxane surface. This arrangement creates hexagonal cavities on the surface. In the Al octahedral sheet,

each Al is coordinated by two vertex oxygen atoms of the siloxane and shares four hydroxyls with neighboring aluminum atoms. Three of these four hydroxyls are oriented toward the extern Al surface forming the gibbsite surface while the fourth one is oriented inward in the direction of the siloxane cavity[15, 56-58]. These two sheets are bonded through shared oxygen atoms (Fig4-1). For the Kaolinite clays, there is little isomorphic substitution for Al in the octahedral positions and for Si in the tetrahedral positions which accounts for a small cation exchange capacity (CEC) value when compared with other swelling clay minerals [59, 60]. However, kaolinite has high retention capacity to many nuclear and nuclear water sites, which is important in the migration of contaminants over distances measured in kilometers. This retention capacity is due to its chemical active of surface defect sites.

**Table 4-1: Atomic positions in the unit cell of Kaolinite mineral layer, with O1 the hydroxyl oxygen and O2 the bridging oxygen.**

| Atom | x(Å) | y(Å) | z(Å) | Atom | x(Å) | y(Å) | z(Å) |
|---|---|---|---|---|---|---|---|
| **Al** | -1,03 | -0,03 | -0,23 | **Al** | 1,59 | -1,53 | -0,34 |
| **Al** | 1,58 | 4,46 | -0,23 | **Al** | -0,97 | 2,96 | -0,34 |
| **Si** | -1,81 | -1,31 | -3,05 | **Si** | 0,79 | 3,16 | -3,05 |
| **Si** | 0,83 | -2,87 | -3,05 | **Si** | -1,73 | 1,62 | -3,05 |
| **O2** | -1,94 | -1,18 | -1,46 | **O2** | 0,67 | 3,31 | -1,46 |
| **O2** | -1,57 | 1,60 | -1,46 | **O2** | 0,99 | -2,89 | -1,46 |
| **O2** | 1,70 | 0,03 | -3,73 | **O2** | -0,91 | -4,46 | -3,72 |
| **O2** | -2,34 | -2,31 | -3,53 | **O2** | 0,27 | 2,18 | -3,53 |
| **O2** | -2,32 | 2,37 | -3,72 | **O2** | 0,24 | -2,12 | -3,72 |
| **O1** | -1,88 | 4,45 | -0,95 | **O1** | 0,68 | -0,03 | -0,95 |
| **O1** | 2,06 | -3,00 | 0,67 | **O1** | -0,50 | 1,49 | 0,67 |
| **O1** | -2,57 | -0,36 | 0,69 | **O1** | 0,04 | 4,13 | 0,69 |
| **O1** | -2,52 | 3,24 | 0,60 | **O1** | 0,04 | -1,25 | 0,60 |
| **H** | -1,45 | -3,68 | -0,82 | **H** | 1,16 | 0,80 | -0,81 |
| **H** | 2,44 | -2,94 | 1,57 | **H** | -0,12 | 1,54 | 1,57 |
| **H** | 2,30 | -0,07 | 1,58 | **H** | -0,26 | 4,41 | 1,58 |
| **H** | -0,03 | -1,59 | 1,51 | **H** | 2,58 | 2,90 | 1,51 |

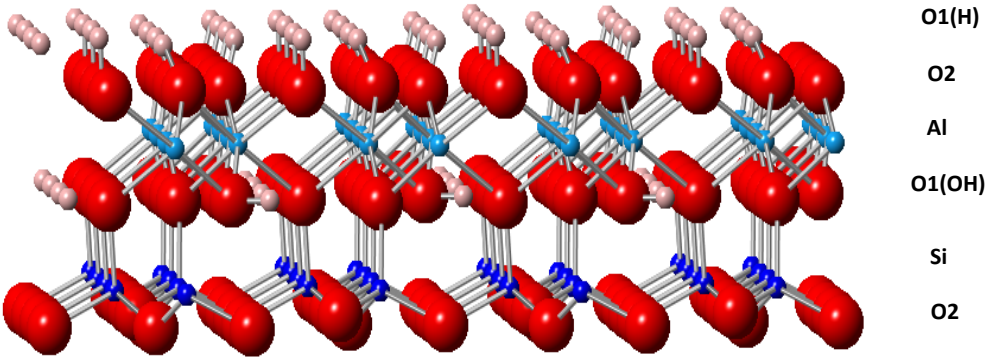


**Fig.4–1: Side view of single layer kaolinite structure.**

We used a repeating supercell containing 16 kaolinite unit cells (4×4×1 units in the a,b and c dimensions). The corresponding supercell dimensions are a = 20.68 Å, b = 35.88 Å, c = 7.39 Å, which consists of 544 atoms: 64 Al, 64 Si, 288 O and 128 H. All species were treated as rigid bodies beside the H atoms and uranyl molecule.

### *4.3.2 Preparation of $(UO_2)^{2+}(H_2O)_5$ species*

In order to have the $(UO_2)^{2+}(H_2O)_5$ species, five SPC water molecules were put randomly in a cubic simulation box with edge lengths of 15 Å. A single Uranyl ion was displaced in the center of the simulation box. The initial coordination is shown in Table 4-2. The systems were first equilibrated at 300K for 100ps and followed by 100ps of MD simulations in NVE ensemble. Potential parameters for the uranyl ions and SPC water molecules are shown in Table4-3. These parameters for uranyl result in a 5-fold-coordnation hydration shell in the equatorial plane with an average U-Ow distance of 2.5 Å (Fig.4-2). The finals atomic coordination is shown in Table4-3.

**Talbe4-2: Initial atomic positions of uranyl ion and five water molecules.**

| Atom | x(Å) | y(Å) | z(Å) | Atom | x(Å) | y(Å) | z(Å) |
|---|---|---|---|---|---|---|---|
| U | 0 | 0 | 0 | $O_W$ | 6.66 | 2.64 | 3.17 |
| O | 0 | 0 | 1.76 | $H_W$ | 6.88 | 2.08 | 2.37 |
| O | 0 | 0 | -1.76 | $H_W$ | 7.09 | 2.25 | 3.98 |
| $O_W$ | -3.72 | 0.28 | -0.53 | $O_W$ | -0.36 | 2.9 | 3.69 |
| $H_W$ | -3.12 | 0.82 | 0.05 | $H_W$ | -1.17 | 3.38 | 3.35 |
| $H_W$ | -3.83 | 0.75 | -1.41 | $H_W$ | -0.53 | 1.91 | 3.66 |
| $O_W$ | 0.85 | 4.98 | -1.5 | $O_W$ | 0.73 | -5.81 | 3.47 |
| $H_W$ | 1.69 | 5.53 | -1.53 | $H_W$ | 0.89 | -5.49 | 2.53 |
| $H_W$ | 0.06 | 5.56 | -1.73 | $H_W$ | -0.03 | -6.44 | 3.48 |

**Talbe4-3: Final atomic positions of uranyl ion and five water molecules.**

| Atom | x(Å) | y(Å) | z(Å) | Atom | x(Å) | y(Å) | z(Å) |
|---|---|---|---|---|---|---|---|
| U | 0.20 | 0.24 | 0.41 | $O_W$ | 0.12 | 2.45 | 1.64 |
| O | 0.06 | 1.11 | -1.20 | $H_W$ | -0.40 | 3.24 | 1.33 |
| O | 0.38 | -0.60 | 2.03 | $H_W$ | 0.63 | 2.69 | 2.47 |
| $O_W$ | 1.82 | -1.45 | -0.66 | $O_W$ | 2.58 | 1.19 | 0.47 |
| $H_W$ | 2.28 | -2.19 | -0.18 | $H_W$ | 3.42 | 0.77 | 0.80 |
| $H_W$ | 2.11 | -1.43 | -1.62 | $H_W$ | 2.77 | 2.12 | 0.14 |
| $O_W$ | -2.24 | 0.88 | 0.83 | $O_W$ | -1.24 | -1.71 | -0.29 |
| $H_W$ | -2.92 | 1.18 | 0.17 | $H_W$ | -2.14 | -1.94 | 0.07 |
| $H_W$ | -2.61 | 0.95 | 1.75 | $H_W$ | -0.98 | -2.36 | -1.00 |

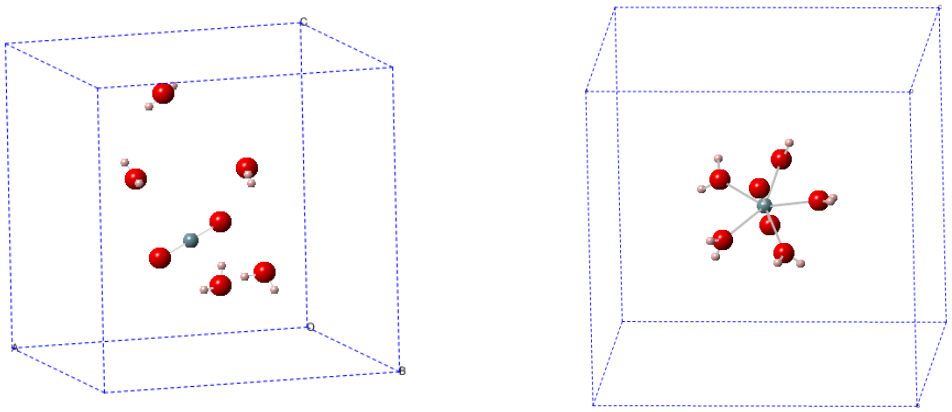

(a) (b)

**Fig.4–2: MD simulation on the $(UO_2)^{2+}$ with five SPC water molecules :( a) initial positions of simulation system; (b) snapshot after MD simulations.**

We have performed some simulations for a single $(UO_2)^{2+}$ ion with more than five water molecules. We have found that the uranyl ion remains always with 5-fold coordination shell.

### *4.3.3 CLAYFF force field parameters*

We have presented the CLAYFF force field in section 3.13. The total energy of this model is expected to have contributions from the long ranged Electrostatic interactions, the short range pair-body (van der Waals) interactions and the bond interaction, which include the chemical bond stretch and valence angle bend terms(equation 3.1). The bond stretch energy of the hydroxyl groups like O-H bonds in this work is described by the third term of equation 3.1, where $k_1$ is a force constant and $r_o$ represents the equilibrium bond length. The three-body energy can be described by the last term where $k_2$ is a force constant. $\theta_{ijk}$ represents the bond angle and $\theta_o$ is the equilibrium bond angle.

In water molecules and between water molecules, the van de Waals interaction occurs only between oxygen atoms. In the kaolinite rigid-body, we ignore the angle bending term but the bond stretch interaction occurs in the surface of hydroxyl groups and in the uranyl U-O bond. For the total system, we ignore all the van der Waals interactions between H atoms and other atoms. Uranyl-clay

interactions include van der Waals term between U atoms and all atoms in kaolinite. All kaolinite potential parameters are introduced by Cygan et al. [61], and which are listed in Table 4-4.

In the surface hydroxyl groups, the hydroxyl oxygen charges is -0.95e and the hydroxyl hydrogen charge is 0.425e. However, in the defects sites, in order to balance the charge of uranyl, we have changed the hydroxyl oxygen charge to -2.00e and the hydroxyl hydrogen charge to +1e. By this method, when deprotonated a surface O-H bond in the defect sites, we can obtain -1e charge. When two O-H bonds are deprotonated in the defect sites, neutral pH is achieved.

To model neutral structure of uranyl-kaolinite, and in order to have more models of uranyl adsorbed on Al(o) surface, we have to invoke two silanol defects at the opposite Si(t) side of the slab model which may be deprotonated when necessary for charge compensation [62]. Such defects may be constructed as introduced by Alena et al. [52]: First, an inner O-Si bond is broken and the oxygen center is artificially saturated by hydrogen, to form an "inner" hydroxyl group. The Si centre is moved outward to the surface and saturated by an OH group, which after deprotonation forms a silanolate moiety (Fig.4-3).

**Talbe4-4: Potential parameters for uranyl ion, kaolinite and SPC water molecules.**

| **Atom type** | **symbol** | **charge (e)** | **Do(kcal/mol)** | **Ro(Å)** |
|---|---|---|---|---|
| Water hydrogen | HW | 0.41000 | 0 | 0 |
| Water oxygen | OW | -0.8200 | 0.1554 | 3.5532 |
| Hydroxyl hydrogen | H | 0.42500 | 0 | 0 |
| Hydroxyl oxygen | $O1$ | -0.95000 | 0.1554 | 3.5532 |
| Bridging oxygen | O2 | -1.05000 | 0.1554 | 3.5532 |
| Tetrahedral silicon | Si | 2.10000 | $1.8405\times10^{-6}$ | 3.7064 |
| Octahedral aluminum | Al | 1.57500 | $1.3298\times10^{-6}$ | 4.7943 |
| Uranium | U | 2.50000 | 0.3733 | 3.1782 |
| Uranyl oxygen | O | -0.25000 | 0.1554 | 3.5532 |
| **Bond** | | **$k_1$(kcal/mol Å$^2$)** | **$r_o$(Å)** | |
| U-O | | 500.00 | 1.80 | |
| O1-H | | 554.13 | 1.00 | |
| **Angle** | | **Θo (deg)** | **$k_2$(kcal/mol Å$^2$)** | |
| O-U-O | | 180.00 | 300.00 | |
| Hw-Ow-Hw | | 109.47 | 47.7696 | |

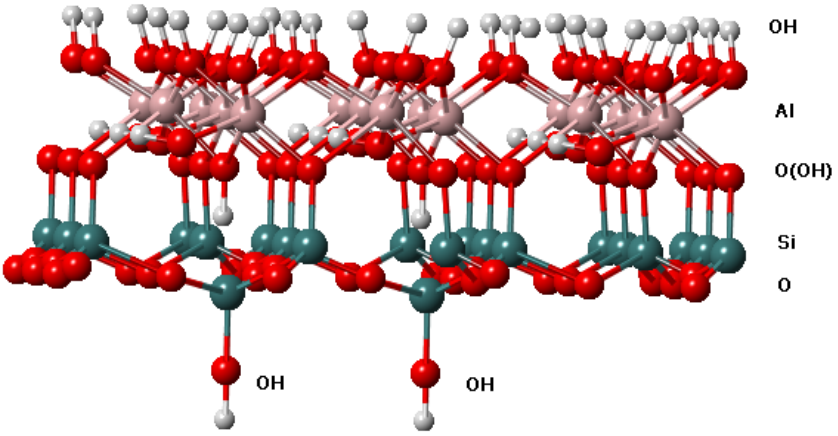


**Fig. 4–3: Side view of Kaolinite structure with two silanol defects in Si(o) surface. These silanol defects can be deprotonated to form a charged silanolate moiety.**

### *4.3.4 Preparation of inner-sphere and outer-sphere complexes models*

All our simulations were performed by the DLPOLY program [63], the ensembles implemented are the constant NVE and NVT [64, 65]. We impose periodic boundary conditions on the xy dimensions to produce xy repeating macroscopic system but no repeat in z direction so that we can focus on adsorption in kaolinite surface instead of in the kaolinite interlayer. The Ewald sum technique was used for electrostatic interactions. For Van der Waals interactions, a real-space cutoff of 8.5Å was imposed. Simulation temperature and pressure were 300K and 0.01bar respectively. We used a 0.0005 ps timestep for all MD simulations. For each model, we carried out 150 ps of simulation time to calculate adsorption equilibrium constants and standard state free energies for NVE ensemble. The final configuration obtained at the NVE simulation was used as the initial configuration for the NVT simulation following 100 ps of simulation time.

Adsorption between metals and clay minerals can occur via two mechanisms: outer-sphere adsorption and inner-sphere adsorption [66]. For the outer-sphere complex, the dissolute uranyl is

assumed to remain intact, the interaction between uranyl and kaolinite is mainly electrostatic, the adsorbed distance between U and surface oxygen is long. The metal is more like a free hydrated ion. But for inner-sphere complexes, chemical bonds to the surface $O^{2-}$ or $OH^{1-}$ groups are formed; the uranyl and surface oxygen distance are relatively smaller. The inner-sphere complexations are considered as leading to strong chemical bound.

In the present study, we performed various adsorption complexes depending on the degree of deprotonation of Al(o) surface hydroxyl group and the degree of deprotonation of silanol group in the defect site. It includes two general types of adsorption sites: (i ) two $Os^-$ center by two deprotonated OH groups or (ii ) one $Os^-$ center and one OH group. For inner-sphere complexation, only bidentate uranyl adsorptions are studied, which include two types: first for neighboring O centers connected to the same Al atom and second for pairs of O centers attached to neighboring Al centers. In our models, the O-O distance in short-bridge sites (AlOO) is 275 pm and in long-bridge sites (AlO-AlO) is up to 359 pm (Fig4-4).

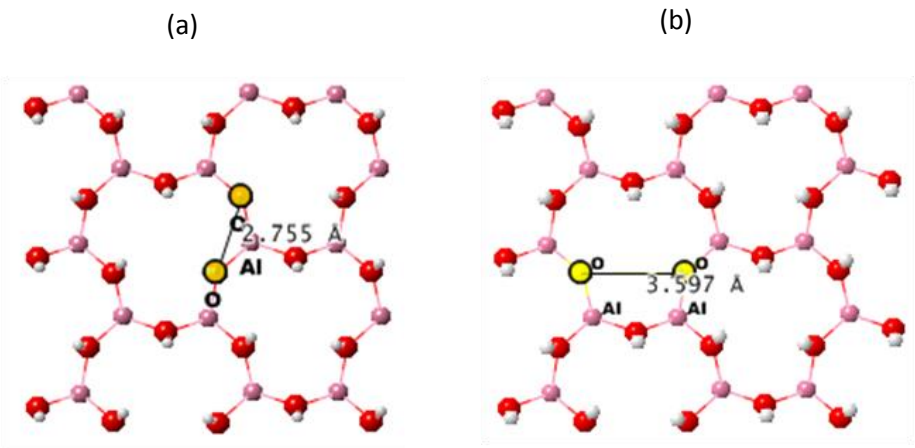


**Fig.4–4: Top view of the Al(o) (001) surface of kaolinite. (a) The two O centers connect to the same Al and O-O distance shows 2.755 Å; (b) the two O centers connect to neighboring Al centers and O-O distance achieving 3.59 Å**

We modeled 4 inner-sphere complexes. To avoid models with a charged unit cell, we created deprotonated $SiO^-$ defects in Si(O) side depending on the number of deprotonated surface OH groups involved in the Al(O) surface: a) two deprotonation in Al(O) surface, where the two deprotonated $O^-$ centers connected to the same Al atom, zero deprotonation in SiOH defect (Fig4-5a); b) two

deprotonation in Al(O) surface, where the two deprotonated $O^-$ centers connected to neighboring Al atoms, zero deprotonation in SiOH defect(Fig.4-5b); c) one deprotonation both in Al(O) surface and in SiOH defect (Fig.4-5c), and d) two deprotonated $SiO^-$ defects in Si(O) surface, no deprotonation in Al(O) surface (Fig4-5d). Besides these various inner-sphere complexes, we optimized an outer-sphere complex (Fig4-6). In this model, we did not involve SiOH defect in the Si(O) surface; a neutral system was constructed by replacing solvated uranyl by the corresponding neutral dihydroxide complex[49].

According to the research by Benco et al. [67], there are three distinct OH groups in the gibbsite layer. Another investigation was illustrated by Notker Rösch et al. [49, 52, 68]. They thought that, in the Al(o) surface exhibits two types of hydroxyl groups: two thirds of which are 'upright' OH groups, oriented largely perpendicular to the surface plane, and one-third of 'lying' OH group that are oriented mainly parallel to the surface [56]. However, in the present work, we consider all the OH groups in Al (o) surface identical.

We examined also an outer-sphere complexion on the Al (o) (001) surface. For this complexion, a neutral system was constructed by replacing solvated uranyl by the corresponding neutral dihydroxide complex [49]. No defect was involved in Kaolinite structure, neither deprotonation. We might say that this outer-sphere complex is a neutral complex. Collected results show two very short bonds to OH groups (2.205 Å and 2.282 Å). For aqua ligands, two of three are short bonds with 2.560 Å and 2.526 Å while the third one achieved 3.344 Å. The third U-Ow attract is rather weak that it cannot be considered as an aqua ligand of the first salvation shell. Thus, the coordination number of uranyl is 4 in this model of the outer-sphere complex with an average value U-Oeq = 2.393 Å. If we include the third weak U-Ow attract, we have an average of 2.583 Å. In figure 9, the two OH groups were represented by yellow atoms. One OH group was attracted by Kaolinite surface, and we noted this OH has a OH-Al distance of 2.777Å which is short. Even for inner-sphere complexes, the aqua to Al distance are ~ 3.30 Å which is larger than 2.777 Å. Compared with inner-sphere, the U-Al distance shows a reasonable length of 4.791 Å.

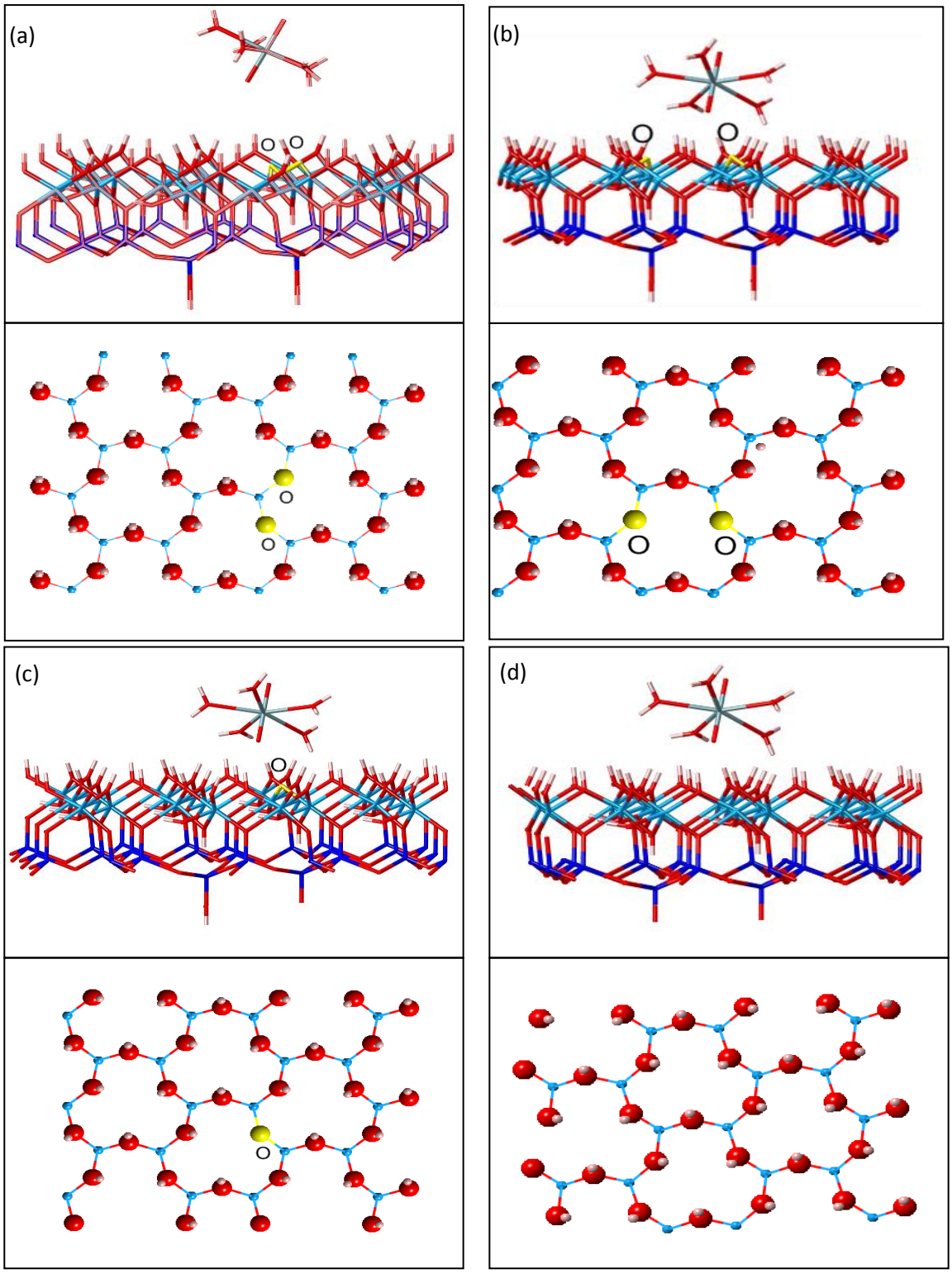


**Fig.4–5: schematic representation of model adsorption inner-sphere complexes on Al(O) (001) surface: a) two deprotonated O- centers in the Al(O) surface and bound to the same Al center, zero deprotonation on SiOH defects; b) two deprotonated O- centers in the Al(O) surface and bound to neighboring Al centers, zero deprotonation on SiOH defects; c) one deprotonation O- both in Al(O) surface and SiOH defects; d) zero deprotonation on Al(O) surface and two deprotonated O- on SiOH defects. The deprotonated O- on Al(O) surface were indicated by yellow sticks. Top view of Al(O) surface are below the side view images.**

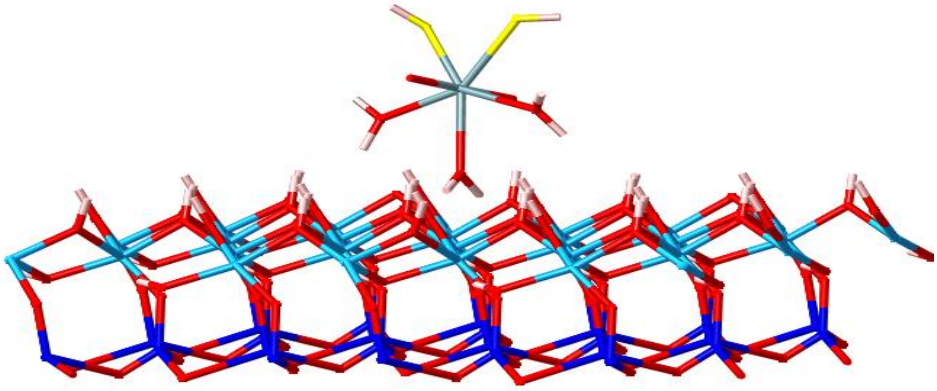

**Fig.4–6: Model adsorption outer-sphere complex of neutral uranyl $UO_2(H_2O)_3(OH)_2$ on Al(o) (001) surface. The yellow atoms indicate oxygen atoms in OH group.**

## 4.4 Results and discussion

### *4.4.1 Uranyl adsorption on Al(O) surface with NVE ensemble*

As mentioned above, four different models of adsorption complexes were explored on both short-bridge sites O(H)-Al-O(H) and long-bridge sites Al-O(H)-Al-O(H) with two defects introduced at the opposite Si(o) surface, silanol or silanolate. All of them are schematically presented in Fig. 4-5, where we compare the four adsorption complexes of uranyl. For complex on doubly deprotonated $O^-$-Al-$O^-$site (Fig. 4-5a) and Al-$O^-$-Al-$O^-$site (Fig. 4-5b), two positive charges of uranyl are neutralized by two negative charges on site $O^-$-Al-$O^-$or Al-$O^-$-Al-$O^-$. For the models shown in Fig.4-5c, one negative charge is involved on site OH-Al-$O^-$ what requires another negative charge defect to be neutralized, and thus, one silanol group was deprotonated. For the model 4-5d, no deprotonation appears in Al(o) surface, so that two deprotonated $SiO^-$ groups are required to achieve charge compensation.

In these four models of uranyl adsorption, uranyl complex fits perfectly with kaolinite. They are similar in geometries. For the original uranyl structure, the average U-$O_t$ distance is ~1.83 Å and the

average U-Ow distance is ~2.539 Å. **C**ompared with optimized results, bond lengths decrease or increase within 2 pm, while the average length of ligand and surface U-O bonds fluctuate within 20 pm. The U-Os distances in complex A are pretty close because of identical negative charge appears for both two deprotonated adsorption $O^-$ sites.

U-O distance in complexes at long-bridge sites Al-O(H)-Al-O(H) are not very different with that at short-bridge sites O(H)-Al-O(H), but the average U-O distance are generally smaller at long-bridge sites, (Table 4-5). In complex B, it exhibits 6 coordination number CN = 6. Three U-surface oxygen bonds appeared with their length which are: 2.330 Å, 2.473 Å and a long contact around 2.944 Å. Because of the appearance of this third contact of U-Os, we might consider that at long-bridge sites, the uranyl is closer to the kaolinite Al(o) surface.

In simulation of complexes A and B, we built two deprotonations at surface OH groups, thus, two negative charges were created, and they give a relative strong attraction to uranyl (two positive charges). Compared with these two complexes, the model C has only one negative charge at OH groups. We notice that the complexe C results in two U-Os bonds, it exhibits a rather short U-Os bond of 2.282 Å to the negative charged $O^-$ center. Another longer bond achieves 2.873 Å, which are much longer than average distance. The longer bond of U and OH center in complexe C can be regarded as rather weak. For model D, two negative charges were brought in opposite Si(O) surface on defects. Charge distance within kaolinite and uranyl exceeds 9.00 Å. Compared with U-Os distance in complex A (2.372 Å and 2.374 Å), U-Os distance in model D is relatively long (2.394 Å and 2.553 Å). We note that U-Al distances at long-bridge sites are longer than at short-bridge sites. It exhibits two U-Al ligands (3.220 Å and 3.524 Å) in model B. This shows again that in complex B, uranyl is more close to kaolinite surface. There is no big difference of U-Al distances between the three models, but the second bond of ~3.80 Å are too long, thus, we could consider only a single bond for U-Al. The optimized geometries of uranyl adsorption inner-sphere complexes in NVE ensemble are shown in Fig.4-7 and the optimized model parameters are presented in Table 4-5.

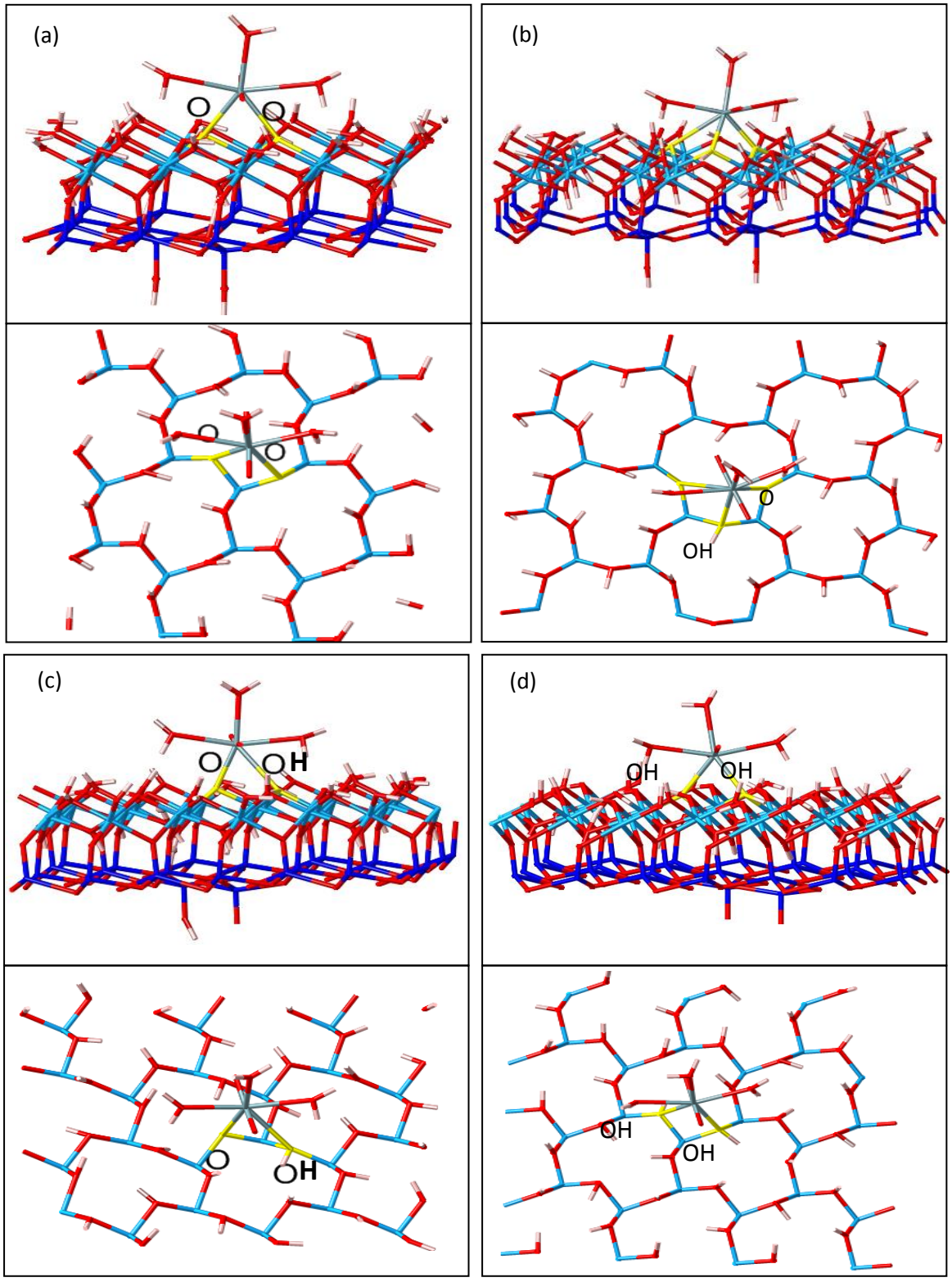


**Fig.4–7: Optimized geometries of uranyl adsorption inner-sphere complexes on Al(O) surface in NVE ensemble.**

**Table 4-5: Four optimized model parameters of uranyl adsorption complex at short-bridge O(H)-Al-O(H) and long-bridge Al- O(H)-Al-O(H) sites with NVE ensemble; N: coordination number; U-$O_t$: Uranyl bond length; U-Ow: bond length to aqua ligands; U-$O_s$: bond length to surface oxygen centers; U-$O_{eq}$: average bond length of I to his coordination; U-Al: bond length to Al atoms.**

| Model | N | U-$O_t$(Å) | U-$O_w$(Å) | U-$O_s$(Å) | U-$O_{eq}$(Å) | U-Al(Å) |
|---|---|---|---|---|---|---|
| $[UO_2(H_2O)_5]^{2+}$ | 5 | 1.831, 1.822 | 2.575, 2.533, 2.492, 2.540, 2.556 | | 2.539 | |
| A | 5 | 1.823, 1.812 | 2.496, 2.521, 2.624 | 2.372, 2.374 | 2.477 | 2.975 |
| B | 5(6) | 1.840,1.868 | 2.500, 2.638, 2.707 | 2.330, 2.473, (2.944) | 2.529 (2.598) | 3.220, 3.524 |
| C | 5 | 1.849, 1.805 | 2.582, 2.425, 2.624 | 2.282, 2.873 | 2.557 | 3.117 |
| D | 5 | 1.832, 1.795 | 2.542, 2.485, 2.501 | 2.394, 2.553 | 2.495 | 3.154 |

### *4.4.2 Outer-sphere complex in NVE ensemble*

We examine here an outer-sphere complexion on the Al (o) (001) surface. For this complexion, a neutral system was constructed by replacing solvated uranyl by the corresponding neutral di-hydroxide complex $UO_2(H_2O)_3(OH)_2$ [49]. Neither defect was involved in Kaolinite structure, no deprotonation. We may say that this outer-sphere complex is a neutral complex (Fig.4-6). Collected results show two very short bonds to OH groups (2.205 Å and 2.282 Å). For aqua ligands, two of three are short bonds with 2.560 Å and 2.526 Å while the third one achieved 3.344 Å. The third U-Ow bond is rather weak, then it cannot be considered as an aqua ligand of the first salvation shell. Thus, the coordination number of uranyl is 4 in this model of the outer-sphere complex with an average value U-Oeq = 2.393 Å. If we include the third weak U-Ow bond, we obtain an average of 2.583 Å. In Fig. 4-8, the two OH groups were represented by yellow atoms. One OH group was attracted by Kaolinite surface, and we notice that this OH has a OH-Al distance of 2.777Å which is short. Even for inner-sphere complexes, the aqua to Al distance are ~ 3.30 Å which is larger than 2.777 Å. Compared with inner-sphere, the U-Al distance shows a reasonable length of 4.791 Å. The outer sphere complexes keep away from the kaolinite surface, because there is no big electrostatic attraction between the two neuter structures. Atomic density profiles of $UO_2^{2+}$ as a function of z are shown in Fig. 4-8. For the 4 inner sphere complexes,

$UO_2^{2+}$ are most likely to be found at 2.42-3.10 Å in z direction, and 4.35-5.23 Å for outer-sphere complexes.

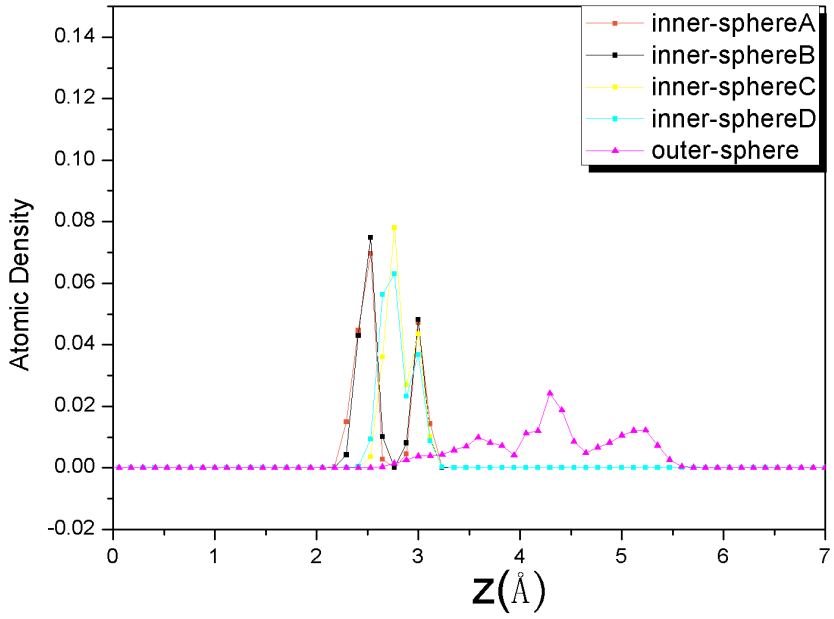


**Fig. 4–8: Atomic density profiles for uranyl ion in inner-sphere complex and outer-sphere complex with NVE ensemble.**

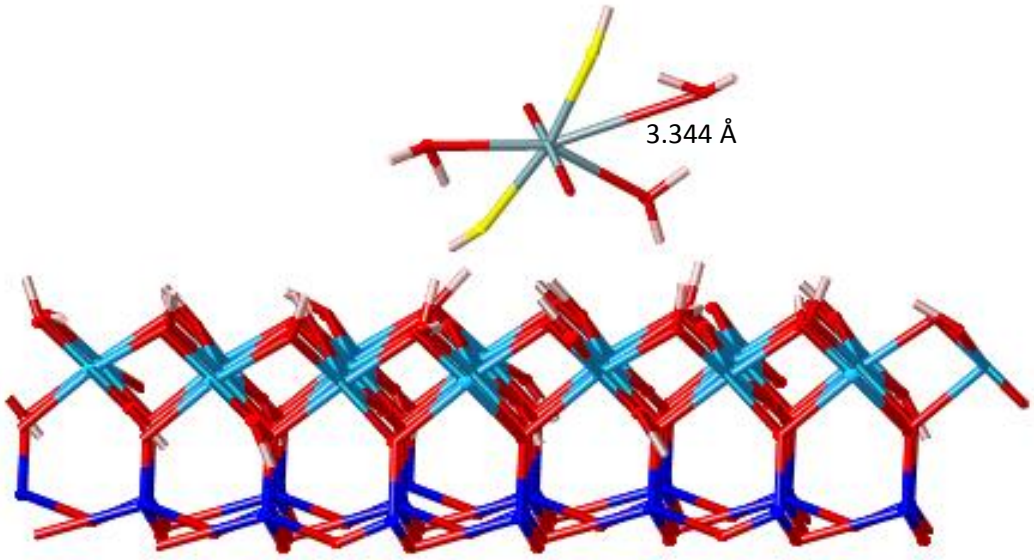


**Fig. 4–9: Optimized geometries of neutral outer-sphere complex of $UO_2(H_2O)_3(OH)_2$ on kaolinite surface. Yellow atoms represent hydroxyls oxygen.**

### 4.4.3 Adsorption results from NVT ensemble

We repeated the calculation for all models mentioned above with NVT ensemble. In this ensemble, molecules numbers, volume and temperature are conserved. The results for these complexes are shown in Table 4-6. As we expected, NVT and NVE results are similar. In short-bridge sites O(H)-Al-O(H), attracted to oxygen surface in complex A are relatively strong (2.296 Å and 2.386 Å). At long-bridge sites AlO(H)-AlO(H), the complex B exhibits coordination number CN = 6: there are three links to surface oxygen Os, include a third long ligand U-Os of 2.939Å and two similar shorter U-Os bonds. U-Oeq = 2.569 Å, which is 29 pm smaller than 2.598 Å in the same model with NVE ensemble. The third bond of 2.939 Å is rather long that cannot be considered as first coordination shell of uranyl. If we exclude it from the average equatorial distance, then we have CN = 5 and U-Oeq = 2.495 Å. In complexes C, it exhibits two bonds: a short one and a long one. The short bond of 2.246 Å bound to deprotonated $O^-$ centers because of the charge attraction. The long one of 2.796 Å is relatively weak. In model D, two links to surface oxygen are weaker than that in complex A. U-Al distance seems longer at long-bridge sites in complex B. The Fig4-10 shows us the atomic density profiles of $UO_2^{2+}$ for inner and outer complexes with NVT ensemble.

**Table 4-6: Optimized structure parameters of all uranyl adsorption complexes with NVT ensemble.**

| Model | N | U-Ot(Å) | U-Ow(Å) | U-Os(Å) | U-Oeq(Å) | U-Al(Å) |
|---|---|---|---|---|---|---|
| **Inner-sphere** | | | | | | |
| A | 5 | 1.802, 1.850 | 2.492, 2.573, 2.514 | 2.296, 2.386 | 2.452 | 2.974 |
| B | 5 (6) | 1.768, 1.802 | 2.538, 2.502, 2.561 | 2.414, 2.461, (2.939) | 2.495(2.569) | 3.263, 3.513 |
| C | 5 | 1.826, 1.830 | 2.569, 2.434, 2.497 | 2.246, 2.796 | 2.508 | 3.052 |
| D | 5 | 1.842, 1.863 | 2.482, 2.571, 2.611 | 2.403, 2.592 | 2.531 | 3.046 |
| **Outer-sphere** | **N** | **U-Ot**(Å) | **U-Ow**(Å) | **U-Oh**(Å) | **U-Oeq**(Å) | **U-Al**(Å) |
| | 4(5) | 1.824, 1.852 | 2.484,2.649, (3.746) | 2.212, 2.280, | 2.406(2.674) | 6.4000 |

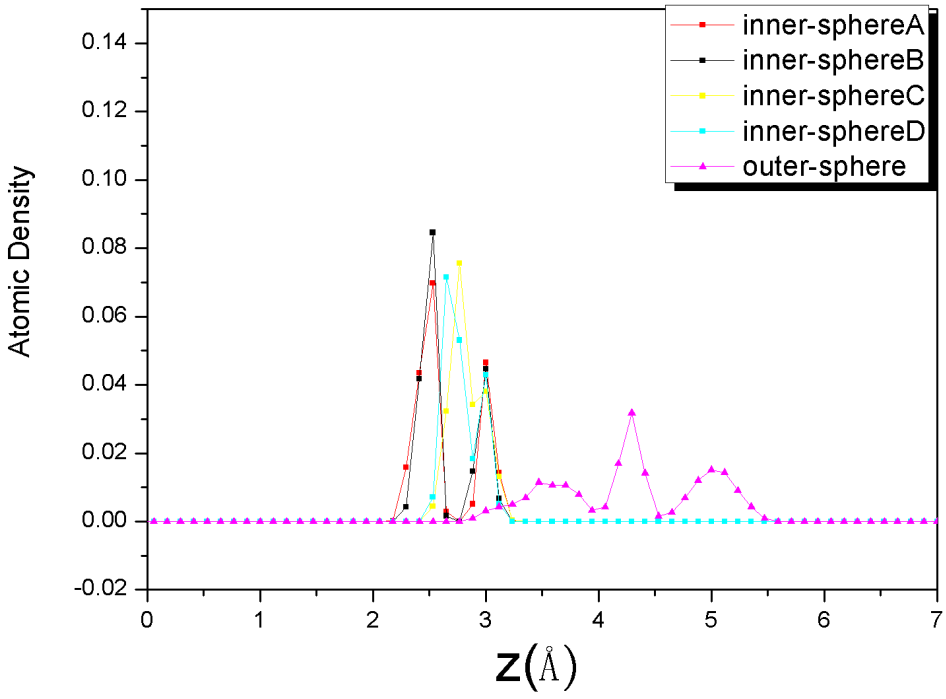


**Fig. 4–10: Atomic density profile for Uranyl ions near the kaolinte surface of inner-sphere and outer-sphere complex in NVT ensemble.**

### *4.4.4 Conclusions and Comparison with experiment and other theoretical studies*

We have presented in this work a computer simulation study of complexes of uranyl at kaolinite Al(o) surface. Based on MD simulations, we used CLAYFF force field to model kaolinite and uranyl interactions. The kaolinite surfaces were modeled using a single layer of kaolinite with 2D periodic boundary conditions. We considered inner-sphere and out-sphere complexes with both NVE and NVT ensembles. There were no big differences between the two studies. The geometry of the inner-sphere complexes of uranyl at kaolinite surface is mainly determined by the degree of charged $O^-$ groups and the distance of charged $O^-$ groups. The bond to deprotonated $O^-$ center is always short, ligand attract is strong: in NVE ensemble, bond lengths to $O^-$ centers is 2.282 Å single deprotonated models. In NVT ensemble, the value of bond lengths to O- centers for single deprotonated complexes is 2.246Å. For the doubly

deprotonated $O^-$-Al-$O^-$ models (at short-bridge sites), bond lengths to $O^-$ are 2.372 Å, 2.374 Å with NVE ensemble, and are 2.296 Å, 2.386 Å with NVT ensemble. These bond lengths are relatively short. At long-bridge sites, in doubly deprotonated $O^-$-Al-$O^-$ model, it exhibits three U-Os attracts two shorter and one longer, with 6-fold coordination, which were considered. However, at short-bridge sites, for the same doubly deprotonated model, we found only two U-Os attracts, and 5-fold coordination number.

Next we will compare our results with density functional theory studies and experimental EXAFS measurements concerning the average structure parameters of the adsorption complexes of uranyl on the surface of Kaolinte[52, 53, 69-71]. We consider only the comparison of our structural parameters of various adsorption complexes optimized in NVT ensemble (Table4-6) with DFT studies[52, 53, 69-71] and experimental EXAFS studies[52, 53, 69-71] as shown in Table 4-7. Our uranyl bonds U-$O_t$ are somewhat longer (1.80-1.86 Å) when compared with experimental values (1.77 and 1.79 Å), but some are shorter than density functional results (1.83-1.87 Å) for the inner-sphere complexes. The U-O distance U-$O_{eq}$ of 2.454-2.533 Å agrees well with density functional results, 2.45-2.54 Å, but longer than experiment of 2.34-2.41 Å as shown in Table 4-7. We notice that the coordination number is not valued for the experimental EXAFS studies. CN=5 was always, but according to our models and density functional models, CN=6 may occurs in adsorption complexes at long-bridge sites where uranyl exhibits a third contact to the surface. If we consider only the first coordination shell of calculated U-Al distances in our studies, 2.974-3.263 Å, we find good agreement with experiment (3.10-3.30 Å and 3026-3.26 Å). For complexes in doubly deprotonated sites at long-bridge Al-O—Al-O- sites, the coordination number and average equatorial U-O distance U-$O_{eq}$ are in good agreement with density functional results of 2.569/2.495 Å compared to 2.54/2.49 Å obtained from experiment. Concerning adsorption complexes, they show the same geometric performances of adsorption of uranyl on the (001) kaolinite surface with density functional and experimental studies. According to the comparisons cited above between our molecular dynamics study within NVE ensemble (Table 4-5) and other studies (Table 4-7) realized by denstity functional method and EXAFS experimental method, we can say that our results show good agreement with both experimental and theoretical results.

**Table 4-7: DFT calculations and EXAFS measurements of uranyl adsorption complexes at the (001) Al(O) surface.**

| Model | U-Ot(Å) | U-Oeq(Å) | U-Al(Å) | Referenc |
|---|---|---|---|---|
| Experimental studies | | | | |
| exp, CN=5 | 1.79 | 2.37~2.41 | 3.10~3.30 | [53] |
| Exp, CN=5 | 1.77 | 2.34 | 3.06/3.26 | [71] |
| Theoretical studies | | | | |
| $O^-$-Al-$O^-$, CN=5 | 1.87 | 2.45 | 3.11 | [69] |
| $O^-$-Al-OH, CN=5 | 1.86 | 2.51 | 3.32 | [69] |
| OH-Al-OH, CN=5 | 1.83 | 2.46 | 3.46 | [52] |
| Al-$O^-$-Al-$O^-$, CN=6 | 1.87 | 2.54/2.49 | 3.30/3.40 | [69] |
| Outer-sphere, CN=4(5) | 1.81 | 2.47/2.64 | | [52] |
| Our DM studies with NVE ensemble | | | | |
| $O^-$-Al-$O^-$, CN=5 | 1.826 | 2.452 | 2.974 | |
| $O^-$-Al-OH, CN=5 | 1.828 | 2.508 | 3.052 | |
| OH-Al- $O^-$, CN=5 | 1.810 | 2.533 | 3.078 | |
| OH-Al-OH, CN=5 | 1.853 | 2.531 | 3.046 | |
| Al-$O^-$-Al-$O^-$ , CN=6 | 1.785 | 2.495/2.569 | 3.263, 3.513 | |
| Outer-sphere, CN=4(5) | 1.838 | 2.406/2.674 | | |

# Chapter 5. Behind adhesion of uranyl onto montmorillonite surface: A molecular dynamics study

## 5.1 Abstract

We have performed molecular dynamics simulations to investigate the adsorption of radionuclide elements species onto substituted Montmorillonite (001) surface in the presence of different counterions. The structure and the dynamics of uranyl ion as well as its aquo, chloride ion, and carbonate complexes are analyzed. In addition, we have studied the surface energy between layered Montmorillonite sheets and the work of adhesion between radionuclide and charged Montmorillonite. The clay model used here is a Wyoming-type Montmorillonite with 0.75e negative charge per unit cell resulting from substitutions in Octahedral and Tetrahedral sheets. The system model was constructed based on CLAYFF force field potential model. To evaluate the thermodynamic work of adhesion, each surface and clay layer regions are converted to a thin film model. One and two species of radionuclide elements ($UO_2^{2+}$)$(H_2O)_5$,$UO_2CO_3(H_2O)_5$, and $UO_2Cl_2(H_2O)_5$) were deposited near the clay surface in a pseudo-two-dimensional periodic cell. Analysis shows that the uranyl ion structure is preserved with two axial oxygen atoms detected at 1.8Å. Radial distribution functions results indicate that average U-$O_w$ distances are 2.45-2.61 Å, and 2.29-2.40 Å for U-$O_c$ distance. Average U-Cl distances are 2.78-3.08 Å, which is relatively larger than that of Uranium atom-Oxygen atom because of electrostatic factors.

## 5.2 Introduction

In recent years, the study in actinide adsorption on clay mineral has greatly increased due to an ongoing concern in environmental research. Their interaction with clay mineral surface plays an important role to govern the migration of actinide in the environment. Knowledge of a description of how actinides interact with clay mineral surface is important for assessing the risk caused by the nuclear waste repositories[1]. Uranium is the predominant heavy metal content of the final waste in the nuclear fuel cycle (>95% $UO_2$). Also, uranium is a major contaminant in the soil, subsurface and groundwater as a result of human activity. Under standard environmental conditions, the most stable chemical form of U(VI) is the uranyl ion $UO_2^{2+}$, which is potentially very mobile and readily complexates with organic and inorganic matter. To assess the possibility of forming an adsorption complex of uranyl onto clay mineral, one has to analyze the energy change which concerned the adhesion strength between radionuclide and clay mineral. The thermodynamic concept quantifying the adsorption is the work of adhesion. However, only a few work of adsorption energy or interaction energy have been realized about clay [2-5]. In this work, the interaction between MMT sheets and the adsorption energy between the radionuclide and MMT surface will be discussed.

Numerous experimental studies of uranyl adsorption on various clay minerals surfaces have been published, e.g. montmorillonite, illite, and kaolinite [6-14]. X-ray adsorption fine structure (XAFS) spectroscopy has been used to study the structure details of surface complexes formed between uranyl and mineral surfaces [15-19]. Recent first-principles density functional theory (DFT) calculations show us a lot of possible inner- and outer-sphere adsorption complexes at kaolinite surface[2, 3]. Although various experimental studies provide some measurement of attenuation capacity of clay minerals for uranyl [15, 20-23], there is still much to be studied on the atomic scale about the structures details of uranyl adsorption onto mineral surfaces.

The remarkable development of molecular computer simulations is very helpful in demonstrating a chemical evolution on the structure and behavior of clay minerals on the atomic level. In this paper, Molecular Dynamics (MD) simulations methods [30]were employed to study the microscopic aspects of

the interaction of uranyl with the Montmorillonite surface, followed by the methods used to obtain the interaction energy and work of adhesion.

## 5.3 System parameters and MD simulation

### *5.3.1 Structure of montmorillonite*

Montmorillonite is a 2:1 clay and a member of the smectite family, which has a strong adsorption and ion exchange capacity. The clay model used in our simulations is a Wyoming-type MMT[30] with the unit cell formula:

$M_{0.75}(Si_{7.75}Al_{0.25})(Al_{3.5}Mg_{0.5})O_{20}(OH)_4$ or $N_{0.325}(Si_{7.75}Al_{3.25})(Al_{3.5}Mg_{0.5})O_{20}(OH)_4$

where M represents a monovalent cation. In the present work $Na^+$, $K^+$, $Cs^+$ are considered. N represents a double valent cation such as $Ba^{2+}$, $Pb^{2+}$, $Ca^{2+}$, $Zn^{2+}$, etc. The coordinates and partial charges of atoms of a unit cell MMT crystal structure is presented in Table5-1, where we don't consider the substitutions.

**Table 5-1: Atomic positions in the unit cell of a dioctahedral clay mineral layer[72].**

| Atom | x(Å) | y(Å) | z(Å) | q(e) | Atom | x(Å) | y(Å) | z(Å) | q(e) |
|---|---|---|---|---|---|---|---|---|---|
| **O** | 2,64 | .0. | 3,28 | -0,8 | **Al** | 7,04 | 6,09 | 0 | 3 |
| **O** | 1,32 | 2,28 | 3,28 | -0,8 | **Al** | 7,04 | 3,05 | 0 | 3 |
| **O** | 3,96 | 2,28 | 3,28 | -0,8 | **O** | 0,88 | 9,14 | -3,28 | -0,8 |
| **O(H)** | 0 | 0 | 1,06 | -1,718 | **O** | 2,2 | 6,86 | -3,28 | -0,8 |
| **H** | 0,8815 | 0 | 1,434 | 0,7175 | **O** | -0,44 | 6,86 | -3,28 | -0,8 |
| **Si** | 2,64 | 1,52 | 2,73 | 1,2 | **O(H)** | 3,52 | 9,14 | -1,06 | -1,7175 |
| **Si** | 0 | 3,05 | 2,73 | 1,2 | **H** | 2,6385 | 9,14 | -1,434 | 0,7175 |
| **O** | 2,64 | 1,52 | 1,06 | -1 | **Si** | 0,88 | 7,62 | -2,73 | 1,2 |
| **O** | 0 | 3,05 | 1,06 | -1 | **Si** | 3,52 | 6,09 | -2,73 | 1,2 |
| **Al** | 4,4 | 1,52 | 0 | 3 | **O** | 0,88 | 7,62 | -1,06 | -1 |
| **Al** | 4,4 | -1,52 | 0 | 3 | **O** | 3,52 | 6,09 | -1,06 | -1 |
| **O** | 0 | 4,57 | 3,28 | -0,8 | **O** | 3,52 | 4,57 | -3,28 | -0,8 |
| **O** | 3,96 | 6,85 | 3,28 | -0,8 | **O** | -0,44 | 2,29 | -3,28 | -0,8 |
| **O** | 1,32 | 6,85 | 3,28 | -0,8 | **O** | 2,2 | 2,29 | -3,28 | -0,8 |
| **O(H)** | 2,64 | 4,57 | 1,06 | -1,718 | **O(H)** | 0,88 | 4,57 | -1,06 | -1,7175 |
| **H** | 3,5215 | 4,57 | 1,434 | 0,7175 | **H** | -0,0015 | 4,57 | -1,434 | 0,7175 |
| **Si** | 0 | 6,09 | 2,73 | 1,2 | **Si** | 3,52 | 3,05 | -2,73 | 1,2 |
| **Si** | 2,64 | 7,62 | 2,73 | 1,2 | **Si** | 0,88 | 1,52 | -2,73 | 1,2 |
| **O** | 0 | 6,09 | 1,06 | -1 | **O** | 3,52 | 3,05 | -1,06 | -1 |
| **O** | 2,64 | 7,62 | 1,06 | -1 | **O** | 0,88 | 1,52 | -1,06 | -1 |

However, we always need considering the isomorphic substitutions in the tetrahedral and octahedral sheets which result negative charges. In our MMT formula, the first and second bracketed terms refer to ions in the tetrahedral and octahedral layers. One out of eight Al atoms in octahedral sheet is replaced by Mg atom, the charge is reduced from +3e to +2e; likewise, one out of 32 Si atoms in tetrahedral sheet is replaced by an Al atom, which results in a reduction in the charge on the site from +1.2e to +0.2e. The positions of the substitutions in octahedral and tetrahedral sheets in our montmorillonite model are shown in Table 5-2. The model system was expanded into a super cell of 21 Å×36 Å in the x and y dimension, which contains 16 MMT unit cell (4×4 repeats in a and b dimension). The 4×4 unit cells of clay layer contain 640 atoms: 124 Si and 4 Al in the tetrahedral sheets, 56 Al and 8 Mg in the octahedral sheets, 384 O and 64 H centers; while 12e negative charge are contained in the clay layer. Different counterions were added to the surface and interlayer region to balance negative charge in the clay layers, a typical Na-worming type MMT structure is shown in Fig.5-1, with $Na_{12}(Si_{124}Al_4)(Al_{56}Mg_8)O_{320}(OH)_{64}$ the formula for our 4×4 super cell model.

**Table5-2: Positions of substitutions in octahedral and tetrahedral sheets of montmorillonite.**

| Atom | x(Å) | y(Å) | z(Å) | Atom | x(Å) | y(Å) | z(Å) |
|---|---|---|---|---|---|---|---|
| Substitution in octahedral sheet | | | | | | | |
| Mg | 4.40 | -1.52 | 0.00 | Mg | 4.4 | 16.76 | 0.00 |
| Mg | 7.04 | 6.09 | 0.00 | Mg | 9.68 | -7.62 | 0.00 |
| Mg | -6.16 | 1.52 | 0.00 | Mg | -6.16 | 10.66 | 0.00 |
| Mg | -3.52 | -15.23 | 0.00 | Mg | 1.76 | -3.05 | 0.00 |
| Substitution in tetrahedral sheet | | | | | | | |
| Al | 2.64 | -7.62 | 2.73 | Al | 5.28 | 6.09 | 2.73 |
| Al | -9.68 | 16.76 | -2.73 | Al | -7.04 | -3.05 | -2.73 |

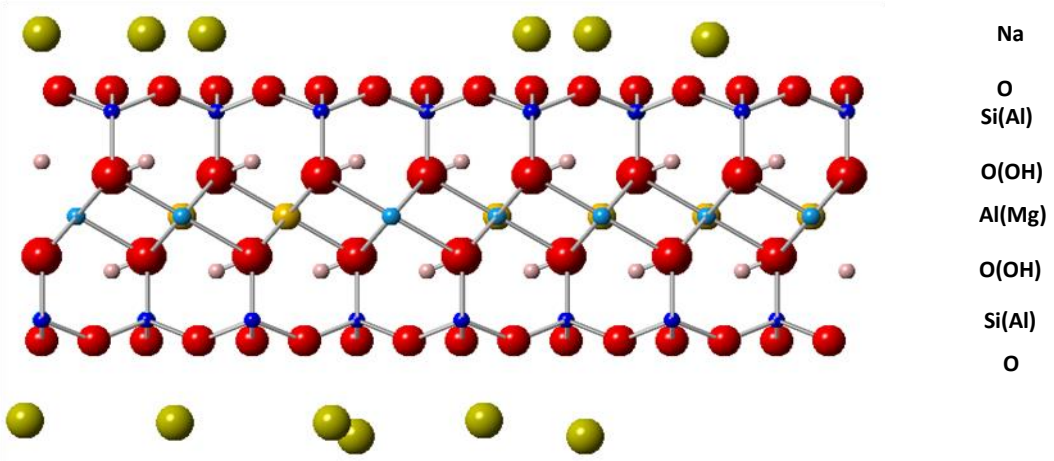


**Fig.5–1: Structure of 4×4 super cell Na-wyoming montmorillonite.**

## *5.3.2 Structure of radionuclide elements*

In this present work, we involved three radionuclide elements. Hydrated uranyl ions $(UO_2^{2+})(H_2O)_5$, uranyl carbonate $(UO_2^{2+})(H_2O)_5(CO_3)$ , and uranyl chlorite $(UO_2^{2+})(H_2O)_5Cl_2$ (Fig.5-2). They are considered as the radionuclide element structures in the surface region of montmorillonite. In order to understand the chemical reactions between the radionuclide elements and MMT surface, we have displaced these radionuclides onto the MMT surface respectively. For charged $(UO_2^{2+})(H_2O)_5$ ions, one species can replace a valent or two monovalent counterions:

$$[(UO_2^{2+})(H_20)_5]_n\, M_{6-n}(Si_{124}Al_4)(Al_{56}Mg_8)O_{320}(OH)_{64} \text{ or}$$

$$[(UO_2^{2+})(H_2O)_5]_n\, N_{12-2n}(Si_{124}Al_4)(Al_{56}Mg_8)O_{320}(OH)_{64}$$

where M and N represent monovalent cations and valent cations, respectively. The index n can be one and two in this work. In the case of n=1, one valent counterion was replaced by the $(UO_2^{2+})(H_2O)_5$. The rest five valent counterions and one $(UO_2^{2+})(H_2O)_5$ are found in the surface region to balance the charge of the clay layer. Two monovalent counterions were replaced to make one $(UO_2^{2+})(H_2O)_5$ and ten monovalent counterions remain. For the case of n=2, four valent or eight monovalent counterions and two $(UO_2^{2+})(H_2O)_5$ will be found in the surface region to make a neuteral system. For neuter uranyl carbonate and uranyl chlorite, we don't need to change the counterions numbers when displacing them onto the MMT surface. The initial coordinates for these radionuclide are shown is Table5-3.

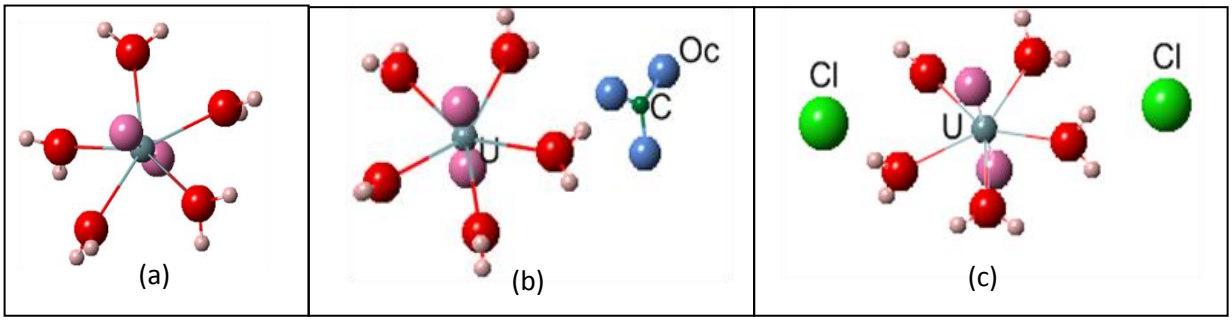


**Fig.5–2: Structure of three radionuclide elements: (a) hydrated uranyl ions $(UO_2^{2+})(H_20)_5$; (b) hydrated uranyl carbonate $(UO_2)(H_20)_5(CO_3)$; (c) hydrated uranyl chlorite $(UO_2)(H_20)_5Cl_2$.**

**Table 5-3: Initial coordinates for radionuclide elements.**

| Atom | x(Å) | y(Å) | z(Å) | Atom | x(Å) | y(Å) | z(Å) |
|---|---|---|---|---|---|---|---|
| U | 4,2 | 10,25 | 6,91 | OW | 6,24 | 11,13 | 5,75 |
| O | 3,15 | 10,57 | 5,44 | HW | 6,45 | 12,09 | 5,57 |
| O | 5,21 | 9,92 | 8,4 | HW | 6,96 | 10,55 | 5,37 |
| OW | 2,91 | 8,13 | 7,35 | OW | 5,41 | 8,32 | 5,65 |
| HW | 1,98 | 8,01 | 7 | HW | 6,11 | 7,69 | 6,01 |
| HW | 3,18 | 7,33 | 7,88 | HW | 5,12 | 8,01 | 4,75 |
| OW | 4,35 | 12,75 | 7,34 | OW | 2,17 | 10,87 | 8,34 |
| HW | 4,45 | 13,12 | 8,27 | HW | 1,52 | 11,62 | 8,22 |
| HW | 4,14 | 13,49 | 6,71 | HW | 1,94 | 10,35 | 9,16 |
| C | 4,91 | 2,39 | 6,38 | Cl | -2,98 | 4,68 | 7,64 |
| Oc | 4,91 | 1,8 | 5,34 | Cl | 5,14 | -3,32 | 7,97 |
| Oc | 4,91 | 3,59 | 6,38 | | | | |
| Oc | 4,91 | 1,8 | 7,41 | | | | |

### *5.3.3 Potential parameters*

DL-POLY code [63] has been used in all our simulations. All species were treated as rigid bodies. We employed the CLAYFF [26]for the potential parameter of Montmorillonite, water molecule and others counterions. The signification of using a partial charge CLAYFF model is the flexibility within clay lattice. Flexibility for all other counterions, including OH groups in the clay lattice, was realized with harmonic bond stretch and angle bend terms[27].Parameters for the uranyl ion were taken from Guilbaud and Wipff [28] where the angle bend force constant $k_2$ is 300 kcal.mol$^{-}$1.rad$^{-2}$, and the equilibrium angle for O-U-O is 180°. These parameters were used to model uranyl complexes with carbonate and chloride. For $UO_2^{2+}$, we used a partial charge of +2.5e, which change slightly compared with +2.8e obtained from *ab initio* results. Using these uranyl and Montmorillonite models, we have performed complexes simulations of uranyl with Montmorillonite surface in the presence of $Na^+$, $K^+$, $Cs^+$, $Ba^{2+}$, $Pb^{2+}$, $Ca^{2+}$, $Zn^{2+}$ interlayer cations, as well as carbonate and Chloride. The corresponding parameters are given in Table5-4.

The total energy is expected to have contributions from the long ranged Electrostatic (Coulombic) interactions, the short ranged pair-body (van der Waals) interactions and the bond interaction which include the chemical bond stretch and valence angle bend terms:

$$U_{total}=U_{coul}+U_{pair}+U_{bond}+U_{angle} \quad (5.1)$$

In addition to the 4 terms involved in the equation 5.1, one can define dihedral angles and inversion angles potentials as intra-molecular interactions, three-body, Tersoff and four-body potentials as inter-molecular interactions. However, during the simulation we ignore these terms to avoid time consuming. The corresponding equations for total energy calculation are represented in Table5-4.

MD simulations were performed in the constant NVT (number of particles, volume, and temperature) ensemble at 300K. A time step of 0.001 ps was used. The equilibration time was confined to 1ns of MD simulation to relax our system. Following the equilibration, 1ns of dynamic simulation was added for the statistical analysis of the structural and the (x, y, z) trajectories of uranyl and counter ions in the surface region.

**Talbe 5-4: Force Field parameters for Radionuclides species and Montomorillonite**[15, 32].

| I. nonbond Species | Symbol | Charge (e) | $A_{ij}$ ((kcal. Å$^{12}$/mol)$^{1/2}$) | $B_{ij}$ ((kcal. Å$^{6}$/mol)$^{1/2}$) |
|---|---|---|---|---|
| Sodium ion | Na | +1.0 | 121.503 | 9.3622 |
| Potassium ion | K | +1.0 | 868.623 | 23.438 |
| Cesium ion | Cs | +1.0 | 1999.548 | 35.561 |
| Barium ion | Ba | +2.0 | 1340.126 | 24.105 |
| Plumbum ion | Pb | +2.0 | 2565.915 | 64.690 |
| Calcium ion | Ca | +2.0 | 354.91 | 14.982 |
| Zinc ion | Zn | +2.0 | 78.422 | 7.431 |
| Chloride ion | Cl | -1.0 | 4591.405 | 53.901 |
| Uranium | U | +2.5 | 713.840 | 31.759 |
| Uranyl oxygen | O | -0.25 | 793.310 | 25.009 |
| Carbonate carbon | C | +0.43 | 1338.021 | 22.989 |
| Carbonate oxygen | Oc | -0.81 | 522.393 | 22.336 |

Coulombic potential: $U_{r_{ij}} = \frac{1}{4\pi\epsilon_0}\frac{q_i q_j}{r_{ij}}$ ; Pair − body potential: $U_{r_{ij}} = \left(\frac{A_i A_j}{r_{ij}^{12}}\right) - \left(\frac{B_i B_j}{r_{ij}^{6}}\right)$

Potential energy U(kcal/mol), atomic charge q(e), radius r(Å)

| II. Bonds stretch | | K1(kcal/mol .Å$^2$) | $r_o$(Å) |
|---|---|---|---|
| Species i | Species j | | |
| U | O | 1000 | 1.8 |
| C | Oc | 1312 | 1.25 |

Bond potential:$U_{ij} = \frac{1}{2}k_1(r_{ij}-r_0)^2$ Potential energy U(kcal/mol), bond stretch force constant k1,and equilibrium bond length r0(Å)

| III. Angle bend | | | K2(kcal/mol .rad$^2$) | $\Theta_o$(deg) |
|---|---|---|---|---|
| Species i | Species j | Species k | | |
| O | U | O | 300.00 | 180.00 |
| $O_c$ | C | $O_c$ | 160.00 | 126.00 |

Angle potential:$U_{ijk} = \frac{1}{2}k_2(\theta_{ijk}-\theta_0)^2$ Potential energy U(kcal/mol), angle bend force constant $k_2$, and equilibrium angle $\theta_0$(deg)

## 5.4 Surface energy and work of adhesion

First, MD simulations were performed exclusively on Montmorillonite to explain the interactions between clay sheets. For this purpose, a Montmorillonite bulk and a thin Montmorillonite film were constructed (Fig.5-3). A 4×4×1 supercell was employed and was simulated until 2ns to achieve an equilibrated configuration in the isothermal-isochoric (NVT) canonical ensemble. We have used a cutoff of 10 Å for van der Walls interactions, and an evaluation of Coulomb interactions through Ewald summation with very high accuracy ($10^{-6}$ kcal/mol). This equilibrated structure is representative of the bulk form in a simulation box of 21.12× 36.56 × 10.58 $Å^3$ and is fully periodic in all three directions. The thin films were formed by extending the z dimension of the periodic box to 60Å in order to remove inter molecular interactions between layers.

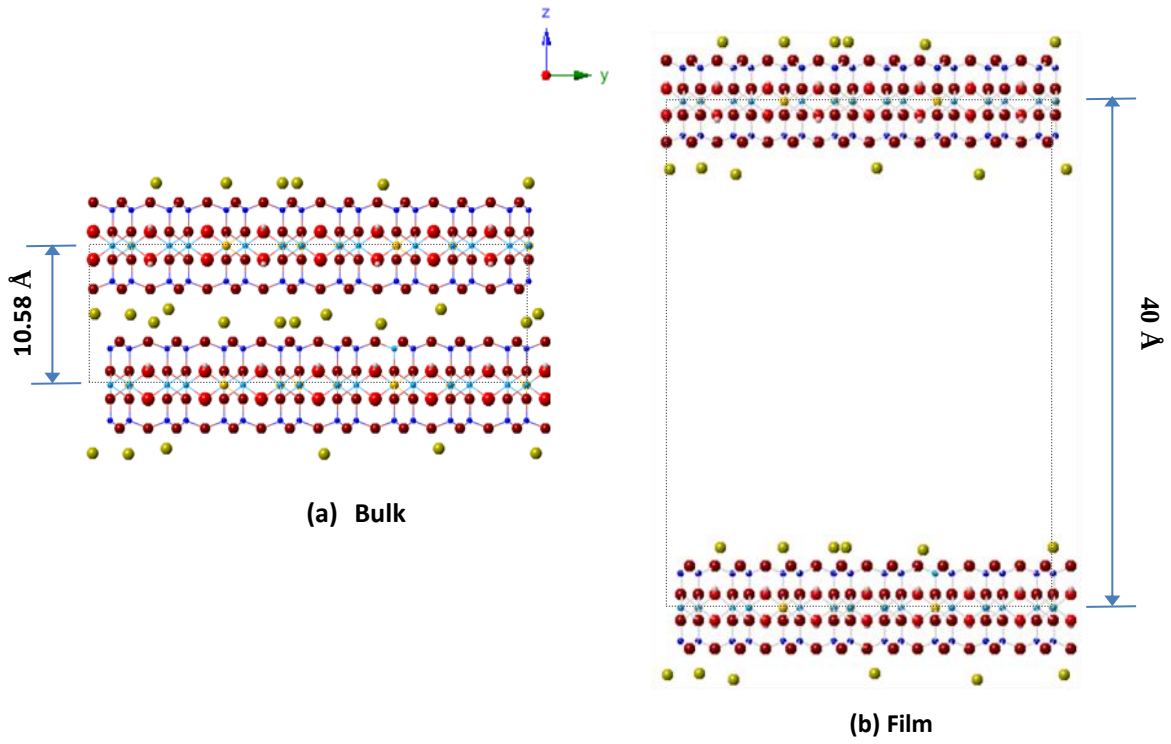


**Fig. .5–3: (a) Bulk molecular structure of MMT with a width of 10.58 Å in z direction of the fully periodic box; (b) film molecular structure of MMT with 40 Å in z direction of the fully periodic box. The surfaces on each side of the sheets are separated by vacuum. Interlayer cation can be Na+, K+, Cs+, $Ba^{2+}$, $Ca^{2+}$, $Pb^{2+}$ and $Zn^{2+}$.**

The surface energy of Montmorillonite can be extracted from the total energies of bulk and film[31]. The average interaction energy between the clay layers has the contributions from Coulomb, van der Waals, internal (bond, angle), and kinetic energies[5].Contributions from kinetic energy are null since all our simulations were computed at constant temperature. The surface energy for 7 MMT structures with different interlayer cations ($Na^+$, $K^+$, $Cs^+$, $Ba^{2+}$, $Pb^{2+}$, $Ca^{2+}$, $Zn^{2+}$) were determined therefore from the following:

$$\boldsymbol{\gamma = \frac{E_{film} - E_{bulk}}{2A}} \qquad \textbf{(5.2)}$$

where $E_{film}$ is the total energy of the thin film structures, $E_{bulk}$ is the total energy of the bulk structure and A is the surface area at the interface.

Secondly, the work of adhesion between the radionuclide and the MMT surface was calculated in the presence of different counter ions according to the following equation:

$$W_A = \frac{(E_U + E_{MMT}) - E_{total}}{2A} \qquad \textbf{(5.3)}$$

Where $E_U$ is the total energy of radioactive thin film. In the present work $(UO_2^{2+})(H_20)_5$, $UO_2(H_20)_5(CO_3)$, and $UO_2(H_20)_5Cl_2$ are considered as the radionuclide element structures in the surface region of MMT (Fig.5-4(abc)). $E_{MMT}$ is the total energy of MMT thin film (Fig.5-4(d)), $E_{total}$ is the total energy of the complex of radionuclide and MMT. A means here the van der Waals contact area between the MMT and the radionuclide element. We put thin films of radionuclide near to the MMT surface and then they were relaxed with 2ns to having possible adsorption complex. In the case of simulation at the radionuclide-MMT interface, free boundary conditions were applied in the direction orthogonal to the MMT surface plane. A total of 42 (7 cations, 3 radionuclide elements of $(UO_2^{2+})(H_20)_5$, $UO_2(H_20)_5(CO_3)$, $UO_2(H_20)_5Cl_2$ and 2 concentrations) complex models are used for the molecular dynamics simulations presented in this study. Typical surface structures of Na-MMT are shown in Fig.5-5. The interlayer region below the slab and surface region above the slab contain net charges of +6e respectively to balance the charge of the clay layer. The simulations have been performed with 6 mono valent cation ($Na^+$, $K^+$, $Cs^+$) or 3 double valents cation ($Ba^{2+}$, $Ca^{2+}$, $Pb^{2+}$ and $Zn^{2+}$) in both regions. However, when we investigate adsorption of charged $(UO_2^{2+})(H_20)_5$ on MMT clay surface, the number of cation in the surface region

changes with the concentration of charged $UO_2^{2+}$. One $(UO_2^{2+})(H_20)_5$ accompanied by 4 mono valents cation or 2 double valents cation and two $(UO_2^{2+})(H_20)_5$ accompanied by 2 mono valents cation or 1 double valents cation to form a charge of +6 e.

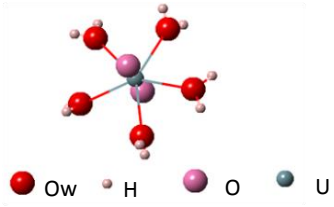


**(a) $(UO_2^{2+})(H_20)_5$**

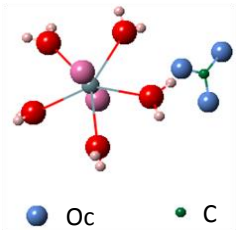


**(b) $UO_2(H_20)_5(CO_3)$**

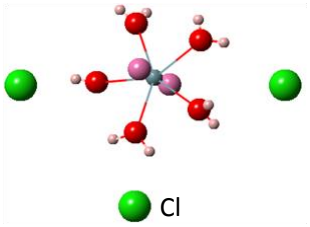


**(c) $UO_2(H_20)_5Cl_2$**

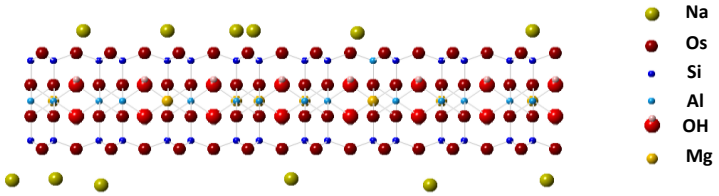


**Fig.5–4: (a) $(UO_2^{2+})(H_20)_5$; (b) $UO_2(H_20)_5(CO_3)$; (c) $UO_2(H_20)_5Cl_2$; (d) film molecular structure of MMT. Atoms colors are labeled aside Fig.**

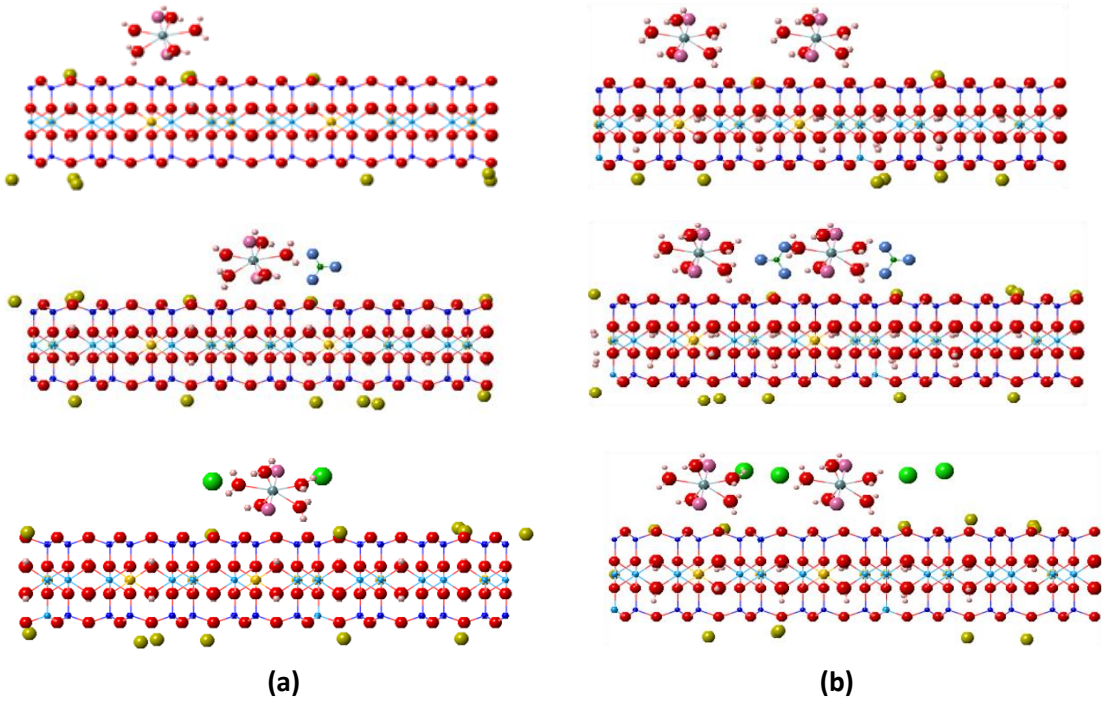


**Fig.5–5: Configuration of each of the three radionuclide elements: $(UO_2^{2+})(H_20)_5$, $UO_2(H_20)_5(CO_3)$ and $UO_2(H_20)_5Cl_2$ (from top to bottom) for: (a) one pair of radionuclide elements; (b) two pairs of radionuclide elements.**

## 5.5 Results and discussion

### *5.5.1 Structural properties of radionuclide complex onto MMT surface*

Representative complex configurations of three radionuclide elements with MMT surface are shown in Figs. 5-6, 5-8 and 5-9. The concentrations of one and two radionuclide molecule (part a and part b of each Fig.) are implemented to investigate the adsorption processes. In order to show clearly the interaction between the surface and radionuclide element, we hide whole MMT structure beside Si-$O_s$ sheet, which forms visual continuous hexagons. We show in Fig.5-6 (a) three typical adsorptions of one uranyl molecule adsorption on MMT: bidentate inner-sphere complex; monodentate inner-sphere complex and outer-sphere adsorption complex (from top to bottom). These kinds of complex appear in two uranyl molecules adsorption simulation (Fig. 5-6(b)). Two uranyl molecules show independent

complex with surface of MMT and no special interaction is observed between uranyl. In the inner-sphere complexes, uranyl was attached to one or two surface oxygen centers for monodentate or bidentate inner-sphere complexes. The two surface oxygen centers bound to the same Si atom for bidentate inner-sphere complexes.

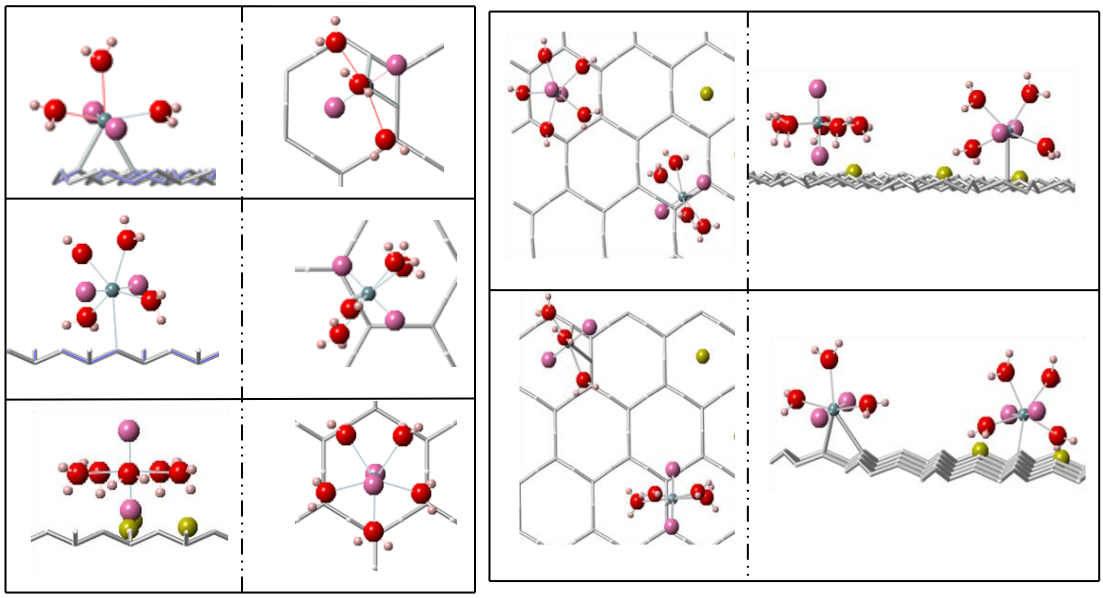

(a) (b)

**Fig.5–6: Snapshot of optimized adsorption structure of one $(UO_2^{2+})(H_20)_5$ molecule adsorbed (from top to bottom: (a) two inner-sphere complex and one outer-sphere complex) on MMT (001) surface; (b) representative complex of two $(UO_2^{2+})(H_20)_5$ molecule adsorbed on MMT (001) surface.**

Atomic density profiles of U and O in $UO_2^{2+}$ as a function of surface distance ($Z-Z_0$) are shown in Fig.5-7. For the outer-sphere complex (Fig.5-7a), U atoms are most likely to be found at 2.9 Å from MMT surface. The uranyl cation is always centered at the midplane with two symmetrical oxygen atoms. The distance between U and O peak centers is equal to the fixed U-O bond length 1.8 Å, which indicates that the O-U-O vector is perpendicular to the MMT surface. Uranyl cation is linked to 5 water oxygen. The distance between U and MMT surface in the inner-sphere complexes is 2.2 Å, which is smaller than that in outer-sphere complexes, and the distance between U and O peak centers is less than the fixed U-O bond. That means the O-U-O vector is tilted from the surface normal in order to fill the surface oxygen atoms.

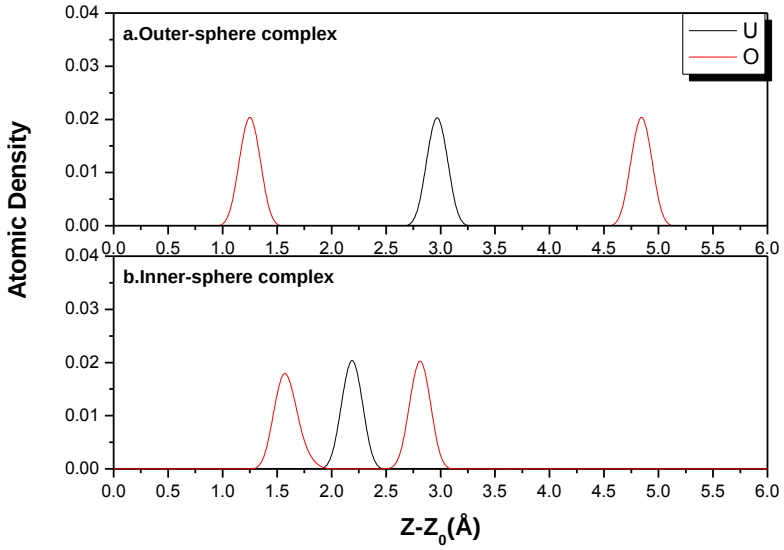


**Fig.5–7: Atomic density profiles for uranyl U and oxygen near the MMT surface of (a) outer-sphere complex;(b) inner-sphere complex. Zo refers to the W coordinate of the nearest surface oxygen.**

Orthogonal views of adsorption complexes of radionuclide element with MMT in the presence of $Cl^-$ and $CO_3^{2-}$ions are shown in Fig.5-8 and Fig.5-9. As excepted uranyl forms complexes with chloride and carbonate ions, and it forms inner or outer-sphere complex with the MMT surface. Typical radial distribution functions (RDFs) of ligands ($O_w$, $O_s$, $Cl^-$, $O_c$) around the U centers of $UO_2^{2+}$ are displayed in Fig. 5-10. For $(UO_2^{2+})(H_20)_5$ radionuclide element, the equilibration coordination shell of complexes consisted of water oxygen ($O_w$) and surface oxygen ($O_s$) in MMT. RDFs of averaged U-ligands ($O_w$ and $O_s$) are shown in Fig. 5-10 where we notice a peak of primary shell at 2.491~2.532 Å for U-$O_w$ and 2.467~2.536 Å for U-$O_s$. The average U-$O_w$ distance of 2.526 Å was given in the outer-sphere complexation $(UO_2^{2+})(H_20)_5$, 2.507 Å and 2.523 Å in the monodentate and bidentate inner-sphere complexation. This indicates that there is no much difference of U-$O_w$ distance between inner-sphere and outer-sphere complexation. For $UO_2(H_20)_5Cl_2$ radionuclide element, the equilibration coordination shell of complexes might be consisted of water oxygen ($O_w$), surface oxygen ($O_s$) and chloride ion ($Cl^-$). Averaged U-ligands results are shown in Fig.5-10. The presence of $Cl^-$ in the uranyl complex results in two peaks of RDF for U-ligands: one corresponding to the primary shell of U-$O_w$ at 2.505~2.532 Å and the second representing the primary shell of U-$Cl^-$ at 2.871~2.983 Å, with chloride ion occupying positions farther

than water oxygen. This means a weaker electrostatic attraction between uranium and chloride ion relative to that between uranium and water oxygen atoms. The red lines in Fig.5-10 show us averaged RDF of U-ligands. For $UO_2(H_20)_5(CO_3)$ radionuclide element, ligands of uranium can be water oxygen, surface oxygen and carbonate oxygen ($O_c$). The presence of $CO_3^{2-}$ in the uranyl complex results in a split equatorial shell about the uranium atom, with oxygen atoms from carbonate occupying positions closer than water oxygen. The RDF analysis gives averaged U-$O_c$ and U-$O_w$ bond length of 2.296~2.426 Å and 2.498~2.554 Å, which indicates a stronger electrostatic attraction between uranium and carbonate oxygen atoms relative to that between uranium and water oxygen atoms.

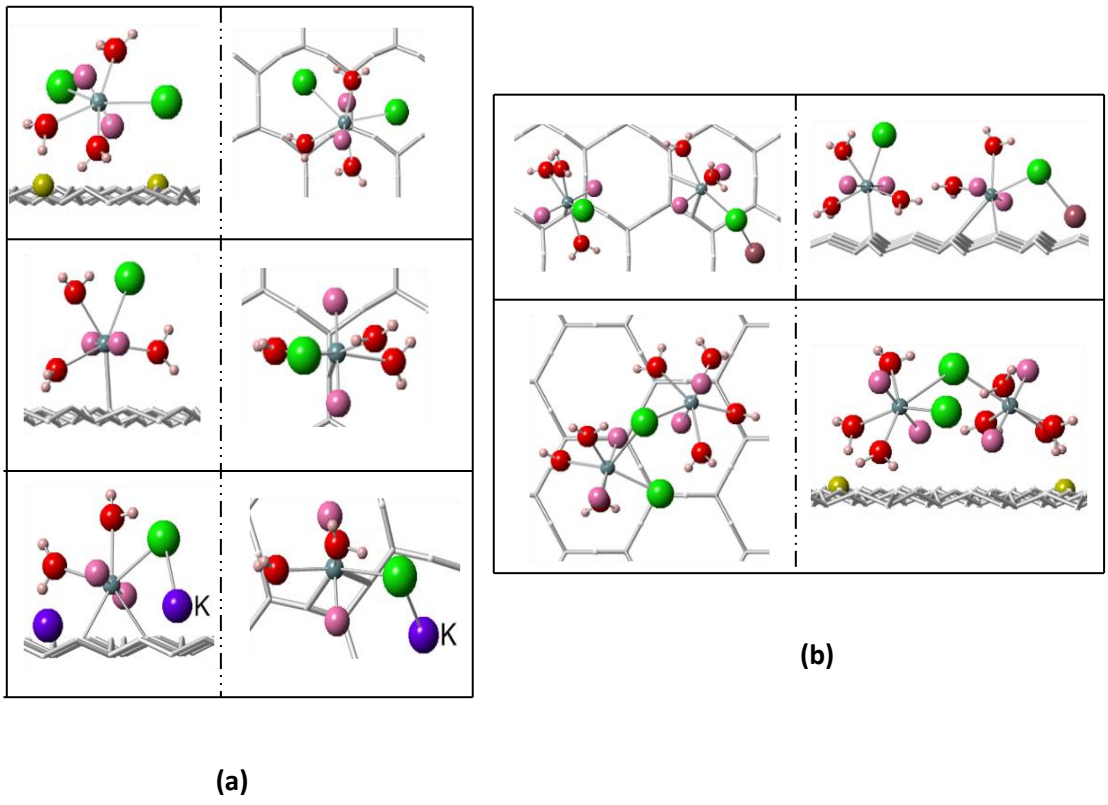


**Fig.5–8: Snapshot of optimized adsorption structure of: (a) one $(UO_2^{2+})(H_20)_5Cl_2$ molecule adsorbed on MMT (001) surface indicating from top to bottom: one outer-sphere complex and two inner-sphere complex; (b) representative complex of two $(UO_2^{2+})(H_20)_5Cl_2$ molecule adsorbed on MMT (001) surface.**

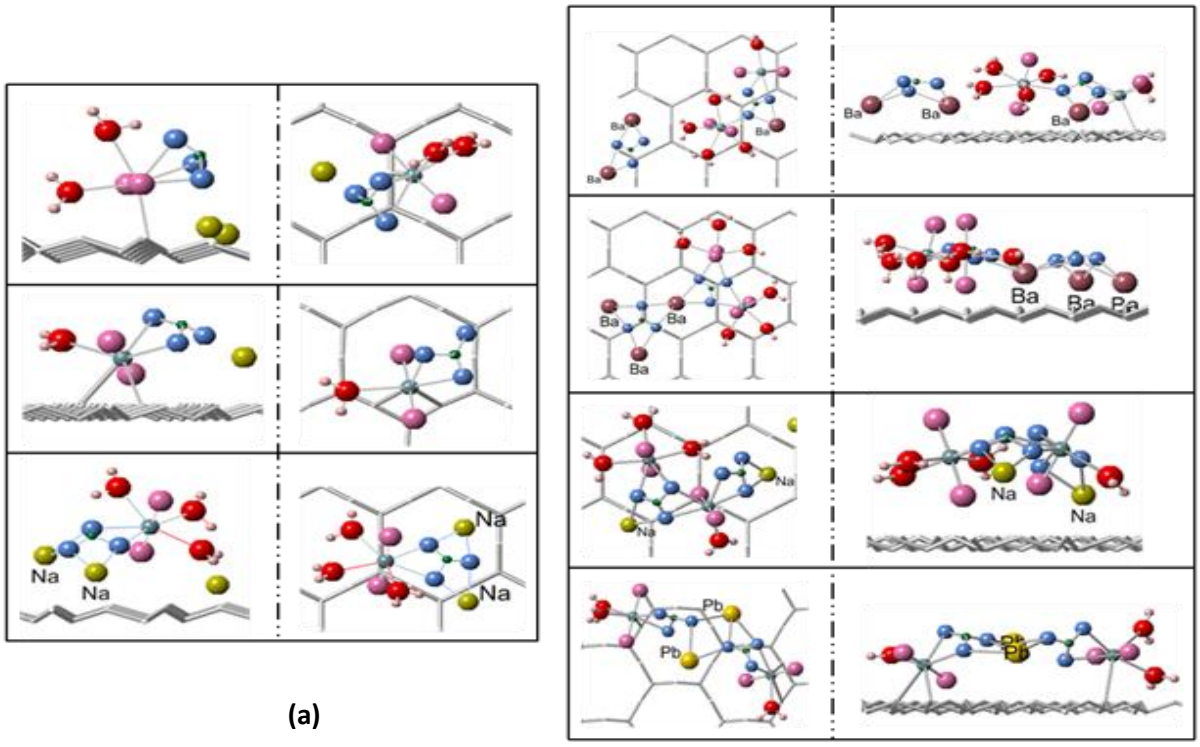


**Fig. 5–9: Snapshot of optimized adsorption structure of: (a) one $UO_2(H_20)_5(CO_3)$ molecule adsorbed on MMT (001) surface. From top to bottom: two inner-sphere complex and one outer-sphere complex; (b) representative complex of two $UO_2(H_20)_5(CO_3)$ molecule adsorbed on MMT (001) surface.**

With the presence of carbonate and chlorite ions in the surface region, we have neutralized radionuclide elements. To balance the charged clay layer, which contains a net charge of -12 e, we placed a net charge of +6 e in both surface region and interlayer region. That's means 6 mono valent cations like $Na^+$, $K^+$, $Cs^+$ or three double valent cations such as $Ca^{2+}$, $Ba^{2+}$, $Pb^{2+}$ and $Zn^{2+}$ were placed in the surface region with radionuclide elements. Both uranyl ions and cations can be adsorbed onto the MMT surface, forming hence a dynamic equilibrium. A cation with higher charge may have stronger electrostatic interactions with MMT surface. For cations with the same charge, adsorption onto clay depends mainly on their ionic radius. A cation with larger ionic radius can be easily adsorbed on the clay surface by the electrostatic interactions. Cesium has the largest ionic radius of 167 pm among seven cations considered here. MMT adsorbs Cs and hence restricts its mobility. Equilibrium snapshot of complexes of neuter radionuclide element with MMT surface are displayed in Fig.5-8 and 5-9, which show that cations can be also adsorbed by carbonate and chlorite ions when their initial distance is less

than 4.0 Å. In Fig.5-11, we see RDF of cation-Cl and cation-Oc, which indicates that the order of bond length of cation-Cl and cation-carbonate oxygen decreases in the order $Cs^{+}>Pb^{2+}>K^{+}>Ba^{2+}>Na^{+}>Zn^{2+}>Ca^{2+}$ and $Cs^{+}>Pb^{2+}>K^{+}>Ba^{2+}>Ca^{2+}>Na^{+}>Zn^{2+}$. The bond length between cations and carbonate oxygen is normally shorter than cations-$Cl^{-}$ bond because of the stronger electrostatic interaction present in carbonate ions. Averaged cations-$Cl^{-}$ distances were measured to be 2.368~ 3.390 Å and cations-Oc distance corresponds to 1.992~2.844 Å. Short bond appears between double valent cations and carbonate oxygen or chlorite ion beside $Pb^{2+}$which is a heavy metal known as one of the most pervasive and elusive environmental health threats. Studies show that the adsorption of lead in soil is mainly specific adsorption and will be difficult to be released[32]. The longest distance of 3.39 Å and 2.85 Å appears between Cs-chlorite and $Cs^{-}$carbonate oxygen because of its stronger adsorption capability to clays than reducing the competitive power of adsorption for chlorite and carbonate.

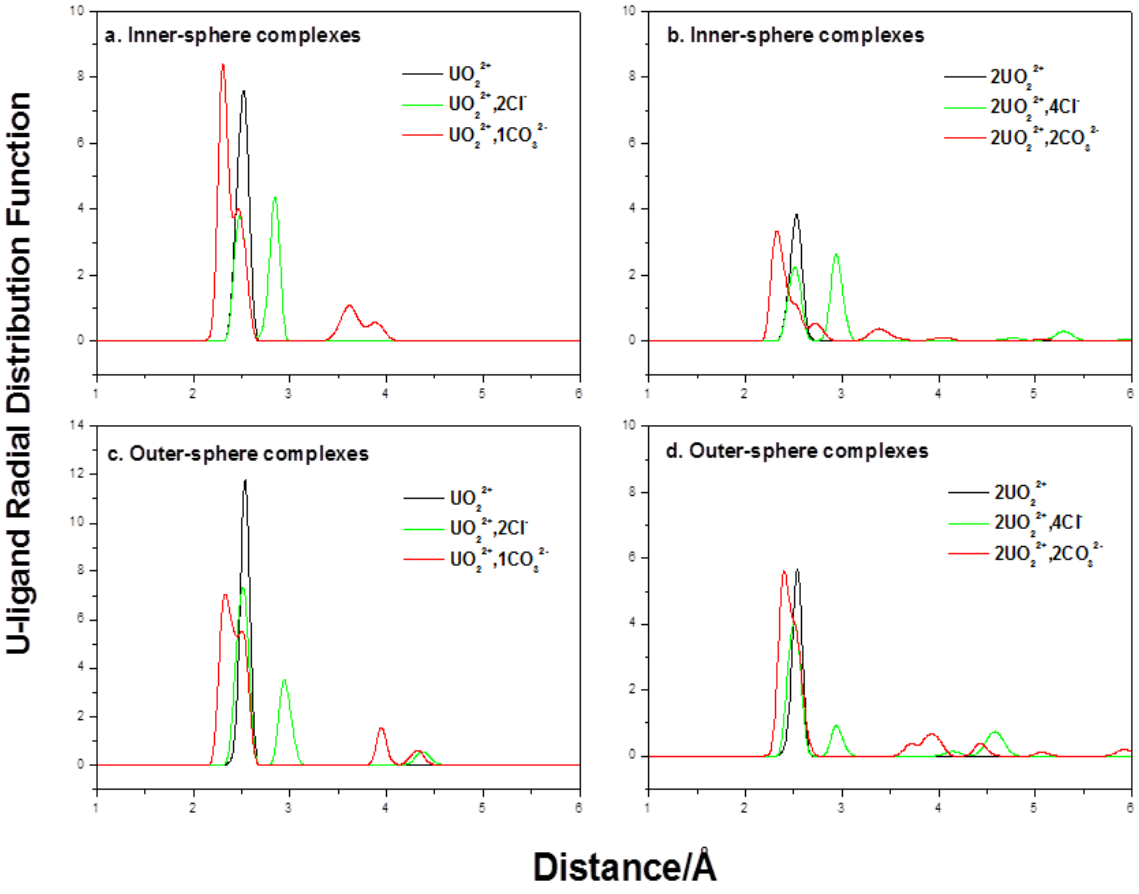


**Fig.5–10: Plots of the U-ligant radial distribution functions for (a) inner-sphere complexes of one radionuclide element; (b) outer-sphere complexes of two radionuclide elements. The black, green and red lines represent radionuclide elements of $(UO_2^{2+})(H_20)_5$, $UO_2(H_20)_5Cl_2$) and $UO_2(H_20)5(CO_3)$, respectively.**

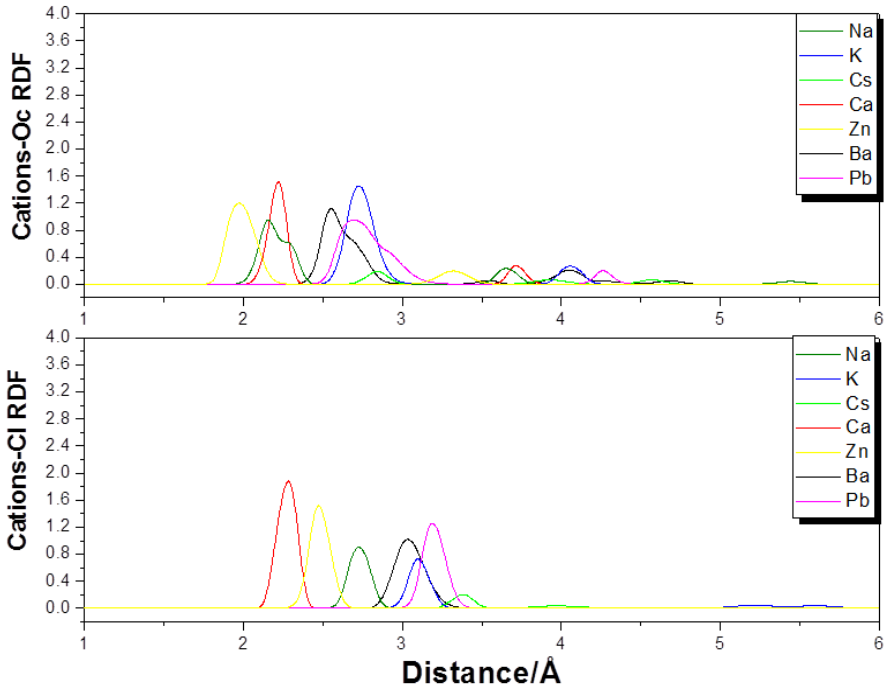


**Fig.5–11: Radial distributions functions of cation-carbonate oxygen and cation-chlorite ions.**

### *5.5.2 Layered MMT surface energy and work of adhesion between adsorption complex and MMT surface*

We started by discussing the interaction between sheets of layered Montmorillonite with different cation. Complete equilibration process of the interface between identical MMT thin films result from a 2ns NVT molecular dynamics run, in the distance as ~50Å, can give an interfacial energy near to zero. The cell for the MMT—MMT interface formed by two thin films was of dimensions 21.12× 36.56 × 60 Å in which the individual MMT thin films were exposed to a vacuum on both sides. We performed the same simulation of 2ns NVT to bulk supercells of 4×4×2 with dimensions of 21.12× 36.56 × 21.16 Å. Then, both of film and bulk final structures were treated as initial structure subjected to NPT molecular dynamics for 1ns to achieve their configuration equilibrium. The surface energy can be extracted from the potential energies of relaxed film and bulk cells. The contributions of surface energy calculated from Equation 5.1 are presented in Table 5.5.

**Table5-5: Obtained contributions to the surface energies (mj/m$^2$) deduced from the differences of bulk and film cells energy.**

| Cation | VDW | Coulomb | BOND | Total |
|---|---|---|---|---|
| Na-MMT | 7.654 | 31.517 | 1.026 | 40.197 |
| K-MMT | 11.706 | 49.528 | 1.557 | 62.791 |
| Cs-MMT | -56.730 | 157.589 | 3.674 | 104.533 |
| Ca-MMT | 1.801 | 72.040 | -2.471 | 71.369 |
| Ba-MMT | 4.952 | 135.076 | -1.413 | 139.299 |
| Pb-MMt | 4.502 | 27.015 | -0.036 | 31.481 |
| Zn-MMT | -1.350 | 90.051 | -1.954 | 86.747 |
| Exp. | | | | 50—200 [34, 37] |

The van der Waals contact of surface area A is considered here as the surface of the thin film of MMT. The main contributions to the formation of the surface energy are the electrostatic interactions changes and the van der Waals interaction changes. Van der Waals interactions are significantly weaker than electrostatic interactions. At equilibrium, interlayer cations are well-distributed; they are strongly attached to both MMT sheets through electrostatic attraction. Some interlayer cations are captivated by anionic Si-Al charge defects in tetrahedral sheet of montmorillonite. In this state, the van der Waals interaction energy is partly repulsive. At about 50Å separation, the MMT surface have already been reconstructed, only half interlayer cations left in each sheet. These cations continue to be attracted by adjacent cavities and most of them are located in the center of hexagons surface. However we consider that there is no van der Waals or electrostatic interaction left between the MMT sheets in vacuum. The simulated value of surface energy from the seven atomistic models is between 31.481 mJ/m2 and 139.299 mJ/m² (Table5.5), which is quantitatively in agreement with experiment [33, 34].

**Table 5-6: Complexes parameters[a] and work of adhesion of one and two radionuclide element adsorption complexes with MMT surface in presence of different cation[b].**

| Uranyl complex | $U\text{-}O_w$ (Å) | $U\text{-}O_s$(Å) | $U\text{-}O_c$(Å) | U-Cl (Å) | Work of Adhesion(J/m$^2$) |
|---|---|---|---|---|---|
| ***One radionuclide element*** | | | | | |
| ***radionuclide specie:*** | | ***$[UO_2(H_2O)_5]^{2+}$*** | | | |
| $[UO_2(H_2O)_5]^{2+}$ | 2.509 ; 2.561 ; 2.538 ; 2.581 ; 2.441 ; | | | | 0.852 |
| $[UO_2(H_2O)_4(O_s)]^{2+}$ | 2.491 ; 2.498 ; 2.532 ; 2.508 : | 2.711 ; | | | 1.259 |
| $[UO_2(H_2O)_3(O_s)_2]^{2+}$ | 2.534 ; 2.522 ; 2.514 ; | 2.467 ; 2.541 ; | | | 1.861 |
| ***radionuclide specie:*** | | ***$[UO_2(H_2O)_5Cl_2]$*** | | | |
| $[Na_2UO_2(H_2O)_3Cl_2]^{2+}$ | 2.496 ; 2.496 ; 2.505 ; | | | 2.983 ; 2.997 ; | 0.610 |
| $\{[NaUO_2(H_2O)_4Cl]^{2+}\}^1$ | 2.536 ; 2.543 ; 2.532 ; 2.577 ; | Na-Os: 2.259 | | 2.871 ; | 1.119 |
| $\{[NaUO_2(H_2O)_4Cl]^{2+}\}^2$ | 2.510 ; 2.521 ; 2.508 ; 2.497 ; | Na-Os: 2.553 | | 3.002 ; | 0.949 |
| $[NaUO_2(H_2O)_3(O_s)_2Cl]^{2+}$ | 2.527 ; 2.478 ; 2.498 ; | 2.570 ; 2.514 ; | | | 0.718 |
| ***radionuclide specie:*** | | ***$[UO_2(H_2O)_5CO_3]$*** | | | |
| $[CsUO_2(H_2O)_2CO_3(O_s)]^+$ | 2.496 ; 2.491 | 2.693 ; ; | 2.338 ; 2.384 ; | | 1.172 |
| $[UO_2(H_2O)_5]^{2+(c)}$ | 2.528 ; 2.541 ; 2.514 ; 2.522 ; 2.500; | | | | 0.536 |
| $Ba_2CO_3$ | | | Ba-Oc 2.570 ; 2.569 ; 2.728 ; 2.505; | | |
| $[BaUO_2(H_2O)CO_3(O_s)]^{2+}$ | 2.475 ; | 2.472 ; | 2.296 ; 2.457 ; 2.655; | | 1.502 |
| $[CaUO_2(H_2O)_2CO_3(O_s)]^{2+}$ | 2.486 ; 2.538 ; | 2.545 ; | 2.340 ; 2.361 ; | | 2.348 |
| $[ZnUO_2(H_2O)_2CO_3]^{2+}$ | 2.492 ; 2.506 ; 2.498 ; 2.538 ; | | 2.284 ; | | 1.851 |

| Uranyl complex | U-$O_w$ (Å) | U-$O_s$(Å) | U-$O_c$(Å) | U-Cl (Å) | Work of Adhesion(J/m²) |
|---|---|---|---|---|---|
| ***Two radionuclide element*** [(d] | | | | | |
| ***radionuclide specie:*** | ***$[(UO_2)_2(H_2O)_{10}Cl_4]$*** | | | | |
| $[Cs(UO_2)_2(H_2O)_4(O_s)_2Cl_3]^{2+}$ | 2.533 ; 2.537 ; | | | 2.988 ; 2.920 ; 3.003 ; | 0.490 |
| | 2.650 ; 2.629 ; | 2.501 ; 2.750 ; | | 2.915 ; | |
| $[Ba(UO_2)(H_2O)_3Cl_2]^{2+(e)}$ | 2.491 ; 2.507 ; 2.498 ; | | | 3.067 ; 2.961 ; ; | 0.650 |
| $[(UO_2)(H_2O)_2Cl(Os)_2]^{+}$ | 2.506 ; 2.491 ; | 2.553 ; 2.502 ; | | 2.876 ; | |
| $[K_3(UO_2)_2(H_2O)_7(O_s)_2Cl_4]^{3+}$ | 2.469; 2.473; 2.453; | 2.622 ; 2.509; | | | 0.432 |
| | 2.488; 2.511; 2.494 ; 2.510; | | | 2.953; | |
| $[Na_4(UO_2)_2(H_2O)_8Cl_4]^{4+}$ | 2.576 ; 2.510 ; 2.492 ; 2.512 ; | | | 2.920 ; | 0.422 |
| | 2.509 ; 2.555 ; 2.489 ; 2.415 ; | | | 2.961 ; | |
| ***radionuclide specie:*** | ***$[(UO_2)_2(H_2O)_{10}(CO_3)_2]$*** | | | | |
| $[Ca_2(UO_2)_2(H_2O)_4(CO_3)_2]^{4+}$ | 2.689 ; 2.683 ; 2.567 ; | | 2.498 ; 2.298 ; | | 1.082 |
| | 2.507 ; | | 2.322 ; 2.329 ; 2.577 ; 2.347 ; | | |
| $[K_2(UO_2)_2(H_2O)_4(CO_3)_2]^{2+}$ | 2.596 ; 2.418 ; 2.561 ; | | 2.238 ; 2.516 ; | | 0.424 |
| | 2.540 ; | | 2.426 ; 2.440 ; 2.340 ; 2.343 ; | | |
| $[Na_2(UO_2)_2(H_2O)_5(CO_3)_2]^{2+}$ | 2.644 ; 2.597 ; 2.584 ; | | 2.399 ; 2.411 ; 2.511 ; | | 0.492 |
| | 2.494 ; 2.540 ; | | 2.448 ; 2.350 ; 2.419 ; 2.391 ; | | |
| $[Pb_2(UO_2)_2(H_2O)_3(CO_3)_2(O_s)_2]^{4}$ | 2.407 ; | | 2.352 ; 2.478 ; 2.333 ; 2.352 ; | | 0.888 |
| | 2.570 ; 2.580 ; | 2.574 ; 2.599 ; | 2.347 ; | | |

| | | | | | |
|---|---|---|---|---|---|
| $[Zn(UO_2)_2(H_2O)_5(CO_3)_2]^{2+}$ | 2.582 ; 2.594 ; 2.605 ; | 2.703 ; | 2.282 ; | | 1.414 |
| | 2.575 ; 2.702 ; 2.560 ; | | 2.365 ; 2.271 ; | | |
| $[Ba_3(UO_2)(H_2O)_3(CO_3)_2]^{2+(e)}$ | 2.662 ; 2.629 ; 2.491 ; | | 2.286 ; 2.368 ; | | 0.513 |
| $[(UO_2)(H_2O)_3(O_s)_2]^{2+}$ | 2.558 ; 2.506 ; 2.516 ; | 2.475 ; 2.686 ; | | | |

(a) $U\text{-}O_w$ bond length to aqua ligands, $U\text{-}O_s$ bond length to surface oxygen centers, $U\text{-}O_c$ bond length to carbonate oxygen centers, U-Cl bond length to chlorite ion. Work of Adhesion corresponds to the complex form in the first line of uranyl complex.

(b) $Na^+$; $K^+$; $Cs^+$; $Ca^{2+}$; $Ba^{2+}$; $Pb^{2+}$ and $Zn^{2+}$ were consisted like cation in this work.

(c) A independent $BaCO_3$ molecule was observed in surface complex.

(d) Two radionuclide elements contain two U atoms, complexes parameters were listed in two lines for different U atom.

(e) Two radionuclide elements complex apart with the MMT surface.

The interface between the radionuclide element and clay structure is formed from the positioning of the radionuclide element above the relaxed Montmorillonite thin film. The distance to the nearest surface oxygen centers from U atom is about 4 Å. The surface size of Montmorillonite (21.12×36.56) in xy plane is larger than the radionuclide element size. To have the most possible adsorption complexes, we have tested six different surface position of radionuclide element for each model. The cell for the U-MMT interface formed by two thin films was of dimension 21.12×36.56×20 Å, which was simulated by NVT molecular dynamics at 300K for 2ns. To acquire their own energy of radionuclide element and MMT thin film, the separated thin films were relaxed and equilibrated at the same conditions. All these adsorption simulations were performed using two-dimensional (xy plane) periodic boundary conditions as discussed above. Interfacial properties for complexes of radionuclide element and MMT surface were estimated with the average values shown in Table 5-6. The works of adhesion calculated from Equation 5.2 are presented in Table 5-6 as well. The van der Waals contact surface area A is considered here as the real contact area between the adsorption complexes and the MMT surface. The van der Waals contact area A at the MMT surface changes with the complexes configuration. To calculate the van der Waals contact area A corresponding to a complex, we simply plotted the vertical projection of the

equilibrated complex on the MMT surface using van der Waals' radius of all the constituent atoms and copied the shape of the projection to AUTOCAD [35]. The dimension of this region can be then determinated. A prototype example is shown in Fig. 10-12(a). The top view of an equilibrated adsorption complex was presented on the left of Fig.10-12(a), and the shaded surface on the right of Fig. 10-12(a) was calculated as the van der Waals contact area of this adsorption complex using van der Waals' radii of all atoms.

(a) Van der Waals contact area

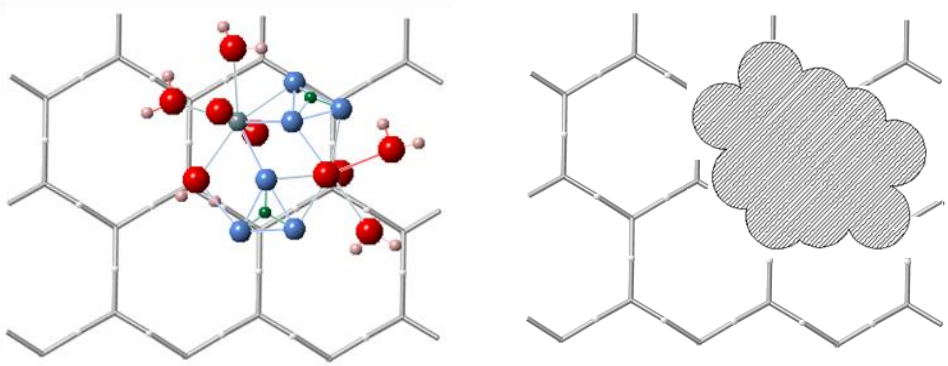

(b) Van der Waals contact area comparison

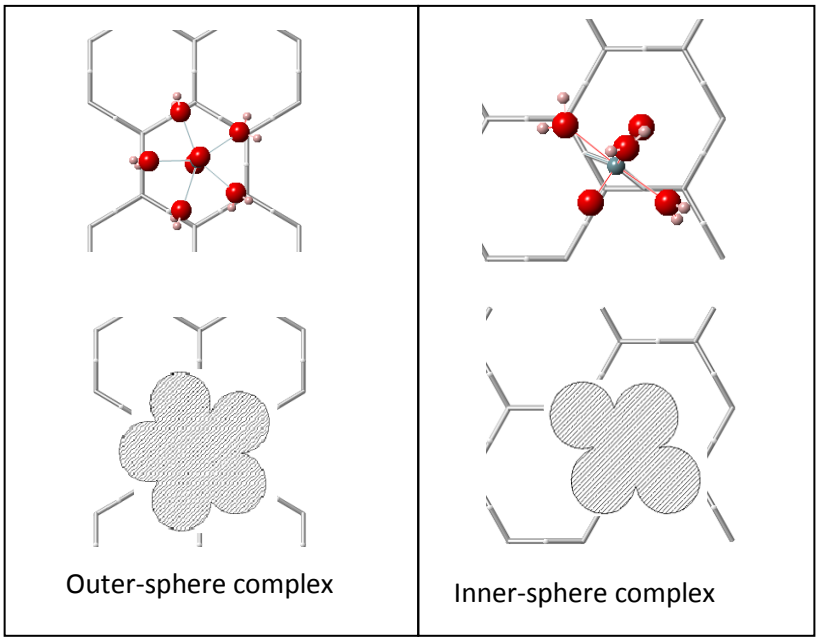


**Fig. 5–12: (a) Top view of the equilibrated adsorption complex (on the left) and vertical projection of the complex on the xy plane (on the right) used for calculation of the van der Waals contact area; (b) Van der Waals contact area comparison for outer-sphere complex with the presence of only one uranyl and its vertical projection area on MMT surface on the left and bidentate inner-sphere complex with the presence of only one uranyl and its vertical projection area on MMT surface on the right.**

Various representative complexes results are listed in Table 5-6. The radionuclide molecule has approached the MMT surface to an equilibrium distance of 2.950±0.720 Å from U atoms to surface oxygen centers. Both positively charged interlayer cations and uranyl ions can absorb onto the MMT surface by electrostatic attraction. In the same time, negatively charged carbonate ions and chlorite ions can be attracted by adjacent interlayer cations and uranyl ions forming a dynamic equilibrium. The conformation of adsorption complex depends on the presence of interlayer cations; radionuclide species and their distance. However, the most possible adsorption complexes observed in our study is the combination of interlayer cations, uranyl and carbonate ions or chlorite ions. The interaction between two thin films contains 'Uranyl-MMT surface' interaction, as well as 'interlayer cations-carbonate ions or chlorite ions' interactions. Work of adhesion is affected by complex conformation; bond formation (U-Os) and van der Waals contact area. The works of adhesion of adsorption complexes correspond to 0.536~2.348 J/m² (Table 3) in the presence of only one radionuclide species. Bond formation between Uranium ions and surface oxygen centers are generally caused by the distribution of the superficial Si→Al charge defects. The affinity of the negatively charged defects makes uranium ions approach and finally break some U-Ow bonds to form new U-Os bond with surface oxygen atom that most adjacent to the defects. Work of adhesion tendency was found to increase as the U-Os bond formation number decreases. When there is no formation of bond between U atom and surface oxygen due to the long distance between Uranyl and nearest Si→Al charge defects, U atoms are most likely to be found at more than 2.9 Å from MMT surface and the O-U-O axis is perpendicular to the MMT surface. For bidentate inner-sphere adsorption complexes with two U-Os bond formation, U-Os bond length are found to be ~2.5 Å, the O-U-O vector is tilted from the normal surface in order to coordinate to surface oxygen centers to form chemical bonds. It is obvious that, with the appearance of chemical bond formation of U-Os, the interaction of inner-sphere complexes with MMT surface is stronger than that of outer-sphere complexes with MMT surface. In addition, Fig. 10-12(b) indicates that the van der Waals contact area of outer-sphere adsorption complex is bigger than that of inner-sphere adsorption complex. Therefore it is reasonable that we obtain a work of adhesion of 0.856 J/m² for outer-sphere complex compared with the work of adhesion of 1.861 J/m² for bidentate inner-sphere complex. As we mentioned above,

interaction energy between radionuclide species and MMT surface can be affected by 'Uranyl-MMT surface' interaction and 'interlayer cations-carbonate ions or chlorite ions' interactions. When there is no bond formation of U-Os, that means no direct interaction of 'Uranyl-MMT surface' and therefore interlayer cations will play an important role. We may take the adsorption complex $[Na_2UO_2(H_2O)_3Cl_2]^{2+}$ like an example. There is no bond formation between radionuclide specie $[UO_2(H_2O)_5Cl_2]$ and MMT surface. However, $Na^+$ ions have linked with Cl- ions with a bond length of ~2.750 Å, and Na-Cl play a role of bridge to connect MMT surface in one side and U atom in another side. This kind of interaction energy is smaller than that with bond formation; we found thus work of adhesion of 0.610 J/m² for this complex which is relatively weaker. Other interesting findings are shown is Table 5-6. $\{[NaUO_2(H_2O)_4Cl]^{2+}\}^1$ and $\{[NaUO_2(H_2O)_4Cl]^{2+}\}^2$ have the same complex conformation, nevertheless, we obtain different work of adhesion result of 1.119 J/m² and 0.949 J/m² respectively. The reason can be explained by the different positions of these two complexes. The first complex is close to a superficial defect and $Na^+$ ions in this adsorption complex is linked with a surface oxygen atom, which is adjacent to a negatively charged Si→Al defect with Na-Os distance of 2.259 Å; while $Na^+$ in the second one is far away from the negatively charged defects. The distance of Na-Os in the second complex is about 2.553 Å that cause the weaker work of adhesion.

As we may see in Table 5-6, compared with $Cl^-$ ions, the presence of $CO_3^{2-}$ ions in radionuclide specie induce a relative stronger work of adhesion between adsorption complex and MMT surface. This is generated by the strong electrostatic attraction within $CO_3^{2-}$ and interlayer cations. Although the presence of $CO_3^2$ ions influences the conformation and work of adhesion of complex, we can't neglect the importance of interlayer cations. Double valent cations such as Ca²+, Ba²+, Pb²+ and Zn²+ produce powerful chemical bond with oxygen in $CO_3^{2-}$. Furthermore, as we discussed above, for cations with the same charge, the one with shorter ionic radius exhibits stronger coulomb attraction with $CO_3^{2-}$. As shown is Table 5-6, similar complexes of $[CaUO_2(H_2O)_2CO_3(O_s)]^{2+}$ and $[BaUO_2(H_2O)CO_3(O_s)]^{2+}$ have been obtained with the presence of $Ca^{2+}$ and $Ba^{2+}$. However, different values of work of adhesion are observed, 2.348 J/m² and 1.502 J/m² respectively with $Ca^{2+}$ ionic radius of 99 pm and $Ba^{2+}$ ionic radius of 135 pm. $Cs^+$ ions have the longest ionic radius of 169 pm among these 7 interlayer cations, that result a

longest bond distance between Cs-carbonate oxygen. Therefore, even if a bond formation of U-Os is built, the work of adhesion of adsorption complex $[CsUO_2(H_2O)_2CO_3(O_s)]^+$ remains 1.172 J/m² that is weaker compared with $[CaUO_2(H_2O)_2CO_3(O_s)]^{2+}$ and $[BaUO_2(H_2O)CO_3(O_s)]^{2+}$, which have the same bond formation.

With increasing radionuclide species to 2 molecules, various forms of complexes can be noticed as presented in the second part of Table 5-6. The interaction energy between the adsorption complexes and MMT surface has no major changes as interlayer cations number and MMT bulk charge remains invariant while the Van der Waals contact area were observed twice or more as much as that of only one radionuclide specie. These were the raisons for which the work of adhesion of two radionuclide species was found to be 0.422 J/m²~1.414 J/m². In this part of simulation, the two uranyl molecules can form a complete adsorption complex with MMT surface, or, they can create individual complex for each uranly molecule with MMT surface like $[Ba_3(UO_2)(H_2O)_3(CO_3)_2]^{2+}$ and $[(UO_2)(H_2O)_3(O_s)_2]^{2+}$ (Table 3). The corresponding work of adhesion is 0.513 J/m², which is rather weak. This is due to the important Van der Waals contact area between these two complexes and MMT surface.

## 5.6 Conclusion

We have carried out a computational approach to study the adsorption of radionuclide elements on the surface of Montmorillonite. We have found that carbonate oxygen has relatively strong bound to uranium ion with a minimum bond length U-Oc of 2.238 Å. The bond length of U-Cl can achieve a maximum of 3.067 Å. From the analysis of computed structures of adsorbed complexes, we have found that chlorite ion and carbonate ions can be attracted by cations with electrostatic attraction.

In addition, the work of adhesion between radionuclide elements and Montmorillonite surface were evaluated. The radionuclide elements may have relatively strong bonds formation with the surface oxygen centers to achieve a work of adhesion of 2.348 J/m². The surface energy between Montmorillonite sheets was found to be smaller than the work of adhesion between radionuclide elements and Montmorillonite surface. As expected, the work of adhesion on the charged MMT surface increases with increasing number of U-$O_s$ bond formation and the chemical interaction between

interlayer cations and $CO_3^{2+}$ or $Cl^-$ ions. A particular attention was paid to the superficial Si→Al charge defects because of the electrostatic attraction to the interlayer cations that is transmitted to negatively charged $CO3^{2+}$ and Cl- ions in radionuclide species. Interlayer cations attach to surface oxygen close to negatively charged defects, and then, the interlayer cation-surface oxygen will play a role of bridge to connect a nearby radionuclide species to form adsorption complex.

# Chapter 6. Structure and diffusion behaviour of carbon dioxide in hydrates calcium Montmorillonite Clay

## 6.1 Abstract

This work performs a Monte Carlo and Molecular Dynamics study toward a molecular understanding of the thermodynamic characteristics of carbon dioxide in hydrated Ca-Montmorillonite. The swelling behaviour of hydrated Wyoming-type Montmorillonite including the carbon dioxide molecules and counterions are presented. In addition, the atom density profile, diffusion behaviors and RDFs of carbon dioxide, interlayer water molecules and Calcium ions have been investigated at different geological burial depth of 0km, 3km and 6km, which correspond to different temperature and pressure of simulation conditions. Furthermore, the influence of different hydration state to the dynamical behaviours of carbon dioxide will be discussed. The calculated self-diffusion coefficient shows that the carbon dioxide species diffuse more freely with the increase of depth and water content. We also found that the presence of the interlayer $CO_2$ inhibits the diffusion of all the mobile species.

## 6.2 Introduction

Montmorillonite is known as swelling clay whose volume is variable with his water content. Montmorillonite will swell when the water content in the clay increases. The distance between the centers of layers is specified by the layer spacing, which equal to the distance between neighbouring mineral layers plus the thickness of one mineral layer. There have been several studies [7, 72-75]aimed at the description of the structure and dynamics behaviour of water and counterions in smectite clay such as interlayer spacing and thermodynamic properties of water and counterions. The layer spacing is variable upon the cations and the number of water molecules contained. On both sides of the clay's surfaces, there are oxygen centers which lead to weak VDW interactions between layers. The role of the counterions in the interlayer space is to join the clay layers together.

Recently, much attention has been paid to the study of the adsorption of carbon dioxide molecules onto hydrated clay surfaces[76, 77]. These investigations are, in general, experimentally difficult and may be supplemented by using molecular simulation. Computer simulation has been used to study the structure and dynamics of carbon dioxide in hydrated calcium montmorillonite clays under conditions encountered in sedimentary basins. It was observed that an increase in pressure or in temperature causes a larger swelling and an increase in the self-diffusion coefficient for the water and carbon dioxide molecules.

The simulation cell contained this 21.12×18.28 $Å^2$ slab of Montmorillonite clay, 3 charge compensating calcium cations, 32 carbon dioxide particles, and 32, 64, and 96 water molecules, corresponding loosely to one-, two- and three-layer hydrate systems, respectively. The simulated system followed gradients of 150 bar km-1 and 30 K/km to burial depth of 3 km and 6 km. temperature and pressure conditions corresponding to specific burial depth of 0, 3, and 6 km were introduced in the simulation.

A combination of constant stress Monte Carlo (MC) and constant volume molecular dynamics (MD) methods have been used in our computations, using the codes ' MONTE' and ' DLPOLY', respectively. In the simulation cell, water and carbon dioxide molecules were initially arranged randomly from MC

simulations. The interlayer cations were selected randomly to move for 2 million MC steps and then 8 million MC steps for the movement of water and carbon dioxide molecules. This gives information on interlayer species positions and clay layer spacing. The equilibrium configurations obtained from MC simulations were then used as initial configurations in the MD simulations. The MD simulations were performed with a timestep of 0.5 ps using an NVT ensemble. The equilibration time was confined to 2 ns of MD simulation to relax the system. After the equilibration, 2 ns of dynamic simulation are added for the statistical analysis of the structure. Interlayer molecular configurations were stored every 500 steps and used for results analysis. The 3-dimensional periodic boundary conditions have been used in the simulation. The equilibrated simulation cell was doubled in the direction normal to the clay sheets for our molecular dynamics runs. This allows us to use a cutoff distance of 9 Å in the minimum image convention, according to the MD program DLPOLY.

The single point charge (SPC) water models[78] has been chosen for liquid water to represent the water, hydroxyl and oxygen –oxygen interactions, where water was treated as a rigid body. The potential model used for carbon dioxide is based on the EPM2 model [79] . These interactions are pair-wise additive involving Coulomb and Lennard-Jones 6-12 potential of the form:

$$\mathbf{U(r)} = \sum\left(\frac{\mathbf{q_i q_j}}{\mathbf{r_{ij}}} - \frac{\mathbf{A_{ij}}}{\mathbf{r_{ij}^6}} + \frac{\mathbf{B_{ij}}}{\mathbf{r_{ij}^{12}}}\right) \qquad \textbf{(6.1)}$$

Where U is the potential energy of the system, q is the partial charge on a site, and A and B represent the van der Waals attractive and short-range repulsive terms, respectively. The potential parameters employed in the simulation are shown in Table6-1.

**Table6-1: Parameters of the SPC[78] and EPM2[79] models.**

| Atom type | $A_{ii}$(kcal Å$^{12}$/mol) | $B_{ii}$(kcal Å$^{6}$/mol) | $q_i$(e) |
|---|---|---|---|
| Ow | 629342 | 625 | -0.8200 |
| Hw | 0 | 0 | 0.4100 |
| Cc | 43581 | 99.244 | 0.6512 |
| Oc | 390222 | 501.301 | -0.3256 |

In this work, using Monte Carlo molecular simulation method, we study first the underlying mechanism of Ca-montmorillonite swelling with increasing hydrated degree in the presence of carbon dioxide particles. Thereafter, we determine the structure and mobility of carbon dioxide in the interlayer region of calcium montmorillonite hydrated clay by means of Molecular Dynamics simulation method.

## 6.3 Swelling of Montmorillonite at elevated pressures and temperatures

We performer here three different sets of simulations on the clay-carbon dioxide system starting from the structure of dehydrate state having non water but 32 carbon dioxide molecules and then a one-layer hydrate having 32 water molecules rising to a two-layer with 64 water, through to a three-layer with 96 water. Each was studied at different temperatures and stresses, chosen to correspond to specific burial depths of 0, 3 and 6 km under gradients of 150bar km$^{-1}$ and 30 K/km. The number of carbon dioxide molecules was keeping to 32 for all these simulations. The Monte Carlo simulation on each set resulted in an equilibrium layer spacing as shown in Table 6-2. The calculated layer spacing was found to increase with burial depths. The layer spacing increases when it adsorbs more and more water molecules for the same temperature and stresses conditions. In Fig. 6-1 we show the structure of Ca-MMT as prototype, in different hydration at room temperature. The layer spacing for a semectite clay depends upon several variables: the temperature, applied pressure, water chemical potential, the magnitude and location of the negative clay layer charge, the identity of the charge-balancing cations that reside in the interlayer. Mooney et al.[80] and Brindley et al. [81]have found that in the presence of water these cations tend to hydrate, thereby forcing the clay layers apart in a series of discrete steps.

Physics allow us to explain the resulting phenomena in the Monto Carlo simulations. As the temperature and pressure increase, the vibration of cations and water molecules becomes more and more important which will generate pressure on the clay lattice and try to push the neighbouring clay layers apart. On the other hand, the van der Waals interaction between the neighbouring clay layers as well as the Coulombic force generated by the cations locating in the interlayer space of clay will keep the layer together.

At low hydrated state, the interlayer space of the clay is small, the van der Waals and Coulombic interactions are relatively important. Since the number of water molecules is small and the vibration force will be weak, it is difficult to separate the neighbouring clay layers especially in z-direction. In contrast, at high hydrated state, the z-distance between neighbouring clay layers is big and the interlayer force becomes weak, what means that the layers will be separated easily. With increasing temperature, the vibration of numerous water molecules as well as the cations will be important enough to push the neighbouring clay layers apart. So the swelling behaviour of the high hydrated clay is obvious under the effect of temperature and pressure.

**Table 6-2: Calculated clay layer spacing (Å) for hydrated Ca-montmorillonite with carbon dioxide particles as a function of depth.**

| Depth/km | 0- layer (0-$H_2O$) layer spacing(Å) | 1- layer(32-$H_2O$) layer spacing(Å) | 2- layer(64-$H_2O$) layer spacing(Å) | 3- layer(96-$H_2O$) layer spacing(Å) |
|---|---|---|---|---|
| 0.0 | 13.97 | 15.70 | 18.86 | 21.36 |
| 3.0 | 14.04 | 16.75 | 19.61 | 22.21 |
| 6.0 | 14.44 | 17.38 | 21.05 | 23.65 |

The calculated layer spacing was compared to that of 2 layers hydrated K-MMT, Li-MMT and Na-MMT in Table6-3. We found that the layer spacing of 2-layer hydrated Ca-MMT is consistently lower than that with monovalent cations. This behaviour is generally caused by charge number; the divalent $Ca^{2+}$ cations can absorb more water molecules around than monovalent cations. The number of the double valent cation is the half of the monovalent ions.

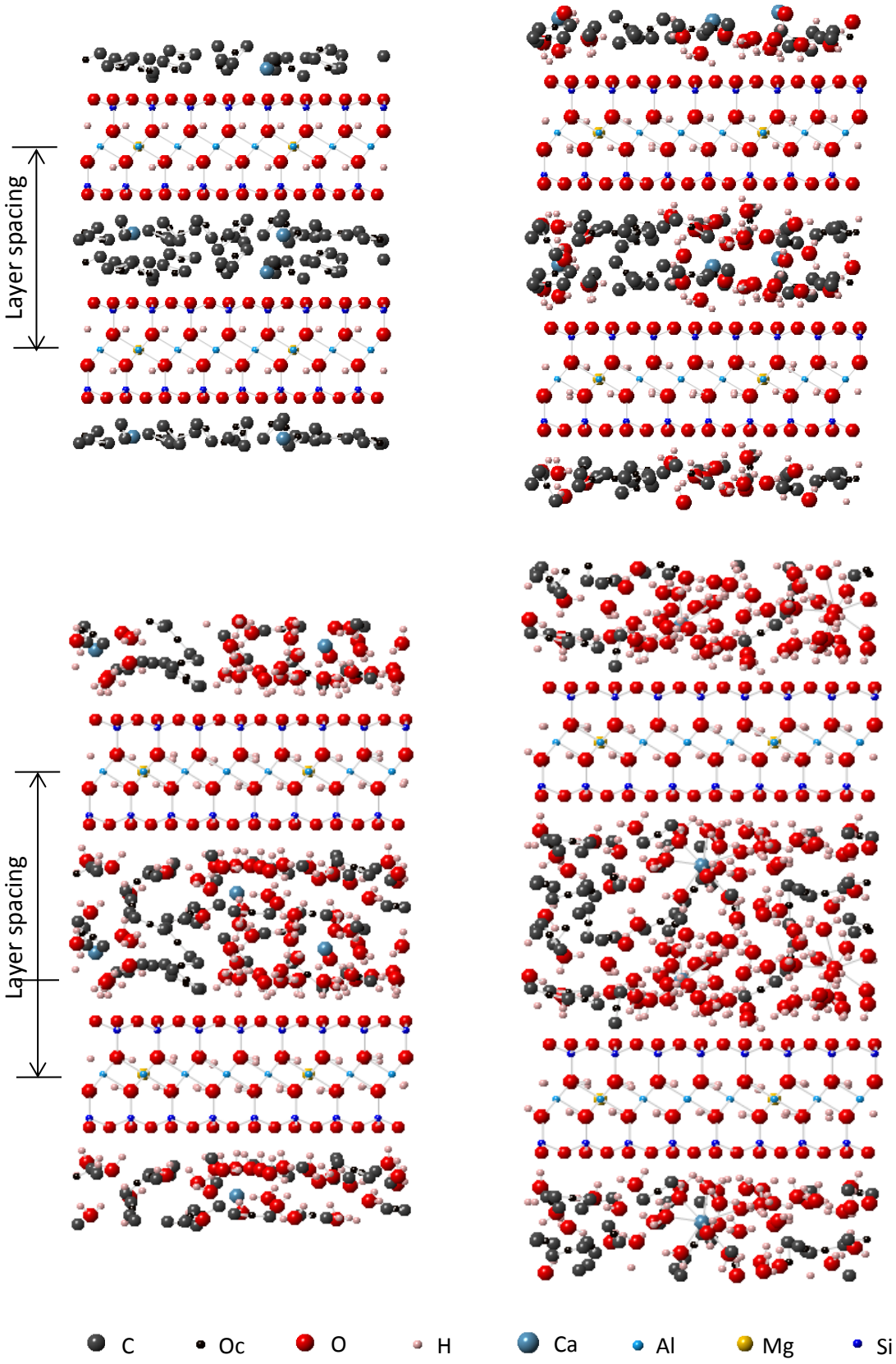


**Fig. 6–1: Relaxed structure of dehydrate, monolayer hydrate, two-layer hydrate and three-layer hydrate Ca-Wyoming montmorillonite at room temperature.**

**Table 6-3: Calculated clay layer spacing for 2-layer hydrated Ca-MMT with Carbon dioxide particles as a function of depths compared to hydrated K-, Li- and Na-MMT.**

| Depth/km | 2-layer Ca-MMT layer spacing(Å) | 2-layer K-MMT layer spacing(Å) | 2-layer Na-MMT layer spacing(Å) | 2-layer Li-MMT layer spacing(Å) |
|---|---|---|---|---|
| 0.0 | 18.93 | 19.12 | 18.87 | 18.90 |
| 3.0 | 19.61 | 19.97 | 19.69 | 19.71 |
| 6.0 | 20.81 | 21.39 | 21.00 | 20.94 |

## 6.4 Carbon dioxide and Water distribution and mobility

The density profiles carbon atoms of $CO_2$ molecules in three different depths for one layer hydrate system are plotted in Fig6-2, where z coordinate represents the distance to the mid-plane of solid layer. The typical layer spacing for one-layer hydrate systems is of the order of 16 Å. There are two large atom density peaks close to the layer surface. In the interlayer space, we can distinguish two major regions, one is near the layer surface and another is in the less structured inner layer. As an increase in the interlayer space width with a fixed number of $CO_2$, the density profile begin to have the third large atom density peak in the middle of interlayer space for two layer hydrate system (Fig.6-3). There is the gradual tendency for Carbon dioxide particles to loose coordination to surface oxygen, and become more fully solvated to water molecules. We may see from Fig 6-4 that there are four large atom density peaks for carbon atoms, two close to the layer surface and two to the interlayer space. This is due to the expansion of interlayer region.

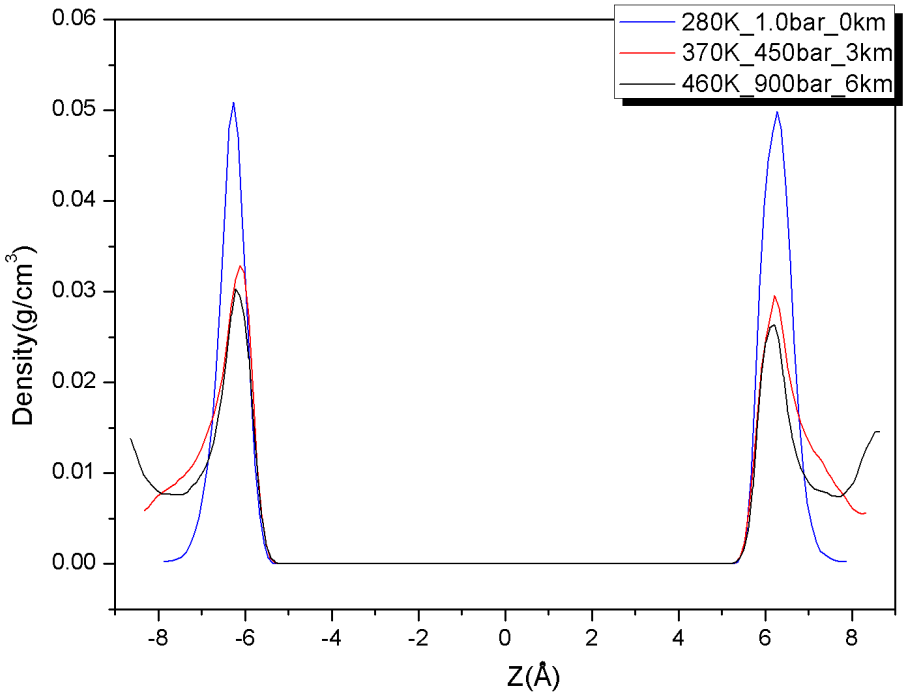


**Fig. 6–2: Density profiles for Carbon atoms as a function of distance from mid-plane of solid layer at different burial depths for one layer hydrate system.**

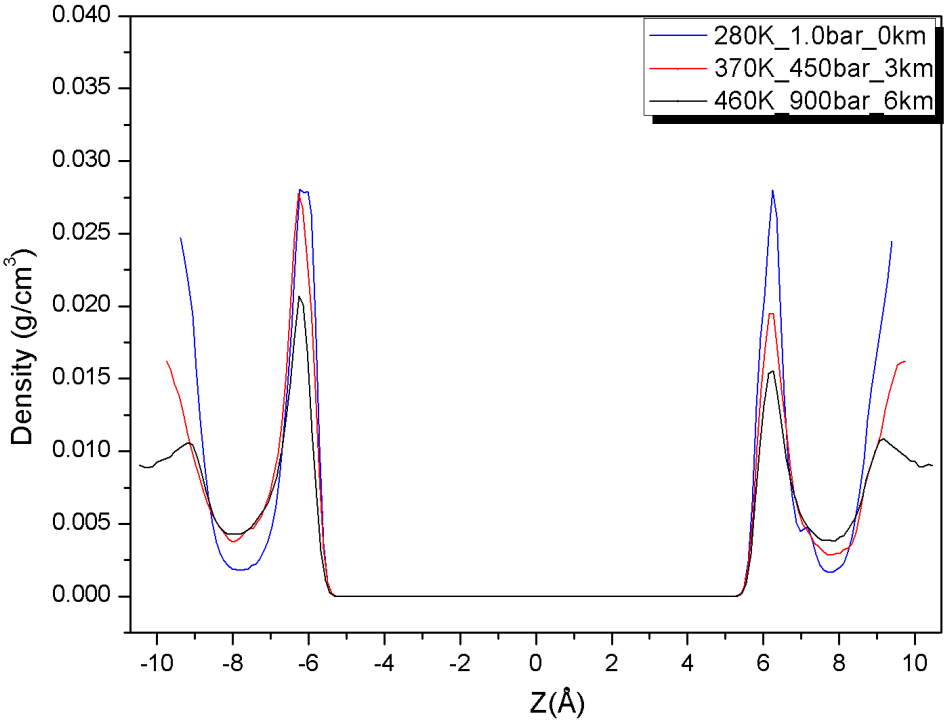


**Fig.6–3: Density profiles for Carbon atoms as a function of distance from mid-plane of solid layer at different burial depths for two layer hydrate system.**

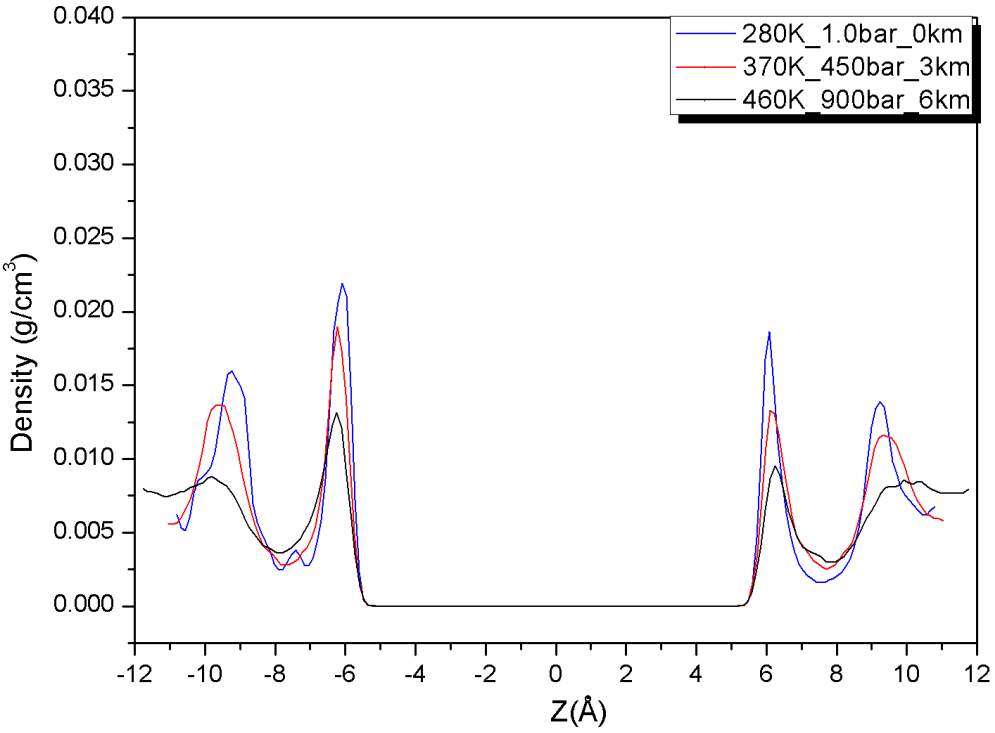


**Fig.6–4: Density profiles for Carbon atoms as a function of distance from mid-plane of solid layer at different burial depths for three layer hydrate system.**

The carbon atom density profile has only one major peak near the surfaces, while oxygen atoms in $CO_2$ molecules form a small peak just near to the biggest one. That means the $O_c$-C-$O_c$ vector is tilted from the normal surface, there exists a specific $CO_2$ orientation. We have shown in Fig6-5 the atomic density profiles for oxygen atoms near the MMT surface for 1-, 2- and 3- layer hydrates for a burial depth of 3 Km. We found the same behaviours for oxygen atoms compared with carbon atoms. In low hydrate state, the contribution of $CO_2$ particles in the interlayer region is near to the layer surface. With increasing the number of water molecules, a part of $CO_2$ molecules approaches to the mid plane of interlayer region. Therefore we can see the third big peak in the middle of interlayer region for two layer hydrate system, others four peaks appear for the three layer hydrate system, two big peaks near each layer surface and another two located nearby the mid plane of interlayer region.

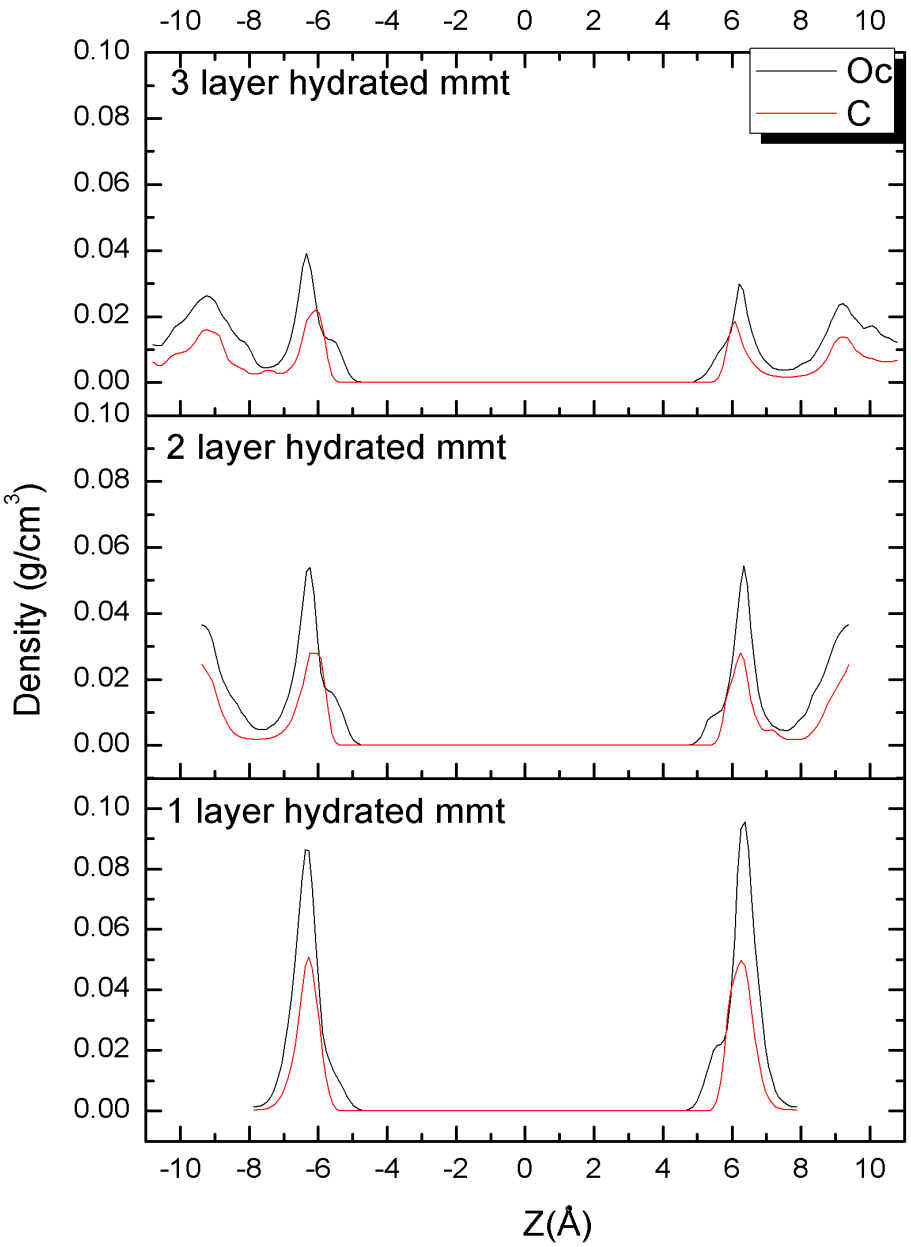


**Fig. 6–5: Density profiles for carbon and oxygen atoms in carbon dioxide molecules as a function of distance from mid-plane of solid layer at different layer hydrate system for burial depth of 3 Km**

The water molecules in Ca-MMT interlayer region were also observed to bond with the clay surface oxygen. This is evident from Fig. 6-6 showing the density profile for water molecules in the one-, two-, and three-hydrated forms as a function of burial depths. The relative position of layered water molecules to the Ca-counterions and carbon dioxide particles is shown in Fig.6-1.

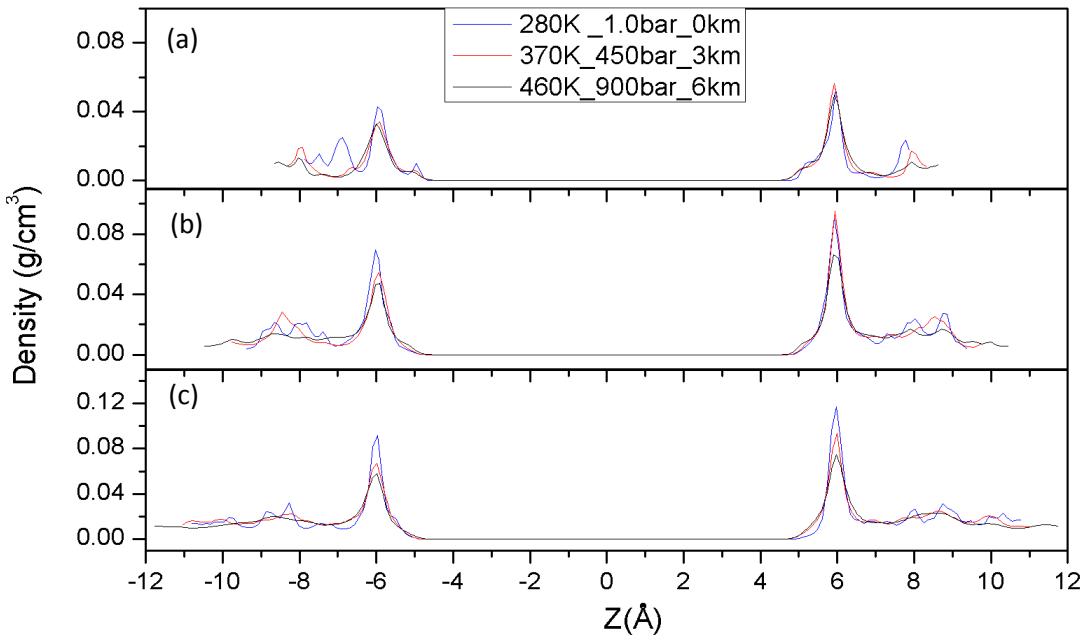


**Fig. 6–6: Density profiles for water molecules as a function of distance from mid plane of solid layer at different burial depths for (a) one-, (b) two-, and (c) three layer hydrates.**

The molecular dynamics simulation method is performed to predict the self-diffusion behavior of interlayer water, carbon dioxide and calcium ions. The calculated self-diffusion are shown in Table6-4. Since there are no many corresponding experimental results to make comparison, we have used some other simulation results, such as the diffusion coefficients of water and calcium couterions in 1-, 2- and 3- layer hydrated Ca-montmorillonite obtained by Zheng et al.[82, 83], and the diffusion coefficients of interlayer water and carbon dioxide in Na-montmorillonite at T=348.15K for 25 bar and 125 bar reported by Botan et al. [77]. Although our results don't correspond exactly to these simulations, our calculated values are of the same order of magnitude. The difference is due to the different temperature and pressure and the employed simulation conditions.

The diffusion of water molecules increases with the quantity of water content. The same phenomenon occurs for the diffusion of interlayer carbon dioxide and calcium ions in different hydrate system. Obviously, the quantity of water content in the clay plays an important role on the diffusion behaviour of interlayer water molecules, carbon dioxide and calcium ions. At one layer hydrate states, we have the same number of water and carbon dioxide molecules, but the transport of water molecules is slower than that of carbon dioxide for different burial depth. This is obvious from the comparison of

calculated radial distribution functions of Ca-$O_W$ and Ca-$CO_2$ (Fig.6-7 and Fig.6-8a). The radial distribution functions for the Ca-$CO_2$ pairs at one layer hydrates for different burial depth are shown in Fig.6-7. The first peaks in the Ca-$O_c$ and Ca-C RDFs occur at approximately 4.87 Å and 5.87 Å for burial depth of 0km, 5.07 Å and 5.92 Å for burial depth of 3km, 5.02 Å and 6.02 Å for burial depth of 6km, respectively. The first peaks for Ca-$O_W$ in one layer hydrate system are situated at 2.47 Å for all the three different burial depths shown in Fig.6-8a. The nearest-neighbor coordination number can be calculated by integrating over the first peak of the correlation function. The value of the first peak for Ca-$O_W$ RDFs is much larger than that of Ca-$CO_2$ peaks. That means the number of water molecules attracted by calcium ions is more than the one of carbon dioxide particles. This makes water molecules and cations diffuse more difficultly than the Carbon dioxide molecules.

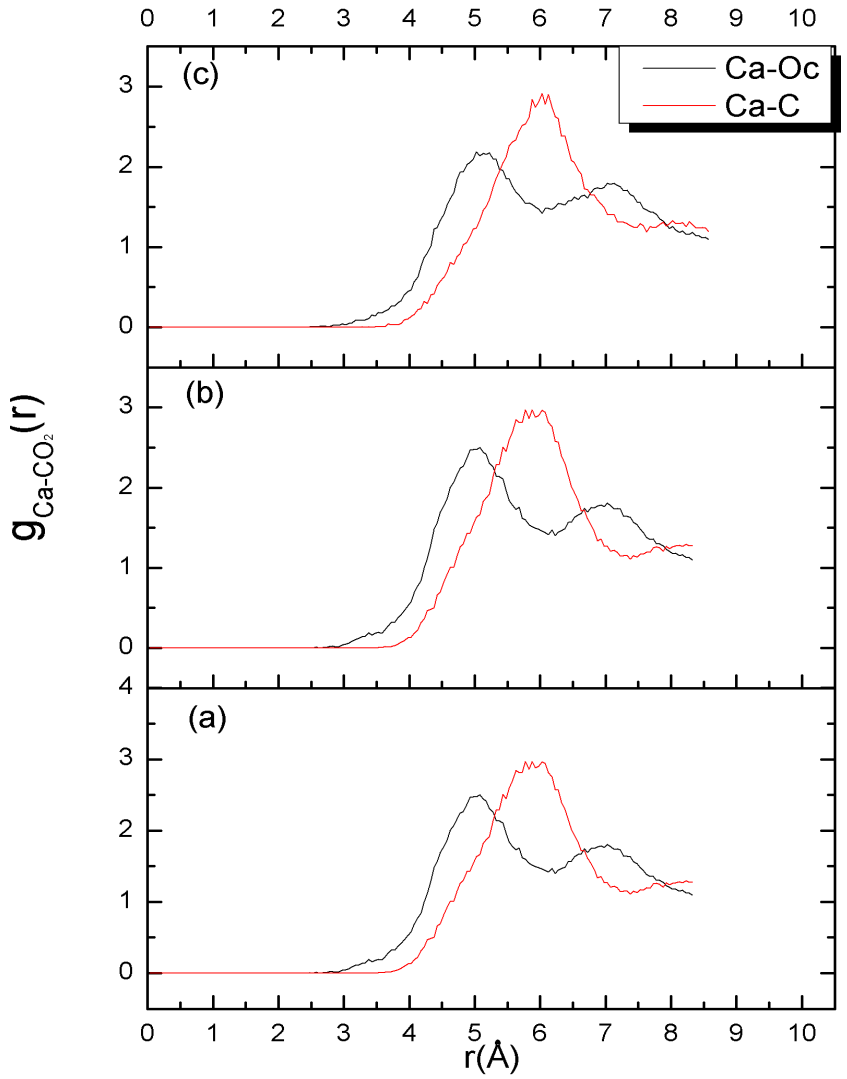


**Fig.6–7: Radial distribution functions for Ca-$CO_2$ interactions at one layer hydrate system for (a) burial depths of 0km, (b) burial depths of 3km and (c) burial depths of 6km.**

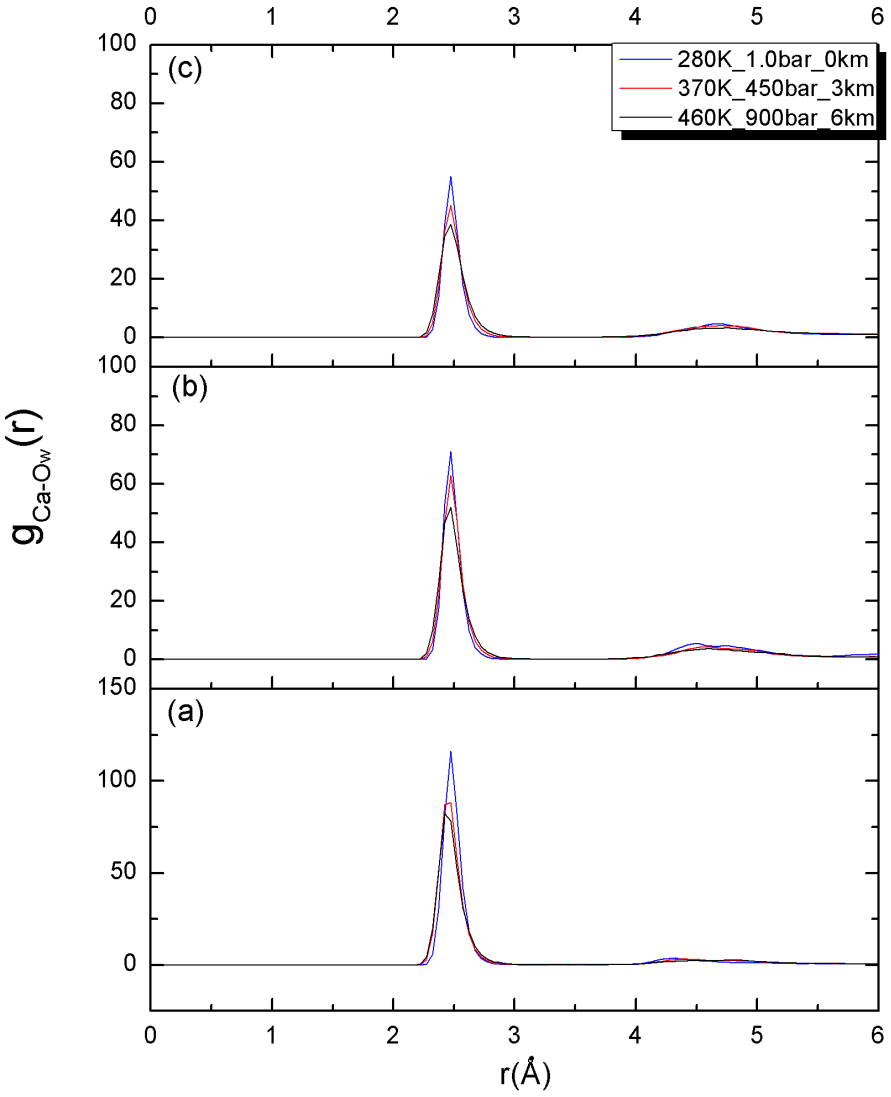


**Fig.6–8: Radial distribution functions for Ca-$O_w$ interactions at different burial depths for (a) one-, (b) two-, and (c) three-layer hydrates.**

The interactions between interlayer particles are generated by the vibration of interlayer particles. This vibration is affected by system conditions like temperature, pressure, quantity of water molecules and interlayer space, etc. At lower depth, the temperature and pressure is relatively lower, which makes small vibration of interlayer particles. The interaction between water and other interlayer particles generated by the vibration is weak. So, the movement of interlayer particles is relative lent. The calculated self-diffusion coefficients in one layer hydrate system are found $0.08\times10^{-9}$ $m^2/s$, $0.13\times10^{-9}$ $m^2/s$ and $0.02\times 10^{-9}$ $m^2/s$ for interlayer water molecules, carbon dioxide molecules and calcium ions, respectively. With the increase of depth, higher temperature and pressure make interlayer particle

vibrate roughly. At 6 km depth interlayer particles were noted to move faster with $D_{H2O}$=0.62×10$^{-9}$ m$^2$/s, and $D_{CO2}$=3.21×10$^{-9}$ m$^2$/s. At high hydrate state, the interlayer spacing of high hydrate system is large enough, which permit the interlayer particles to diffuse freely. Water quantity is large and the interactions between water molecules and carbon dioxide and counterions are strong to make them moving quickly.

The results obtained by Zheng et al.[82] given in Table6-5 and compared with our simulation results indicate that the presence of carbon dioxide molecules reduces the mobility of interlayer water and calcium ions. These simulations are performed in conditions similar to our burial depth of 0km (T=300K and P=1.0bar). For one layer hydrate $CO_2$-$H_2O$-MMT system of Botan et al.[77], the simulation conditions are T=348.15K P=25bar or P=125bar, which correspond to our conditions between burial depth of 0km and 3km. The rate of movement of carbon dioxide molecules were found between that of our results at 0km depth and 3km depth, ranging from 0.138×10$^{-9}$ m$^2$/s to 1.954×10$^{-9}$ m$^2$/s, respectively. The same behavior for two layer hydrate $CO_2$-$H_2O$-MMT system, $D_{CO2}$=1.6×10$^{-9}$ m$^2$/s for P=25bar and $D_{CO2}$=1.5×10$^{-9}$ m$^2$/s for P=125bar were found in the range of 0.605×10$^{-9}$ m$^2$/s and 2.171×10$^{-9}$ m$^2$/s in our simulation for two layer hydrate system at 0km depth and 3 km depth, respectively.

The burial depth and hydration degree of system play an important role to the mobility of interlayer particles. With arise of water content, self-diffusion coefficient of interlayer particles tends to increase. The mobility of interlayer particles increases due to an increase of hydrophobic interaction as the depth is increased from 0km to 3km and 6km. For mobility of water molecules, the burial depth and hydration degree have the same importance. However, compared to water content, the burial depth seems to have more influence on the mobility of carbon dioxide molecules. The carbon dioxide diffusion coefficient has a spectacular rise from 0.605×10$^{-9}$ m$^2$/s at zero depth, to 6.060×10$^{-9}$ m$^2$/s at 6km for two layer hydrate system. However, carbon dioxide self-diffusion coefficients show a rather unspectacular rise at burial depth of 3km for example, from 1.954×10$^{-9}$ m$^2$/s at one layer hydration, to 2.171×10$^{-9}$ m$^2$/s at two layers hydration and 2.320×10$^{-9}$ m$^2$/s at three layers hydration.

The self-diffusion coefficient of carbon dioxide molecules in zero hydrate system have been calculated at different burial depth. The results obtained are 0.061×10$^{-9}$ m$^2$/s for zero km, 0.230×10$^{-9}$

$m^2/s$ for depth of 3km and $0.630\times10^{-9}$ $m^2/s$ for depth of 6km. There is no much difference between the calculated results for one layer hydrate system.

**Table6-4: Self-diffusion coefficients (in $10^{-9}$ $m^2/s$) for interlayer water, carbon dioxide and $Ca^{2+}$ in hydrated Ca-montmorillonite as a function of burial depth.**

| | 1 layer ($32H_2O$,$32CO_2$) | | | 2 layer ($64H_2O$,$32CO_2$) | | | 3 layer ($96H_2O$,$32CO_2$) | | |
|---|---|---|---|---|---|---|---|---|---|
| **T, P, Depth** | $D_{H2O}$ | $D_{CO2}$ | $D_{ca}$ | $D_{H2O}$ | $D_{CO2}$ | $D_{ca}$ | $D_{H2O}$ | $D_{CO2}$ | $D_{ca}$ |
| **280K,1bar, 0.0km** | 0.084 | 0.138 | 0.001 | 0.346 | 0.605 | 0.011 | 0.813 | 0.892 | 0.086 |
| **370K,450bar,3.0km** | 0.200 | 1.954 | 0.041 | 1.863 | 2.171 | 0.026 | 2.332 | 2.320 | 0.155 |
| **460K,900bar,6.0km** | 0.627 | 3.210 | 0.010 | 3.890 | 6.060 | 0.076 | 7.460 | 5.010 | 0.520 |

**Table6-5: Simulation result of diffusion coefficient of water, carbon dioxide and cations in different hydrate montmorillonite presented by Zheng et al.[82] and Botan et al.[77]**

| | $D_{H2O}$ | $D_{CO2}$ | $D_{cations}$ |
|---|---|---|---|
| **One layer hydrate Ca-$H_2O$-MMT T=300K P=1.0bar [82]** | 0.295 | | 0.003 |
| **Two layer hydrate Ca-$H_2O$-MMT T=300K P=1.0bar[82]** | 0.752 | | 0.042 |
| **Three layer hydrate Ca-$H_2O$-MMT T=300K P=1.0bar [82]** | 1.103 | | 0.635 |
| **One layer hydrate Na-$CO_2$-$H_2O$-MMT[77] T=348.15, P=25bar** | 0.51 | 0.24 | 0.19 |
| **One layer hydrate Na-$CO_2$-$H_2O$-MMT[77] T=348.15, P=125bar** | 0.32 | 0.17 | 0.13 |
| **Two layer hydrate Na-$CO_2$-$H_2O$-MMT[77] T=348.15, P=25bar** | 3.50 | 1.60 | 1.30 |
| **Two layer hydrate Na-$CO_2$-$H_2O$-MMT[77] T=348.15, P=125bar** | 3.20 | 1.50 | 1.40 |

## 6.5 Conclusion

Grand canonical Monte Carlo and molecular dynamics simulations have been used to study the structure and dynamics of carbon dioxide molecules in hydrated Ca-montmorillonite clays under conditions encountered in sedimentary basins. At low hydrate system, $CO_2$ molecules are located close

to the clay surface with the linear O=C=O slightly tilted relative to the surface. In the two layers and three layers hydrate system, the interlayer region is big enough to permit a part of carbon dioxide molecules to move to the center of interlayer. The interlayer diffusion strongly depends on the water content as well as on the burial depth. The presence of interlayer $CO_2$ inhibits the diffusion of all the mobile species. These results mainly show that the hydrated clay system is capable of adsorbing $CO_2$ molecules.

Further work is under progress, we will investigate the effect of other counterions like $Na^+$, $K^+$, $Li^+$, and also some heavy metal cations as pollutant as $Rb^+$, $Cs^+$, $Ni^{2+}$ and $Zn^{2+}$ on the dynamics and structure of carbon dioxide.

# SUMMARY

In this thesis, we have performed three different works to understand the adsorption behavior of radionuclide elements and carbon dioxide onto clay materials. Monte Carlo and Molecular Dynamic simulation methods have been employed to study: 1) the adsorption of uranyl species $(UO_2)^{2+}(H_2O)_5$ onto kaolinite (001) surfaces; 2) the adsorption of radionuclide elements species onto substituted Montmorillonite (001) surface in the presence of different counterions; 3) the structure and dynamics of carbon dioxide in hydrated calcium montmorillonite clays under conditions encountered in sedimentary basins.

Kaolinite clays do not have big cation exchange capacity value when compared with other swelling clays minerals. However, the chemically active surface defect sites in kaolinite allow it to have high retention capacity to many nuclear wastes. In order to have complex of Uranyl-kaolinite as many as possible, two silanol defects have been created at the opposite Si(t) side of the slab. These defects may be deprotonated when necessary for charge compensation. Various adsorption complexes have been modeled depending on the degree of deprotonation of Al(o) surface hydroxyl group. We found two principals adsorption mechanisms between uranyl and kaolinite clay: outer-sphere adsorption and inner-sphere adsorption. The interaction between uranyl and kaolinite is mainly electrostatic for outer-sphere complexes, the adsorbed distance between U and surface oxygen is long. For inner-sphere complexes, bond formations of U atom and surface oxygen or hydroxyl group are observed, and the bond length of U atom and surface oxygen atom is relatively smaller. The inner-sphere complexes are considered as leading to strong chemical bound.

This first 'Molecular Dynamics' model study of uranyl adsorption complexes at a 1:1 clay mineral surfaces provided valuable insight in geometric aspects. Yet, to achieve a more complete atomistic description of uranyl sorption onto the clay minerals surfaces, a 2:1 Wyoming-type Montmorillonite has been chosen because of its strong adsorption and ion exchange capacity. More information about energetic aspects has been explored for adsorption complexes of uranyl-MMT. The structure and the dynamics of uranyl ion as well as its aquo, chloride ion, and carbonate complexes were analyzed. In

addition, we have studied the surface energy between layered Montmorillonite sheets and the work of adhesion between radionuclide and charged Montmorillonite. The main contributions to the formation of the surface energy are the electrostatic interactions changes and the van der Waals interaction changes. We have found that the van der Waals interactions are significantly weaker than electrostatic interactions. The simulated values of surface energy with the presence of different counterions are found between 31.481mj/m² and 139.299mj/m². Interfacial properties and the work of adhesion for complexes of radionuclide element and MMT surface were estimated. The work of adhesion of adsorption complexes correspond to 0.422~2.348 j/$m^2$, which are found more important than that of surface energy. This is generally caused by the small van der Waals contact surface area between radionuclide species and MMT surface. The distribution of the superficial Si→Al charge defects make uranium ions approach to the surface oxygen centers that most adjacent to the defects and finally break some U-$O_w$ bonds to form new U-$O_s$ bond. The work of adhesion on the charged MMT surface increases with increasing number of U-Os bond formation and the chemical interaction between interlayer cations and $CO_3^{2+}$ and $Cl^-$ ions.

In the last part of this thesis, we have focussed on the study of the storage of carbon dioxide by hydrated Ca-Montmorillonite clay. Grand canonical Monte Carlo simulations were used to add the water and carbon dioxide molecules into the interlayer space. The calculated layer spacing was found to increase with burial depths. The layer spacing increases when it adsorbs more and more water molecules for the same temperature and stresses conditions. Then, we employed molecular dynamics simulations to understand the diffusion behaviours of $CO_2$ and water molecules. The burial depth and hydration degree of system play an important role to the mobility of interlayer particles. With arise of water content, self-diffusion coefficient of interlayer particles tends to increase. The mobility of interlayer particles increases due to an increase of hydrophobic interaction as the depth is increased from 0km to 3km and 6km. For mobility of water molecules, the burial depth and hydration degree have the same importance. However, compared to water content, the burial depth seems to have more influence on the mobility of carbon dioxide molecules.

# References


1. Bergaya, F. and G. Lagaly, *Chapter 1 - General Introduction: Clays, Clay Minerals, and Clay Science*, in *Developments in Clay Science*, B. Faïza and L. Gerhard, Editors. 2013, Elsevier. p. 1-19.

2. Smith, I., *Smith's elements of soil mechanics*. 2013: Wiley. com.

3. Pusch, R., *Chapter 11.4 Clays and Nuclear Waste Management*, in *Developments in Clay Science*, B.K.G.T. Faïza Bergaya and L. Gerhard, Editors. 2006, Elsevier. p. 703-716.

4. Ghg, I., *Leading options for the capture of CO2 emissions at power stations.* IEA Greenhouse Gas R&D Programme, Cheltenham, UK, report PH3/14, Feb, 2000.

5. Cygan, R.T., J.-J. Liang, and A.G. Kalinichev, *Molecular models of hydroxide, oxyhydroxide, and clay phases and the development of a general force field.* The Journal of Physical Chemistry B, 2004. **108**(4): p. 1255-1266.

6. Shoval, S., et al., *Hydroxyl-stretching bands in polarized micro-Raman spectra of oriented single-crystal Keokuk kaolinite.* Clays and clay minerals, 2002. **50**(1): p. 56-62.

7. Newman, A.C., *Chemistry of clays and clay minerals*. 1987: Longman scientific and technical.

8. Frenkel, D., B. Smit, and M.A. Ratner, *Understanding molecular simulation: from algorithms to applications.* Physics Today, 1997. **50**: p. 66.

9. Metropolis, N., et al., *Equation of state calculations by fast computing machines*, in *The journal of chemical physics*. 1953. p. 1087.

10. Wood, W. and F. Parker, *Monte Carlo Equation of State of Molecules Interacting with the Lennard‐Jones Potential. I. A Supercritical Isotherm at about Twice the Critical Temperature.* The Journal of Chemical Physics, 1957. **27**: p. 720.

11. Alder, B. and T. Wainwright, *Molecular dynamics by electronic computers.* Transport processes in statistical mechanics, 1958: p. 97-131.

12. Allen, M.P. and D.J. Tildesley, *Computer simulation of liquids*. 1989: Oxford university press.

13. Gibson, J., et al., *Dynamics of radiation damage.* Physical Review, 1960. **120**(4): p. 1229.

14. Teppen, B.J., et al., *Molecular dynamics modeling of clay minerals. 1. Gibbsite, kaolinite, pyrophyllite, and beidellite.* The Journal of Physical Chemistry B, 1997. **101**(9): p. 1579-1587.

15. Vasconcelos, I.F., B.A. Bunker, and R.T. Cygan, *Molecular dynamics modeling of ion adsorption to the basal surfaces of kaolinite.* The Journal of Physical Chemistry C, 2007. **111**(18): p. 6753-6762.

16. Fu, M.H., Z.Z. Zhang, and P.F. Low, *Changes in the properties of a montmorillonite-water system during the adsorption and desorption of water: hysteresis.* Clays and clay minerals, 1990. **38**(5): p. 485-492.

17. Zheng, y., *Modélisation et simulation à l'échelle nanométrique de l'effet de température, de pression et des polluants sur l'argile hydratée de type montmorillonite.* Doctorat thesis, university of Lille 1, 2010.

18. Smith, D.E., *Molecular computer simulations of the swelling properties and interlayer structure of cesium montmorillonite.* Langmuir, 1998. **14**(20): p. 5959-5967.

19. Chang, F.R.C., N.T. Skipper, and G. Sposito, *Monte Carlo and molecular dynamics simulations of interfacial structure in lithium-montmorillonite hydrates.* Langmuir, 1997. **13**(7): p. 2074-2082.

20. Boek, E.S., P.V. Coveney, and N.T. Skipper, *Monte Carlo molecular modeling studies of hydrated Li-, Na-, and K-smectites: Understanding the role of potassium as a clay swelling inhibitor.* J. Am. Chem. Soc, 1995. **117**(50): p. 12608-12617.

21. Skipper, N.T. and C. Chang, *Monte Carlo simulation of interlayer molecular structure in swelling clay minerals; 1, Methodology.* Clays and clay minerals, 1995. **43**(3): p. 285.

22. Sylwester, E., E. Hudson, and P. Allen, *The structure of uranium (VI) sorption complexes on silica, alumina, and montmorillonite.* Geochimica et Cosmochimica Acta, 2000. **64**(14): p. 2431-2438.

23. Greathouse, J.A. and R.T. Cygan, *Water structure and aqueous uranyl (VI) adsorption equilibria onto external surfaces of beidellite, montmorillonite, and pyrophyllite: Results from molecular simulations.* Environmental science & technology, 2006. **40**(12): p. 3865-3871.

24. Metropolis, N. and S. Ulam, *The monte carlo method.* Journal of the American statistical association, 1949. **44**(247): p. 335-341.

25. Metropolis, N., et al., *Equation of state calculations by fast computing machines.* The journal of chemical physics, 1953. **21**: p. 1087.

26. Verlet, L., *Computer" experiments" on classical fluids. I. Thermodynamical properties of Lennard-Jones molecules.* Physical review, 1967. **159**(1): p. 98.

27. Gear, C.W., *Numerical initial value problems in ordinary differential equations*. 1971: Prentice Hall PTR.

28. Hockney, R.W., *POTENTIAL CALCULATION AND SOME APPLICATIONS*. 1970, Langley Research Center, Hampton, Va.

29. Swope, W.C., et al., *A computer simulation method for the calculation of equilibrium constants for the formation of physical clusters of molecules: Application to small water clusters.* The Journal of Chemical Physics, 1982. **76**: p. 637.

30. M.P.ALLEN and D.J.TILDESLEY, eds. *Computer Simulation of Liquids*. 1987, oxford university Press,New York.

31. Lewis, G. and C. Catlow, *Potential models for ionic oxides.* Journal of Physics C: Solid State Physics, 1985. **18**(6): p. 1149.

32. Montroll, E.W. and J.L. Lebowitz, *The liquid state of matter: fluids, simple and complex*. 1982: North-Holland.

33. Todorov, I., W. Smith, and U. Cheshire, *The DL POLY 4 user manual.* STFC, STFC Daresbury Laboratory, Daresbury, Warrington, Cheshire, WA4 4AD, United Kingdom, version, 2011. **4**(0).

34. Bayly, C.I., et al., *A well-behaved electrostatic potential based method using charge restraints for deriving atomic charges: the RESP model.* The Journal of Physical Chemistry, 1993. **97**(40): p. 10269-10280.

35. Murthy, C., S. O'Shea, and I. McDonald, *Electrostatic interactions in molecular crystals: lattice dynamics of solid nitrogen and carbon dioxide.* Molecular Physics, 1983. **50**(3): p. 531-541.

36. Righini, R., K. Maki, and M.L. Klein, *An intermolecular potential for methane.* Chemical Physics Letters, 1981. **80**(2): p. 301-305.

37. Tuckerman, M., *Statistical Mechanics and Molecular Simulations*. 2008: Oxford University Press.

38. Teleman, O., B. Jönsson, and S. Engström, *A molecular dynamics simulation of a water model with intramolecular degrees of freedom.* Molecular Physics, 1987. **60**(1): p. 193-203.

39. Hansen, J. and I. McDonald, *Theory of Simple Fluids.* New York, 1986.

40. Côté, A.S., B. Smith, and P.J.D. Lindan, *A Molecular Dynamics tutorial*. 2001.

41. Skoulidas, A.I. and D.S. Sholl, *Self-diffusion and transport diffusion of light gases in metal-organic framework materials assessed using molecular dynamics simulations.* The Journal of Physical Chemistry B, 2005. **109**(33): p. 15760-15768.

42. Allen, P.G., et al., *Investigation of aquo and chloro complexes of UO22+, NpO2+, Np4+, and Pu3+ by X-ray absorption fine structure spectroscopy.* Inorganic Chemistry, 1997. **36**(21): p. 4676-4683.

43. Vallet, V., et al., *Solvent effects on uranium (VI) fluoride and hydroxide complexes studied by EXAFS and quantum chemistry.* Inorganic Chemistry, 2001. **40**(14): p. 3516-3525.

44. Aaberg, M., et al., *Structure of the hydrated dioxouranium (VI) ion in aqueous solution. An x-ray diffraction and proton NMR study.* Inorganic Chemistry, 1983. **22**(26): p. 3986-3989.

45. Clark, D.L., et al., *Chemical speciation of the uranyl ion under highly alkaline conditions. Synthesis, structures, and oxo ligand exchange dynamics.* Inorganic Chemistry, 1999. **38**(7): p. 1456-1466.

46. Guilbaud, P. and G. Wipff, *Force field representation of the UO22+ cation from free energy MD simulations in water. Tests on its 18-crown-6 and NO3-adducts, and on its calix [6] arene6-and CMPO complexes.* Journal of Molecular Structure: THEOCHEM, 1996. **366**(1-2): p. 55-63.

47. Zaidan, O.F., J.A. Greathouse, and R.T. Pabalan, *Monte Carlo and molecular dynamics simulation of uranyl adsorption on montmorillonite clay.* Clays and clay minerals, 2003. **51**(4): p. 372-381.

48. Greathouse, J.A., et al., *Molecular dynamics study of aqueous uranyl interactions with quartz (010).* The Journal of Physical Chemistry B, 2002. **106**(7): p. 1646-1655.

49. Moskaleva, L.V., V.A. Nasluzov, and N. RÖsch, *Modeling Adsorption of the Uranyl Dication on the Hydroxylated -Al2O3 (0001) Surface in an Aqueous Medium. Density Functional Study.* Langmuir, 2006. **22**(5): p. 2141-2145.

50. Hennig, C., et al., *Structure of uranium sorption complexes at montmorillonite edge sites.* Radiochimica Acta, 2002. **90**(9-11/2002): p. 653-657.

51. Den Auwer, C., et al., *Investigating Actinyl Oxo Cations by X ray Absorption Spectroscopy.* European Journal of Inorganic Chemistry, 2003. **2003**(21): p. 3843-3859.

52. Kremleva, A., S. KrÜger, and N. RÖsch, *Density functional model studies of uranyl adsorption on (001) surfaces of kaolinite.* Langmuir, 2008. **24**(17): p. 9515-9524.

53. Reich, T., et al., *Application of XAFS spectroscopy to actinide environmental science.* X-Ray Absorption Fine Structure--XAFS 13, 2007. **882**: p. 179-183.

54. Dierking, S., S. Amayri, and T. Reich, *Actinide Sorption Studies Using the Isotopes 237Np and 239Np.* Journal of NUCLEAR SCIENCE and TECHNOLOGY, 2008. **6**: p. 133-137.

55. Krepelova, A., S. Sachs, and G. Bernhard, *Uranium (VI) sorption onto kaolinite in the presence and absence of humic acid.* Radiochimica Acta, 2006. **94**(12): p. 825-833.

56. Benco, L., et al., *Ab initio density functional theory applied to the structure and proton dynamics of clays.* Chemical physics letters, 2001. **333**(6): p. 479-484.

57. Benco, L., et al., *Upper Limit of the OH⊙⊙⊙ O Hydrogen Bond. Ab Initio Study of the Kaolinite Structure.* The Journal of Physical Chemistry B, 2001. **105**(44): p. 10812-10817.

58. Vasconcelos, I.F., et al., *EXAFS analysis of cadmium (II) adsorption to kaolinite.* Chemical Geology, 2008. **249**(3): p. 237-249.

59. Newman, A.C.D. and G. Brown, *The chemical constitution of clays.* Monograph, Mineralogical Society, 1987(6): p. 1-128.

60. Huertas, F.J., L. Chou, and R. Wollast, *Mechanism of kaolinite dissolution at room temperature and pressure: Part 1. Surface speciation.* Geochimica et Cosmochimica Acta, 1998. **62**(3): p. 417-431.

61. Cygan, R.T., J.J. Liang, and A.G. Kalinichev, *Molecular models of hydroxide, oxyhydroxide, and clay phases and the development of a general force field.* The Journal of Physical Chemistry B, 2004. **108**(4): p. 1255-1266.

62. Pacchioni, G., L. Skuja, and D.L. Griscom, *Defects in SiO2 and related dielectrics: Science and technology*. 2000: Springer Netherlands.

63. Smith, W., et al., *The DL poly 2 user manual.* CCLRC, Daresbury Laboratory, Daresbury, Warrington WA4 4AD, England. **2**.

64. Kraska, T., *Molecular-dynamics simulation of argon nucleation from supersaturated vapor in the NVE ensemble.* The Journal of Chemical Physics, 2006. **124**: p. 054507.

65. Butler, B.D., et al., *Configurational temperature: verification of Monte Carlo simulations.* The Journal of Chemical Physics, 1998. **109**: p. 6519.

66. Stumm, W., *Chemistry of the solid-water interface: processes at the mineral-water and particle-water interface in natural systems*. 1992: John Wiley & Son Inc.

67. Benco, L., et al., *Upper Limit of the OH O Hydrogen Bond. Ab Initio Study of the Kaolinite Structure.* The Journal of Physical Chemistry B, 2001. **105**(44): p. 10812-10817.

68. Martorell, B., et al., *Density Functional Model Study of Uranyl Adsorption on the Solvated (001) Surface of Kaolinite.* The Journal of Physical Chemistry C: p. 335-343.

69. Martorell, B., et al., *Density Functional Model Study of Uranyl Adsorption on the Solvated (001) Surface of Kaolinite.* The Journal of Physical Chemistry C, 2010.

70. Vasconcelos, I.F., et al., *EXAFS analysis of cadmium (II) adsorption to kaolinite.* Chemical Geology, 2008. **249**(3-4): p. 237-249.

71. Krepelov, A., et al., *Structural characterization of U (VI) surface complexes on kaolinite in the presence of humic acid using EXAFS spectroscopy.* Journal of colloid and interface science, 2008. **319**(1): p. 40-47.

72. Skipper, N., F.-R.C. Chang, and G. Sposito, *Monte Carlo simulation of interlayer molecular structure in swelling clay minerals. I: Methodology.* Clays and Clay Minerals, 1995. **43**(3): p. 285-293.

73. Sposito, G., et al., *Surface geochemistry of the clay minerals.* Proceedings of the National Academy of Sciences, 1999. **96**(7): p. 3358-3364.

74. Titiloye, J. and N. Skipper, *Molecular dynamics simulation of methane in sodium montmorillonite clay hydrates at elevated pressures and temperatures.* Molecular Physics, 2001. **99**(10): p. 899-906.

75. Cases, J., et al., *Mechanism of adsorption and desorption of water vapor by homoionic montmorillonite. 1. The sodium-exchanged form.* Langmuir, 1992. **8**(11): p. 2730-2739.

76. Yang, X. and C. Zhang, *Structure and diffusion behavior of dense carbon dioxide fluid in clay-like slit pores by molecular dynamics simulation.* Chemical physics letters, 2005. **407**(4): p. 427-432.

77. Botan, A., et al., *Carbon dioxide in montmorillonite clay hydrates: thermodynamics, structure, and transport from molecular simulation.* The Journal of Physical Chemistry C, 2010. **114**(35): p. 14962-14969.

78. Berendsen, H., et al., *Interaction models for water in relation to protein hydration.* Intermolecular forces, 1981. **11**(1): p. 331-342.

79. Harris, J.G. and K.H. Yung, *Carbon dioxide's liquid-vapor coexistence curve and critical properties as predicted by a simple molecular model.* The Journal of Physical Chemistry, 1995. **99**(31): p. 12021-12024.

80. Mooney, R., A. Keenan, and L. Wood, *Adsorption of Water Vapor by Montmorillonite. I. Heat of Desorption and Application of BET Theory1.* Journal of the American Chemical Society, 1952. **74**(6): p. 1367-1371.

81. Brown, G. and G. Brindley, *Crystal structures of clay minerals and their X-ray identification, ed. M. Society. Vol. Chapter 3.* Mineralogical Society, London, 1980: p. 361-410.

82. Zheng, Y. and A. Zaoui, *How water and counterions diffuse into the hydrated montmorillonite.* Solid State Ionics, 2011. **203**(1): p. 80-85.

83. Zheng, Y. and A. Zaoui, *Temperature effects on the diffusion of water and monovalent counterions in the hydrated montmorillonite.* Physica A: Statistical Mechanics and its Applications, 2013. **392**(23): p. 5994-6001.

**RESUME :**

Afin de prévoir et réglementer l'impact environnemental des activités humaines telle que l'exploitation minière de l'uranium et des déchets radioactifs, il est nécessaire de comprendre le comportement des actinides, la migration des radionucléides dans l'environnement et analyser leur interaction avec l'argile minérale. Le comportement des actinides dans le sol concerne principalement les interactions et les adsorptions dans les surfaces qui changent les formes des éléments radioactifs et réduisent la mobilité des actinides dans les systèmes naturels. Par conséquent, il est important de comprendre comment les actinides interagissent avec l'argile minérale et étudier le processus fondamental de précipitation de surface. L'uranium est la teneur en métal lourd la plus prépondérante des déchets ultimes dans le cycle du combustible nucléaire ( > 95 % de $UO_2$ ). En outre, l'uranium est un contaminant majeur dans le sol, le sous-sol et les eaux souterraines en raison de l'activité humaine. Dans des conditions environnementales standards, la forme chimique la plus stable de U ( VI ) est l' ion uranyle $UO_2^{2+}$, qui est potentiellement très mobile et se combine facilement avec la matière organique et inorganique. D'un autre côté, le dioxyde de carbone est un important gaz à effet de serre, réchauffant la surface de la terre à une température plus élevée en réduisant vers l'extérieur le rayonnement. Toutefois, des problèmes peuvent se produire lorsque la concentration atmosphérique des gaz à effet de serre augmente. Des quantités importantes d'émissions de dioxyde de carbone ont été produites depuis la révolution industrielle, ce qui est derrière l'important réchauffement climatique et l'augmentation du niveau de la mer. Les minéraux argileux sont d'une grande importance pratique, particulièrement dans le stockage du dioxyde de carbone en raison de sa perméabilité hydraulique et sa capacité de conserver les particules mobiles. Nous avons choisi la kaolinite et la montmorillonite comme des prototypes de minéraux argileux de type 1:1 et 2:1. Les méthodes de Monte Carlo (MC) et la dynamique moléculaire (MD) ont été utilisées dans ce travail afin de comprendre le comportement d'adsorption des radionucléides et de dioxyde de carbone à la surface des argiles. Dans cette thèse, nous étudions d'abord l'adsorption de l'uranyle à la surface de la kaolinite par le biais de la dynamique moléculaire et de la Monte Carlo. Plusieurs sites d'adsorption ont été modélisés en considérant des défauts de surface dans le but d'avoir des complexes inter ou externe-sphère. Ensuite, les adsorptions des particules d'uranyle sur des surfaces de la montmorillonite en présence des différents ions seront effectuées. L'énergie d'interaction entre des feuilles de montmorillonite et le travail d'adhérence entre le radionucléide et surface MMT seront également discutés. Enfin, nous présenterons l'étude du comportement d'adsorption de dioxyde de carbone dans le MMT, en détaillant au passage les propriétés thermodynamiques, structurales et dynamiques.

**Abstract**

In order to predict and regulate the environmental impact of human activities such as uranium mining and radioactive waste disposal, it is necessary to understand the behaviour of actinides in the environment because their interaction with clay mineral is an important factor to control the migration of radionuclide in the environment. The behaviour of actinides in the soil is mainly the surface adsorption interactions, which change the forms of radioactive elements and reduces the mobility of actinides in the natural systems. Therefore, it is important to search how the actinides interact with clay mineral such as the fundamental process of surface precipitation. Uranium is the predominant heavy metal content of the final waste in the nuclear fuel cycle (>95% $UO_2$). In addition, uranium is a major contaminant in the soil, subsurface and groundwater as a result of human activity. Under standard environmental conditions, the most stable chemical form of U(VI) is the uranyl ion $UO_2^{2+}$, which is potentially very mobile and readily complexates with organic and inorganic matter. On the other hand, Carbon dioxide is an important greenhouse gas, warming the earth's surface to a higher temperature by reducing outward radiation. However, problems may occur when the atmospheric concentration of greenhouse gases increases. Amounts of carbon dioxide were produced since the industrial revolution, which is behind the significant global warming and rising sea level. Clay minerals are of great practical importance here, in storage of carbon dioxide due to its hydraulic permeability and ability to retain mobile species. We have chosen kaolinite and montmorillonite as prototypes of clay minerals of 1:1 and 2:1. Classical Monte Carlo (MC) and molecular dynamics (MD) methods have been used in this work in order to understand the adsorption behaviour of radionuclide and carbon dioxide in clays surface. In this thesis, we will investigate –first- the adsorption of uranyl on kaolinite surface by means of Monte Carlo and Molecular Dynamics simulation methods. Several adsorption sites have been modeled by considering surface defects in order to have inner or outer-sphere complexes. Then, the adsorptions of uranyl species onto Montmorillonite surfaces in the presence of different counterions will be performed. Interaction energy between Montmorillonite sheets and work of adhesion between the radionuclide and MMT surface will be discussed as well. Finally, we present the study of the adsorption behaviour of carbon dioxide in MMT, and -at the same time- thermodynamics, structural and dynamical properties.